OUKA
Osaka University Knowledge Archive

Title	Numerical Study on Fracture Mechanics Parameters of Fatigue Cracks in Welded Joints under Arbitrary Stress Distributions
Author(s)	Kyaw, Phyo Myat
Citation	大阪大学, 2022, 博士論文
Version Type	VoR
URL	https://doi.org/10.18910/89634
rights	
Note	

Osaka University Knowledge Archive : OUKA

https://ir.library.osaka-u.ac.jp/

Osaka University

Doctoral Dissertation

Numerical Study on Fracture Mechanics Parameters of Fatigue Cracks in Welded Joints under Arbitrary Stress Distributions

（任意応力場中にある溶接継手疲労き裂の数値破壊力学パラメタ評価法に関する研究）

PHYO MYAT KYAW

June 2022

Graduate School of Engineering,
Osaka University

A Dissertation for Doctor of Engineering Degree submitted to

Osaka University

Graduate School of Engineering

Division of Global Architecture

Department of Naval Architecture and Ocean Engineering

in
June 2022

Supervised by
Professor Naoki Osawa

Committee members

Professor Kazuhiro Iijima

Graduate School of Engineering, Osaka University

Professor Ninshu Ma

Joining and Welding Research Institute, Osaka University

Associate Professor Satoyuki Tanaka

Graduate School of Advanced Science and Engineering, Hiroshima University

Abstract

Ships and offshore structures are mainly constructed using welded panels and joints. Welded structures that are subjected to cyclic loadings are at a high risk of failure due to fatigue damage. Fatigue strength of the welded structures under the cyclic wave and mechanical loads is mostly affected by the welding residual stress (RS) followed by the flaws. The undesirable high tensile RS can be reduced by using post-weld treatment methods such as high-frequency mechanical impact (HFMI) treatment.

In welded joints, the cracks can exist as pre-existing flaws or appear sometime after welding due to the stress concentration at the weld toe/root and applied cyclic loading. Therefore, the fatigue strength of welded structures is usually evaluated using the fracture mechanics approach in fitness for purpose assessments. Moreover, in service conditions, the structures are subjected to multiaxial loading, and it is crucial to also consider mixed-mode fracture failures of welded structures. Despite the necessity, the mixed-mode fracture of HFMI-treated joints has not been studied due to its difficulty to consider all the components of RS in the calculation of fracture parameters.

For reliable fracture assessments, accurate values of stress intensity factors (SIFs) are important parameters. Analytical and numerical methods are widely used to calculate the SIF solutions. However, precise estimation of SIFs for cracks in RS fields under multiaxial loading is still challenging work for researchers. The investigation of mixed-mode SIFs (MM-SIFs) of T-joints under arbitrary stress distributions has not been accomplished in the previous studies. The MM-SIFs due to HFMI-induced RS is also still under mystery as no such calculation methodology has been reported before.

In this study, a numerical MM-SIF calculation system was proposed based on the influence function method (IFM). The proposed numerical IFM (NIFM) was verified using a simple flat cracked-body under multi-axial loading. The NIFM was then applied to the MM-SIF calculation of as-welded and HFMI-treated T-joints. The fatigue life of T-joints under constant amplitude loading considering six components of welding RS was also estimated using the NIFM. In addition, the numerical weld modification factor method and its formulae were introduced based on the NIFM. The developed formulae are validated and then applied for evaluating the MM-SIFs of T-joints considering welding RS.

Acknowledgments

This thesis becomes a reality not only with my research input but also with the educational, intellectual, emotional, and financial support of many individuals. I would like to express my gratitude to all of them without whom I would not have accomplished this research.

Foremost, I am tremendously grateful for Professor Osawa's guidance, kindness, and inspiration throughout my study at Osaka University. The fruitful conversations we frequently had during these years equipped me with the knowledge and skillsets to complete this research.

Secondly, I would like to appreciate Professor Tanaka for his valuable advice and priceless input to my study. Most of my works were finished exceptionally and beautifully with his suggestions and supervision. I would also like to send my sincere thanks to Professor Gadallah for being a wonderful mentor and guiding me throughout this research work. It was also a great pleasure to have worked with Professor Rashed, receiving his kindness and knowledge. I sincerely appreciate Professor Ma and Professor Iijima for the constructive discussions, feedback, and time shared with my work.

This thesis is dedicated to my Mom, Nyo Nyo Than, as my deepest appreciation for not giving up on my academic journey despite the difficulties we had in the past. Also, I owe Min a great debt as I will not be able to stand the ups and downs during these five years without his help and encouragement. Likewise, I might not be able to reach this far in my education without the financial and mental support of my childhood teachers, the teachers from MMU, and my god-father, U Zaw Win, and his family.

My colleagues and friends at OU have always been good companions to me and I cannot thank you enough for these memorable experiences. As well, it has always been a blessing to have my friends and siblings all along by my side providing such warm hugs and words to conquer the hardships and stresses faced on this path.

Finally, and greatly, I would like to send my gratitude to the Japanese government for providing me with funding during my study at Osaka University.

PHYO MYAT KYAW

Table of Contents

Nomenclature

Symbols

a	=	crack depth, mm
a_f	=	length of the front end of the heat source model, mm
a_r	=	length of the rear end of the heat source model, mm
a/c	=	crack depth-to-crack length ratio
a/t	=	crack depth-to-model thickness ratio
A, B	=	coefficients of least squares regression equation
b	=	half-breadth of the heat source model, mm
c	=	crack half-length, mm
C	=	material constant in cyclic crack growth relationship, N/cycle.mm$^{1/2}$
C_i	=	kinematic hardening parameter
$C_{I,II,III}^{ij,QP}$	=	MM-SIFs at the target nodes along the crack front (*Q-th* node) due to six components of unit distributed load (σ_{ij}) at the crack face node (*P-th* node), namely, influence coefficients, MPa.mm$^{1/2}$
d	=	depth of the heat source model, mm
$\frac{da}{dN}$	=	crack growth rate with cycles, mm/cycle
F_I, F_{II}, F_{III}	=	normalized values of mode-I, -II, and -III SIFs, respectively
E	=	Young's modulus, GPa
E^*	=	effective Young's modulus, GPa
$h(x, geo.)$	=	geometric influence function on the crack length parallel to the x-axis
$I(s)$	=	interaction integral at crack front location s
$\bar{I}(s)$	=	domain form of the interaction integral at crack front location s
J_2	=	second stress invariant
K	=	stress intensity factor, MPa.mm$^{1/2}$
K_{Imin}, K_{Imax}	=	minimum and maximum SIFs for mode-I, MPa.mm$^{1/2}$
$K_I^{aux}, K_{II}^{aux}, K_{III}^{aux}$	=	auxiliary mode-I, -II, and -III SIFs, MPa.mm$^{1/2}$
$K_{I,II,III}^{Q}$	=	MM-SIFs at the *Q-th* nodes due to crack face tractions, MPa.mm$^{1/2}$
K^{QP}	=	influence coefficient defined in Shiratori et al. (1986)

$^{(w)}K^{Q}_{I,II,III}$	=	$K^{Q}_{I,II,III}$ of the welded joint, MPa.mm$^{1/2}$
$^{(f)}K^{Q}_{I,II,III}$	=	$K^{Q}_{I,II,III}$ of the flat plate, MPa.mm$^{1/2}$
$^{(w)}K$	=	generic term of $^{(w)}K^{Q}_{I,II,III}$
$^{(wf)}K$	=	MM-SIFs of the flat plate at the *Q-th* nodes due to crack face tractions observed in the welded joint, MPa.mm$^{1/2}$
K_{flat}	=	SIF of a flat plate under remote loading, MPa.mm$^{1/2}$
K_Q	=	SIF at the *Q*-th node, MPa.mm$^{1/2}$
K_{weld}	=	SIF of a welded joint under remote loading, MPa.mm$^{1/2}$
L	=	straight crack face boundary in a 2D crack, mm
L_C	=	length of the crack front segment, mm
L_e	=	edge length of the smallest element at the crack front line, mm
m	=	exponent in crack growth law
M	=	Number of kinematic hardening components
M_k	=	magnification factor
N	=	number of fatigue life cycles, cycles
N_i	=	shape function for a normalized coordinate system on each element face node *i*
P	=	node on the crack face element defined in the IFM
Q	=	node on the crack front defined in the IFM
Q_s	=	Flaw shape parameter
$q(s)$	=	weight function at point *s* on the crack front
r	=	distance from the crack front
R	=	stress ratio
R_D	=	radius of the largest domain surrounding the crack front line, mm
S	=	finite surface
S^+	=	upper crack surface
S^-	=	lower crack surface
t_{ij}	=	crack face traction components, MPa
u_j	=	displacement components
U	=	stress range ratio
U_x	=	displacement loading in the *x*-direction, mm
V	=	finite volume

x, y, z	=	Cartesian coordinates, mm
x', y', z'	=	local coordinates defined on a surface crack, mm
ΔK	=	SIF range, MPa.mm$^{1/2}$
ΔK_{eff}	=	effective SIF range, MPa.mm$^{1/2}$

Greek Symbols

α	=	coefficients of the least squares regression equation
$\boldsymbol{\alpha}$	=	back stress tensor
γ_i	=	kinematic hardening parameter
ε_p	=	equivalent plastic strain
θ	=	flank angle, degree
$\mu_{I,II,III}^{ij,QP}$	=	ratios of IC values of welded joint and flat plate
μ_k	=	weld modification factor, the generic term of $\mu_{k,I,II,III}^{Q}$
$\mu_{k,I,II,III}$	=	Mode-I, -II, and -III μ_k
$\mu_k^{(IC)}$	=	generic term of $\mu_{I,II,III}^{ij,QP}$
$\mu_{k,I,II,III}^{Q}$	=	mode-I, -II, and -III modification factors at the SIF evaluation nodes derived by the influence function method
ν	=	Poisson's ratio
ξ, η	=	normalized coordinates
ρ	=	weld toe radius, mm
$\boldsymbol{\sigma}$	=	acting stress tensor
$\boldsymbol{\sigma}(x)$	=	stress field on the (fictitious) crack face of an uncracked model along the x-axis
σ_0	=	yield stress (scalar)
σ_{ext}	=	external tensile loading, MPa
σ_n	=	unit stress on the crack face node, n, MPa
σ^P	=	traction force at P-th node
$\sigma^{ij,P}$	=	six components of traction stress, ij, i.e., xx, yy, zz, xy, yz, and xz, at the P-th node on the crack face, MPa
${}^{(f)}\sigma^{ij,P}$	=	$\sigma^{ij,P}$ of the flat plate, MPa

${}^{(w)}\sigma^{ij,P}$	=	$\sigma^{ij,P}$ of the welded joint, MPa
σ_{xx}	=	longitudinal (*xx*) component of welding RS
σ_{yy}	=	transverse (*yy*) component of welding RS
φ	=	location of crack front parametric angle, degree

Acronyms

CA	=	constant amplitude
CFT	=	crack face traction
FCP	=	fatigue crack propagation
FE	=	finite element
FEA	=	finite element analysis
HFMI	=	high-frequency mechanical impact
IC	=	influence coefficient
IC-MRDB	=	IC modification ratio database
ICDB	=	IC database
IFM	=	influence function method
IIM	=	interaction integral method
JWRI	=	Joining and Welding Research Institute
MM-SIFs	=	mixed-mode SIFs
NIFM	=	numerical IFM
RS	=	residual stress
SIF	=	stress intensity factor
TEP	=	thermal elastic-plastic
TEP-FEA	=	TEP finite element analysis
TFV	=	traction force vector
TSV	=	traction stress component
UDL	=	unit distributed load
2D	=	two-dimensional
3D	=	three-dimensional

CHAPTER 1

Motivation and scope of the study

1.1 Background

1.1.1 Fatigue failure of welded structures

Welding has been employed on a very wide scale, especially for fabricating metallic plates and girders of different cross sections. It is one of the most convenient and promising methods in the construction of bridges, ships, offshore structures, pressure vessels, cranes, etc. On the other hand, there are some unavoidable post-weld problems such as high-tensile residual stress (RS), porosity, undercuts, cracks, and deformations, that endanger structural strength and reduce fatigue strength. However, the effectiveness and handiness of the welding during construction outweigh the setbacks.

Welding is also a major production technique in buildings ships and offshore structures. The first all-welded hulls were built during World War II [1]. Welded ships did increase the production efficiency, and reduce the overall weight of the ship by replacing the rivets with weld seams which leads to increasing speed of the ship. However, approximately 400 Liberty ships were inspected to have sustained structural failures out of 2700 ships built [2]. Among them, 20 ships faced total failures and 90 were considered serious. According to the investigation reports, the failures were initiated from the fatigue cracks which were associated with welding imperfections and poor fracture toughness of the materials.

Moreover, marine structures are generally subjected to various kinds of fatigue loadings: loads due to varying loading conditions, loads in a seaway, and propulsion-induced loads and vibrations [3]. When these cyclic loadings are superimposed with the high tensile RS of the welded joints, the fatigue strength of the structure is considerably affected [4]. As can be seen in a typical welding RS distribution in a butt welded joint in Fig. 1.1, high tensile RS appeared in and near the weld beads. Also, the combination of welding RS and high local stress concentration due to the notch effect cause fatigue crack initiation sites under cyclic loading. The initiated fatigue cracks are then propagated, and eventually, cause the total failure of the whole structure. In the case of brittle crack propagation as in Liberty ships, it leads to a catastrophic failure in

a short time. Such failures have to be avoided or at least should be controlled to reduce the cost of maintenance and loss of properties. Therefore, fatigue crack propagation (FCP) assessment of welded joints is an important procedure during the design stage as well as for the maintenance of structures.

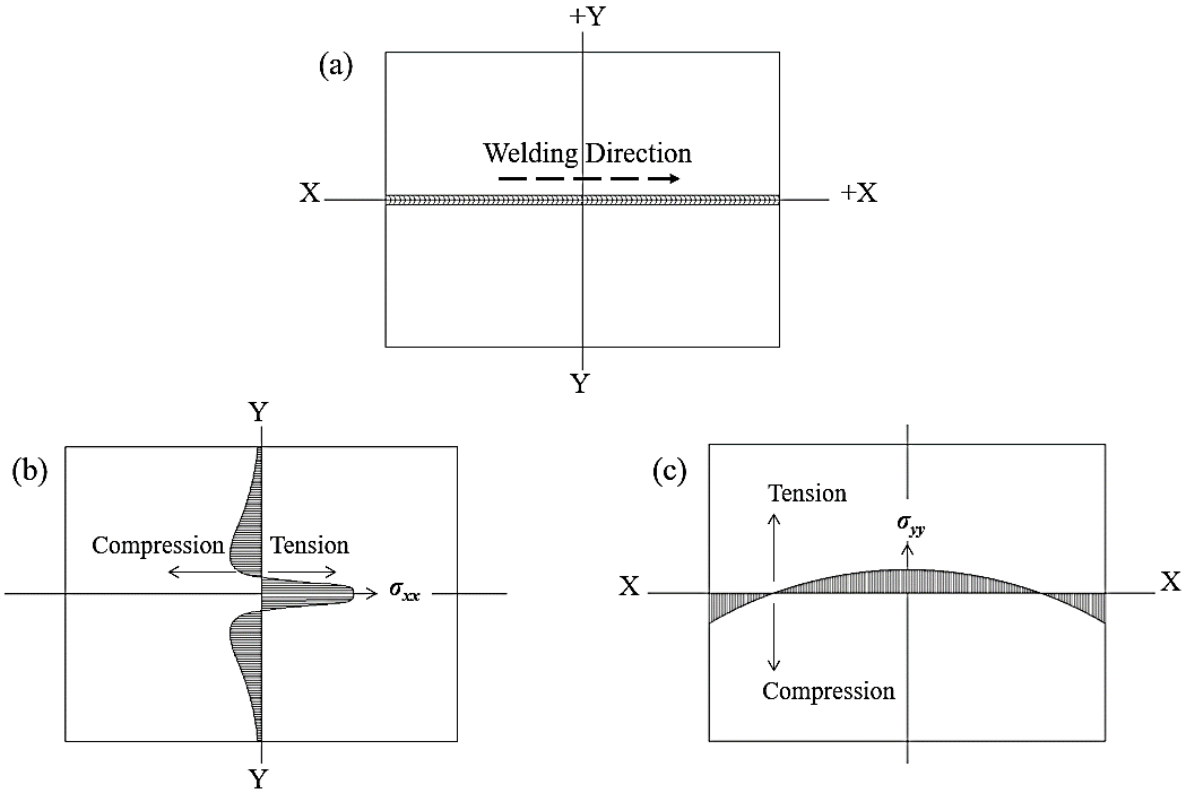

Fig. 1.1 Typical welding RS distributions in a butt joint. (a) Illustration of welding direction and coordinates, (b) distribution of longitudinal RS (σ_{xx}) along YY, and (c) distribution of transverse RS (σ_{yy}) along XX. [5].

1.1.2 Fatigue life improvement using post-weld treatment methods

To improve the fatigue strength of the welded components, good design practice and high-quality fabrication are the most important factors. When the design and fabrication cannot fulfill the target fatigue life, post-weld treatment techniques can be used to increase the fatigue life [6]. Post weld improvement techniques are generally divided into two categories: weld geometry improvement methods and RS improvement methods. The categorization is based on how the improvement is achieved; the methods used in the first group attain the goal by modifying the local geometry and improving the surface quality while the compressive RS is induced in the latter methods to reduce the tensile RS in the welds.

Out of the available post-weld treatment techniques, high-frequency mechanical impact (HFMI) treatment can provide the modification of local weld geometry as well as induce compressive RS after the treatment [7–10]. HFMI devices are composed of a power source and an HFMI tool (indenters). The power source can be ultrasonic piezoelectric, ultrasonic magneto strictive, or pneumatic. The cylindrical indenters strike the target location of a structure or component in cyclic motion with high frequency. The highly plastically deformed region is obtained from the impact with the indenter causing the microstructural changes in the material. The notch effect at weld transitions can also be reduced using the HFMI treatment [6] (see Fig. 1.2). The compressive RS induced after the HFMI greatly contributes to the retardation of crack growth at the weld toe region [11]. Due to its practicality and effectiveness, HFMI peening service providers, equipment manufacturers, and studies have progressively increased in the past decade.

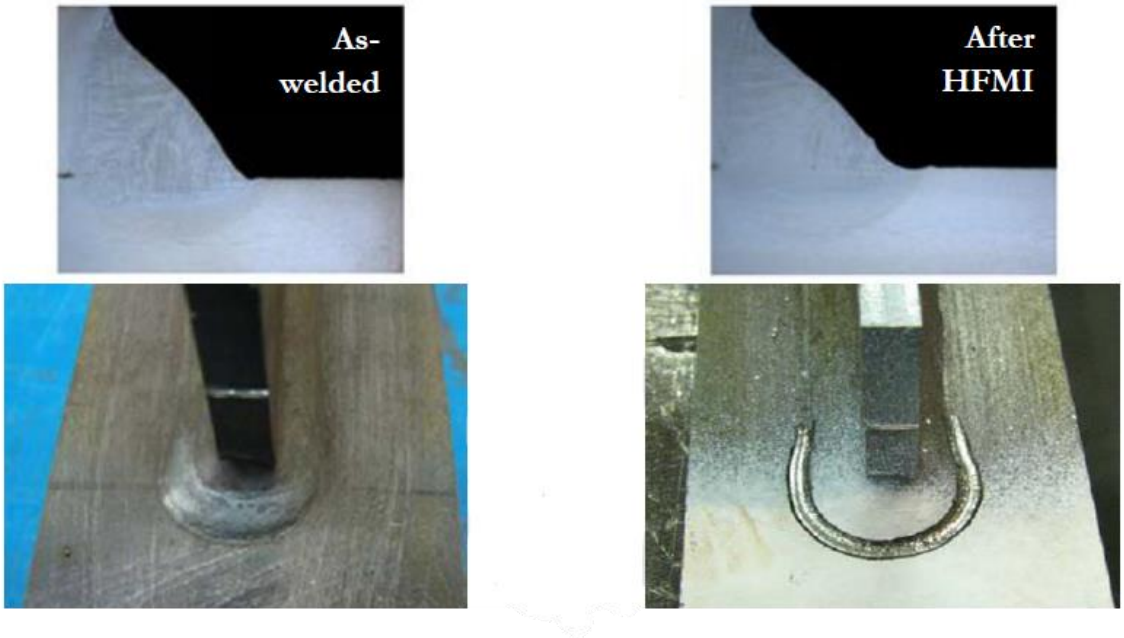

Fig. 1.2 Weld toe profiles in the as-welded condition and HFMI-treated condition [6].

1.1.3 Fatigue crack propagation of welded structures

Fatigue life estimation of structures is carried out through the stress-life approach (S-N approach), or fracture mechanics approach. During the design stage of ship structures, the S-N approach is usually applied. However, if an existing crack is found

while new-building or in-service inspections, the fracture mechanics approach is mainly used so that it can consider crack propagation. In the case of welded joints, the cracks can exist as pre-existing flaws or appear sometime after welding due to the stress concentration at the weld toe/root and applied cyclic loading. Therefore, for the fitness-for-purpose assessment, the fatigue strength of welded structures is usually evaluated using the fracture mechanics approach assuming the initial crack.

Paris-Erdogan law [12] is a popular rule to calculate the crack growth rate of a structure under constant amplitude (CA) loadings. It defines the three phases of crack propagation; low speed of propagation, stable propagation, and high speed of propagation. Generalized crack propagation stages are shown in Fig. 1.3. According to the Paris-Erdogan law, the crack growth rate is dependent on the range of stress intensity factors (SIF) under cyclic loadings. In linear elastic fracture mechanics, a sharp crack front is assumed which can represent a failure in brittle materials, and a local polar coordinate system (see Fig. 1.4(a)) is defined at the crack tip to describe the stress and displacements related to the crack. The closer to the crack tip, the larger the stress near the crack tip as shown in Fig. 1.4(b) causing a stress singularity at the crack tip. The SIF indicates the value of stress intensity (stress state) near the crack tip which is induced by the applied loading or the RS. Hence, SIFs are the important parameter that can estimate the stress near the crack region and the crack growth behavior in brittle fractures. There has been a steady increase in studies on the methodologies to calculate SIFs of different cracked geometries and to improve the accuracy and efficiency of the existing techniques.

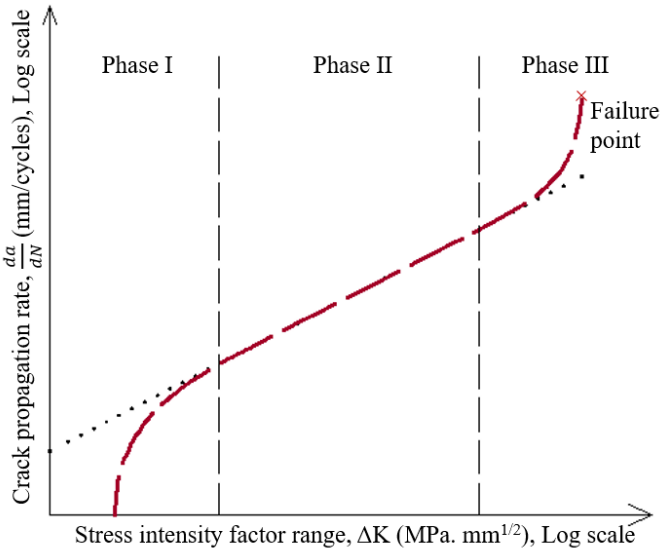

Fig. 1.3 Generalized Paris-Erdogan Law for calculating crack growth rate [12].

Some structures which are subjected to multiaxial loadings are likely to experience a mixed-mode fracture. In fracture mechanics, the modes of failure can be distinguished into three different types (see Fig. 1.5). The fracture under crack opening loads is called mode-I; the one under in-plane shear loading is mode-II fracture; mode-III propagation is due to out-of-plane shear loading. The SIFs observe under the combination of those loadings are called mixed-mode SIFs (MM-SIFs). In-service life, the structures may be subjected to multiaxial loading. In addition, as-welded RS and post-weld treated RS may also induce the mixed mode fracture as the RS distribution is non-uniform. It is also crucial to investigate the effect of RS on MM-SIFs to study the mixed-mode fracture and growth rate in practical applications.

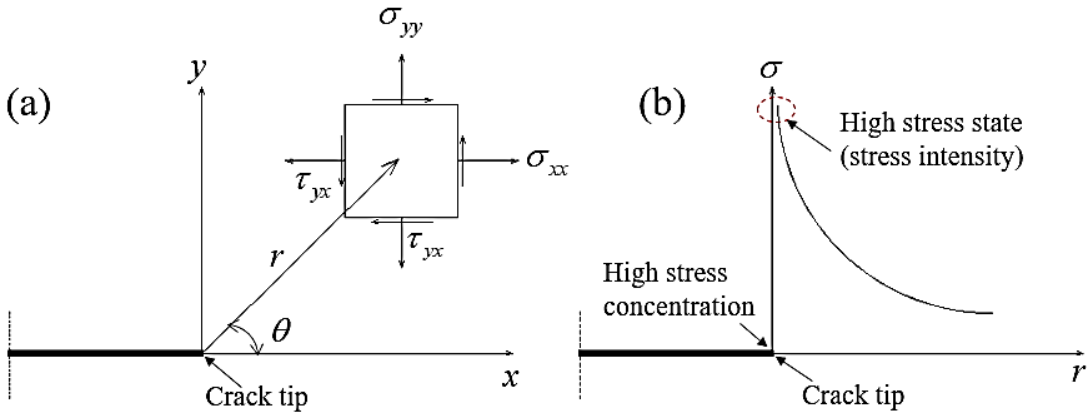

Fig. 1.4 Stress state near the crack tip. (a) Definition of the polar coordinate axis ahead of a crack tip, and (b) stress singularity at the crack tip.

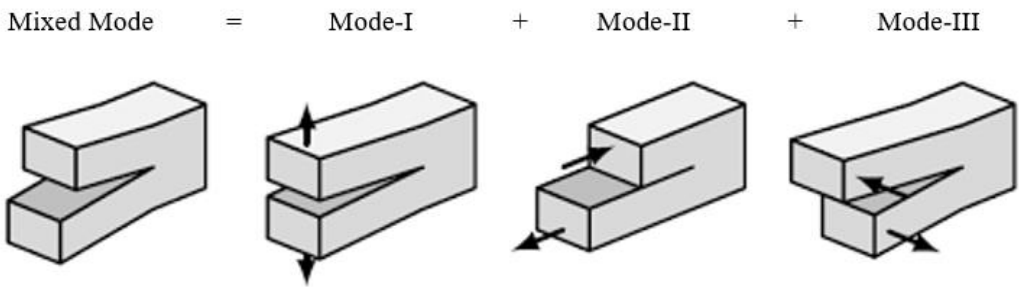

Fig. 1.5 Illustration of mixed-mode fracture in a through-thickness cracked body [13].

1.2 State of the art

1.2.1 Fatigue life estimation of welded structures

Most of the studies employ the S-N approach to estimate the fatigue life of a welded structure. For example, Sun et al. [14] investigated the fatigue life of T-welded joints using experimental and analytical methods considering the effect of boundary conditions. Fatigue assessment of local stresses at fillet welds around plate corners was studied in the work of Fricke et al. [15] considering the notch stress effect. On the other hand by the fracture mechanics approach, Tanaka et al. [16] simulated the crack propagation of T-joints under tensile and bending loading using finite element analysis (FEA). Nevertheless, those previous works did not consider the effect of welding RS in the FCP assessments. On the other hand, Gadallah et al. [17] investigated the influence of welding heat input and welding RS on SIFs and FCP for butt-welded joints. Tchoffo Ngoula et al. [18] simulated the fatigue crack growth in cruciform welded joints by using the node release technique and discussed the effect of welding RS and the weld toe geometry.

Nowadays, the undesirable high tensile RS can be reduced by using post-weld treatment methods and HFMI is one of the popular techniques. For optimal effect of the HFMI treatment, recommendations and guidelines provided by International Institute of Welding (IIW) can be considered [6,19]. Experimental studies are usually costly, and to study several aspects of the HFMI treatment, various numerical simulation procedures were proposed by different scholars [7–11,20–24]. To improve the numerical simulations of HFMI treatment, Ernould et al. [20] reviewed different approaches to performing HFMI simulations and they validated the results from numerical simulations with the experimental results. The stability of the compressive

RS under cyclic loadings was investigated by Leitner et al. [7], Ruiz et al. [21], and Mikkola et al. [25]. The previous studies regarding HFMI treatment showed that this method offers a significant improvement in the fatigue strength of welded structures [19,26].

To prove the effectiveness of HFMI application, several studies on fatigue life estimation were conducted. Yildrim et al. [9] and Leitner et al. [26] studied the fatigue assessment of HFMI-treated welded structures using the nominal and notch stress approach. Leitner et al. [27] also evaluated crack propagation of HFMI-treated welded joints in which fracture parameters were calculated using the weight function method, and they proved the rehabilitation of welded structures after the HFMI treatment. The fatigue life of the HFMI-treated welded joint was evaluated using the superposition concept and Paris-Erdogan equation by Kim and Kim [8], and the weld toe magnification factor for the HFMI-treated joint was also proposed in that study.

In the previous works, for estimating the fatigue life of as-welded and HFMI-treated joints by fracture mechanics approach, simplified stress distributions are usually considered using the weight function method. Although the final stage of brittle fracture is mostly observed as mode-I fracture, the nature of mixed-mode fracture under multi-axial loading and the effect on fatigue life has not been revealed in numerical studies. The reason behind this is the lack of a reliable numerical calculation system that can consider non-uniform, multi-axial loadings subjected to cracked bodies with complicated geometries.

1.2.2 SIF evaluations considering welding RS

To ensure the structural integrity of welded structures in-service, flaw assessments are conducted on a fitness-for-service basis using the guidelines and recommendations provided by welding institutes [6,28]. Still, welded structures that are subjected to cyclic loadings are at a high risk of failure due to fatigue damage. Fatigue strength of the welded structures is mostly affected by the welding RS followed by the flaws. Nevertheless, the previously reported calculation systems barely consider welding RS as well as multiaxial loadings in the SIF evaluations. The following gives a review of the evolution of SIF calculation techniques under arbitrary stress distributions.

SIFs for various structures can be calculated using different analytical [29–36], numerical methods [4,16,17,37–48] and also combined analytical and numerical approach [49–51]. To calculate the SIFs under arbitrary loadings like welding RS, the weight function method is a computationally efficient approach. The method was firstly developed by Bueckner [29] and Rice [52] to empower the evaluation of SIF without needing repetitive analysis for each geometry and loading condition. It has proven efficient in the SIF evaluation for various loading conditions when WF's analytical solution is available [35,36,53,54]. Most of the literature used the weight function method to calculate SIFs under the influence of RS as a large number of weight function equations are available for different cracked geometries [6,55,56]. However, the analytical solutions have been established for very limited cases, and it is difficult to perform its weighted integral for cases with complicated crack face traction (CFT) distribution. Consequently, only mode-I SIFs of simply-shaped cracks for simple CFT distributions were analyzed in most of the studies.

This problem was addressed by Besuner et al. [57] and Shiratori et al. [58–60], and as a countermeasure, the influence function method (IFM) was developed. IFM was used to analyze two-dimensional (2D) and three-dimensional (3D) surface crack problems by using analytical equations and computer programs [57,61–64]. The IFM is based on the weight function method which is used for estimating SIFs for cracks in arbitrary stress distributions. In IFM, the weighted integral is discretized by using influence coefficients (ICs), which are SIFs at a crack front node (SIF target node) for unit distributed load (UDL) applied at each FE node (UDL application node) on the crack face. IC can be calculated numerically for arbitrarily shaped cracks, and the integral is replaced by the total sum of the product of IC and CFT.

Besuner et al. [57] examined the mode-I SIF for surface cracks by IFM in which a unit point load was employed to calculate the IC. On the other hand, Shiratori et al. [61,63] developed the IFM by employing the unit distributed load (UDL) on the crack face to establish the IC database (ICDB). Furthermore, Shiratori et al. have developed an ICDB for several types of surface cracks and this database has been employed in the surface crack analysis program (SCANP) [62]. SCANP can be used to calculate SIFs as well as simulate fatigue crack propagation. In the improved version of SCANP, ICs have been extended to compute SIFs for semi-elliptical surface cracks with aspect ratios

as high as 8.0 [64]. However, the current version of SCANP is only available for mode-I (i.e., K_I-value) problems.

Further, Osawa et al. [65] have developed an automated ICDB calculation system to calculate mode-I SIF for surface cracks in welded joints. However, the accuracy of SIF solutions was insufficient due to the absence of the CFT integral in the applied numerical method. In principle, the IFM can be implemented in tri-axial loading conditions that produce MM-SIFs for cracks in welded joints. However, the developed ICDB calculation system was only valid for mode-I cracks in flat plates.

During the service life of a structure, multiaxial loadings will probably be experienced [66,67]. Especially in T-joints, due to unsymmetrical geometry about the weld toe, considerable values of mode-II and -III SIFs are also observed even under uniaxial applied loading. In addition, welding RS are generally non-uniform on the crack face and have a significant influence on the fatigue life estimation of welded joints [17,44,47]. In typical welding RS distribution, transverse and longitudinal stresses are dominant components that could lead to mixed-mode fracture. Therefore, while analyzing the fracture parameters of T-joints, MM-SIFs should be considered.

1.3 Specific objectives

Given the literature gap, firstly, a fully-automated IFM-based MM-SIF calculation system was developed in this study. The existing IFM was upgraded not only in the calculation efficiency but also in the accuracy of MM-SIF solutions by integrating the CFT integral in the SIF calculations. The developed numerical IFM (NIFM) was applied to evaluate MM-SIFs of surface cracks under multiaxial loadings, to estimate the fatigue life of as-welded joints considering welding RS, and to compare the effect of RS on MM-SIFs of as-welded and HFMI-treated joints. To obtain the optimum structure design, the behavior of fatigue life under different loading conditions and welding conditions should be examined and compared. The numerical NIFM system employed in this article makes such investigations easier in which welding specialists can evaluate SIFs for various welding conditions without repeating the fracture analysis.

In addition, this study introduced a new approach for the weld modification factor (μ_k) method to evaluate MM-SIFs of cracked T-joints under arbitrary stress distributions. The μ_k formulae were developed based on the NIFM and the ICs. The

MM-SIFs of T-joints under arbitrary stress distributions can be calculated by multiplying the proposed μ_k and the flat plate SIFs obtained by NIFM.

The previous works reported by different scholars give the relation of SIFs of a welded joint and flat plate for a specific loading: membrane, shear, or bending. However, the μ_k is developed to obtain the relation of MM-SIFs of the welded joint and flat plate under the same CFT. By employing our proposed technique and developed formulae for μ_k, the geometric effect on MM-SIFs of surface cracks in T-joints can be calculated readily. Therefore, the proposed μ_k can be employed to get MM-SIFs of welded joints under arbitrary stress distributions.

1.4 Framework of the thesis

This thesis can be read as a combination of four different parts: problem definition, methodology development, application of the developed calculation system, and μ_k methodology. The corresponding chapters to each part are categorized in Fig. 1.6.

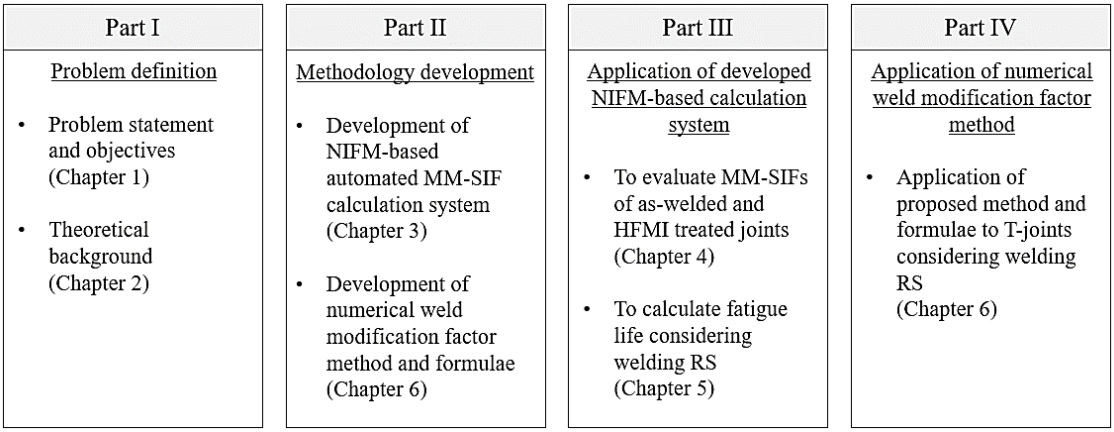

Fig. 1.6 Structure of the thesis.

1) In Chapter 1, the background on fatigue failures of welded joints, post-weld treatment methods to improve the fatigue strength, and the estimation of fatigue life of the welded joints are explained. Based on the challenges in evaluating the fatigue life of the welded components given in previous literature, the objectives of this study are established.
2) Chapter 2 includes the basic theories and methodologies related to this work. Some of the SIF evaluation methods which are corresponding to further development in the following chapters are explained in detail.

3) Stating in Chapter 3 is the development of the NIFM-based SIF calculation system and the verification of the proposed calculation system. Flat plates with surface cracks under uni-axial and shear loadings are employed to show the effectiveness and accuracy of MM-SIF solutions obtained by using the proposed system. The solutions given by the developed system are compared with those given by the analytical and other numerical analyses.
4) Then, the application of the NIFM-based SIF calculation system to evaluate MM-SIF solutions of as-welded and HFMI-treated welded joints is demonstrated in Chapter 4. T-joints with surface cracks are used as numerical examples. The RS estimated from numerical welding and HFMI analyses, which are described in Appendix A, are considered to calculate MM-SIFs.
5) In Chapter 5, fatigue life estimation of welded joints considering welding RS is presented. Surface-cracked T-joints are used to estimate the SIFs with and without welding RS. The details of welding RS estimation are presented in Appendix B.
6) Based on the difficulties experienced in MM-SIF calculation of welded components, a more efficient and accurate approach to calculate MM-SIFs of welded joints under arbitrary stress distributions is proposed in Chapter 6. A numerical weld modification factor (μ_k) is proposed based on the NIFM for semi-circular surface cracks in T-joints, and the formulae are driven using the regression models. The μ_k and its formulae are verified and validated by comparing with the solutions obtained by the commercial FE analysis code (MSC Marc, 2014) and those by the well-established solutions.
7) Chapter 7 summarizes the fundamental findings of the work in this study. The suggestions which will improve the current work are also described for further work.

CHAPTER 2

Basic theoretical background

2.1 SIF evaluation methods

2.1.1 The IFM

By using the fracture mechanics approach, the FCP of welded structures has been widely studied using experiments [14,68], numerical methods [16,17], and analytical methods [69,70]. Accurate evaluation of SIFs plays an important role in the reliable FCP assessment. Analytical and numerical methods are widely used to calculate the SIF solutions [28,45,47,58,71–75]. However, accurate estimation of MM-SIFs for cracks in welding RS fields under multiaxial loading is still challenging work for researchers. Many studies have reported a variety of calculation techniques for SIFs under arbitrary stress distribution. Among them, the IFM has been claimed to be one of the most reliable methods for the evaluation of SIFs under arbitrary stress distribution. For decades, the IFM has been widely employed in the calculation of SIFs and was modified to improve the accuracy of SIF solutions, and the efficiency of calculation procedure [48,57–64,75,76].

In the IFM proposed by Besuner et al. [57], the SIFs are evaluated using Eq. (1) in which $h(x, geo.)$ represents the influence function (IF), $\sigma(x)$ is the load on the pressurized crack, and L denotes the straight crack face boundary parallel to the x-axis. The IFs are calculated using established equations as a function of the crack geometry or crack mouth opening displacement. And, $\sigma(x)$ is extracted from the uncracked model's stress field on the crack face. However, this approach requires establishing reliable IF equations for each cracked geometry.

$$K = \int_{L} h(x, geo.)\sigma(x)dx \tag{1}$$

For this reason, Shiratori et al. [58] developed a discretized IFM in which the IFs are denoted as ICs. The ICs are the SIFs at the target SIF evaluation points (*Q-th*) due to UDL at the nodes (*P-th*) on the crack face. The summation of products of ICs and loads are the SIF solutions as shown in the following equation [58]. The definitions of *Q-th* and *P-th* nodes on the crack face are illustrated using a surface-cracked flat plate in Fig.

2.1. By using the ICs induced by the UDL, SIF evaluation becomes easier without the need to establish the IF equation.

$$K_Q = \sum_{P=1}^{n} K^{QP} \sigma^P \tag{2}$$

The value of UDL at the chosen node is unity and that for the other nodes is zero. UDL is determined by calculating equivalent nodal forces where normal stress distribution is calculated by 2D quadratic shape function as in Eq. (3) [65]. As the UDL is interpolated on the element face, the stresses become one or zero at the nodes and non-zero for other parts on the element face (see Fig. 2.2). The normalized coordinate system (ξ, η) on element face of a 20-noded hexahedral element is shown in Fig. 2.2.

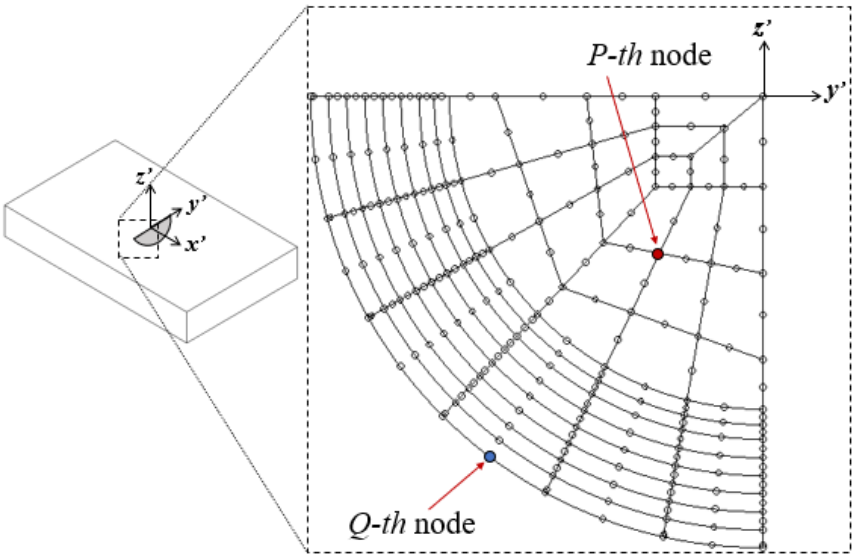

Fig. 2.1 Notation of crack face node and crack front node on a surface crack in the IFM.

$$\begin{aligned} N_i(\xi,\eta) = {} & \frac{1}{4}\xi_i^2\eta_i^2\left\{\left(1+\xi_i\xi\right)\left(1+\eta_i\eta\right)\right\} - \left(1-\xi^2\right)\left(1+\eta_i\eta\right) - \left(1-\eta^2\right)\left(1+\xi_i\xi\right) \\ & + \frac{1}{2}\eta_i^2\left(1-\xi^2\right)\left(1-\xi_i\right)\left(1+\eta_i\eta\right) + \frac{1}{2}\xi_i^2\left(1-\eta^2\right)\left(1-\eta_i^2\right)\left(1+\xi_i\xi\right) \end{aligned} \tag{3}$$

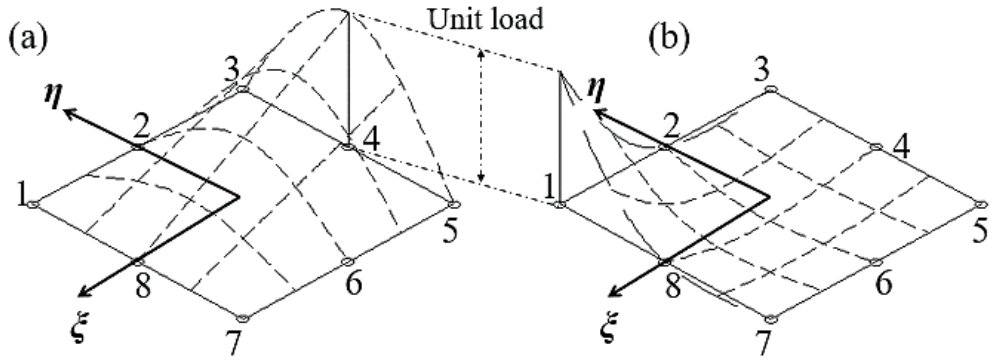

Fig. 2.2 Application of UDL on the crack face. (a) UDL on an element face due to a unit load at the mid node, and (b) UDL on an element face due to a unit load at the edge node [75].

Later, Shiratori et al. [61] expanded the IFM to evaluate MM-SIFs using the following equation:

$$\begin{Bmatrix} K_I^Q \\ K_{II}^Q \\ K_{III}^Q \end{Bmatrix} = \sum_{P=1}^{n} \begin{Bmatrix} K_{Ix}^{QP} & K_{Iy}^{QP} & K_{Iz}^{QP} \\ K_{IIx}^{QP} & K_{IIy}^{QP} & K_{IIz}^{QP} \\ K_{IIIx}^{QP} & K_{IIIy}^{QP} & K_{IIIz}^{QP} \end{Bmatrix} \begin{Bmatrix} \sigma_x^P \\ \sigma_y^P \\ \sigma_z^P \end{Bmatrix}, \tag{4}$$

where K_I^Q, K_{II}^Q, and K_{III}^Q denote the mode-I, -II, and -III SIFs at the SIF target points (*Q-th* nodes) due to applied arbitrary loading; K_{Ix}^{QP}, K_{Iy}^{QP}, and K_{Iz}^{QP} represent mode-I, - IC values which are the MM-SIFs at the SIF target points due to UDL (*x*, *y*, *z* traction vectors); σ_x^P, σ_y^P, and σ_z^P are the traction force vectors (TFV) on the crack face nodes (UDL application nodes, *P-th* nodes) which are calculated using the superposition principle. While using IFM in the previous works, the ICs are usually calculated using Spreadsheets which takes a lot of man-hours to establish one ICDB for a cracked model. Therefore, an automated SIF calculation software based on IFM, SCANP was developed by Shiratori et. al. [62] in which ICDBs of flat plates and cylinders are included for surface cracks with different aspect ratios. However, to calculate the MM-SIFs for complicated cracked bodies and non-uniform loadings, the IFM needs to be upgraded. This study proposed a fully automated NIFM-based SIF calculation system to evaluate MM-SIFs of different cracked bodies under multi-axial loading, and the proposed methodology is described in Chapter 3.

2.1.2 The interaction integral method (IIM)

The IIM is one of the famous numerical methods to calculate the SIFs which provides a more general and simpler analysis procedure than the earlier virtual crack extension method [45,77]. Moreover, the method has the capabilities to easily extract MM-SIFs and T-stresses compared to the domain integral method. It uses the computed displacements, stresses, and strains for post-processing to represent the correct equilibrium state for the specified boundary-value problem. It also provides auxiliary field quantities such as SIFs or T-stresses. The computation of J-integral for the superimposed actual and auxiliary fields state leads to a conservation integral that enables the direct calculation of SIFs [78]. The superimposed integrals are then divided into three parts: domain integral for the actual state, domain integral for the auxiliary state, and domain form of the interaction integral.

The local coordinate system at the crack front position *s* is shown in Fig. 2.3 [79]. The domain form of the interaction integral at a location *s* along a 3D crack front, $\bar{I}(s)$, [77] is defined as:

$$\begin{aligned}\bar{I}(s) = &\int_V \left(\sigma_{ij} u^{aux}_{j,1} + \sigma^{aux}_{ij} u_{j,1} - \sigma_{jk}\varepsilon^{aux}_{jk}\delta_{1i}\right) q_{,i} \\ &+\int_V \left[\sigma_{ij}\left(u^{aux}_{j,1i} - \varepsilon^{aux}_{ij,1}\right) + \sigma^{aux}_{ij,1} u_{j,1}\right] q dV - \int_{S^+ + S^-} t_j u^{aux}_{j,1} q dS\end{aligned}, \tag{5}$$

where the superscript '*aux*' represents the auxiliary field components, u_j denotes displacement components, δ_{ij} is the Kronecker delta, *V* and *S* represent finite volume and finite surface, respectively, *q* is weight function and t_j are CFT components. S^+ and S^- represent the upper and lower crack face surfaces, respectively. The definitions of these parameters are given in more detail in the WARP3D user's guide [77]. The CFT-integral, $-\int_{S^+ + S^-} t_j u^{aux}_{j,1} q dS$, contributes significantly to the preciseness of evaluated SIFs [17,71,79]. After computing $\bar{I}(s)$, the value of interaction integral *I*(*s*) at any location *s* along the 3D crack front is calculated as in Eq. (6). MM-SIFs are then calculated using *I*(*s*) as given in Eq. (7).

$$I(s) = \frac{\bar{I}(s)}{\int_{L_c} q(s)ds} \tag{6}$$

$$I(s) = \frac{1}{E^*}\left(2K_I K_I^{aux} + 2K_{II} K_{II}^{aux}\right) + \frac{1+\nu}{E}\left(2K_{III} K_{III}^{aux}\right) \tag{7}$$

Where L_C denotes length of the crack front segment. K_I^{aux}, K_{II}^{aux}, and K_{III}^{aux} represent auxiliary mode-I, -II, and -III SIFs respectively, and E^* and E are Young's modulus for the plane stress and plane strain conditions, respectively. MM-SIFs are treated as plane stress conditions at the crack mouth locations and as plane strain conditions for nodes along the crack front except at the crack mouth locations. Relationships between K_I, K_{II}, and K_{III} can be obtained by giving the selected appropriate values for auxiliary modes of SIFs:

$$K_I = \frac{E^*}{2} I(s),\ K_{II} = \frac{E^*}{2} I(s),\ K_{III} = \frac{1+\nu}{E} I(s). \tag{8}$$

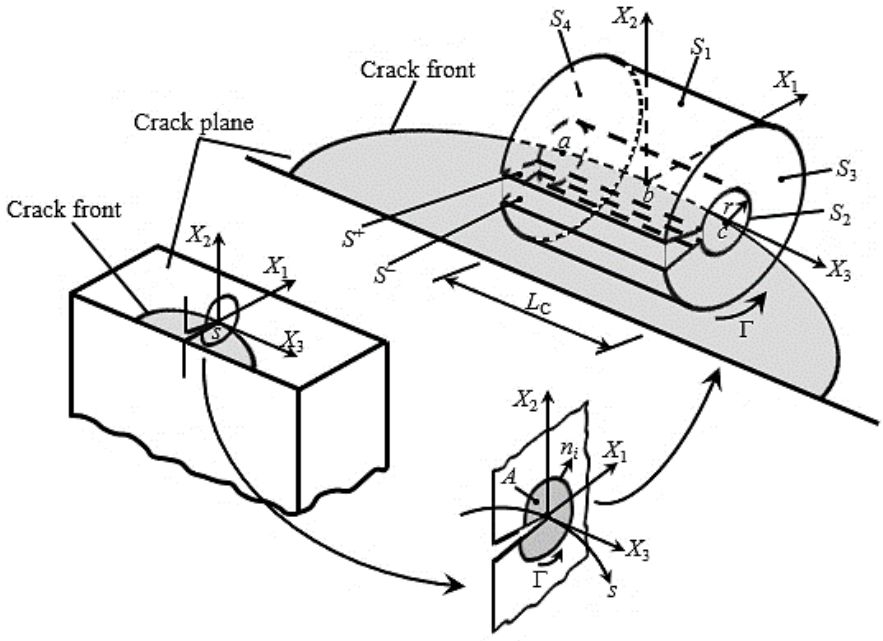

Fig. 2.3 A finite volume for use in IIM formulation at a crack front location $s = B$ that extends over the length L_C from point A to C. [43]

The IIM is the most convenient method available to extract MM-SIFs. And, the CFT integral included in the numerical integration procedure also increases the accuracy of MM-SIF solutions. Due to numerical integration procedures and less study on IIM in the last decade, IIM has not been set up yet in commercial software (e.g. MSC Marc). However, WARP3D, an open-source code, provides IIM to solve 3D fracture mechanics problems. In this study, WARP3D-IIM was modified so that it can consider six components of traction stresses on the crack face (details are given in Chapter 3).

2.2 Welding and post-weld treatment analyses

2.2.1 Welding analysis

In this study, the RS induced by the welding process was estimated numerically using the in-house code JWRIAN. JWRIAN was developed by The Joining and Welding Research Institute (JWRI) of Osaka University [80,81]. The iterative substructure method was applied in this code to perform high-speed implicit thermal elastic-plastic finite element analysis (TEP-FEA). The analysis procedure includes three steps.

In the JWRIAN code, to reduce the computation time, the whole welding structure is divided into weakly non-linear regions and strongly non-linear regions. The iterative substructure method ensures continuity of tractions between those regions. Sequentially coupled thermal and mechanical FEA is carried out during the simulation. First, temperature history for each node is calculated by FE heat transfer simulation. The volumetric ellipsoid heat source is applied in the thermal analysis. Based on the weld profile, the transferred heat source into the weld profile is changed, e.g., the half-ellipsoid volumetric heat source for 45° fillet welds (see Fig. 2.4) where a_f and a_r represent the front and rear lengths of the heat source, d and b are the depth and half-breath of the heat source model, respectively. The thermal analysis is carried out to establish thermal profiles followed by stress analysis which examines the displacement, stress, and strain based on the thermal profiles. The calculated WRS is examined from the final stage of stress analysis performed by JWRIAN. The reliability and accuracy of predicted WRS using JWRIAN were validated with the experimental results for different welded joint geometries in previous works [45–47,82–86].

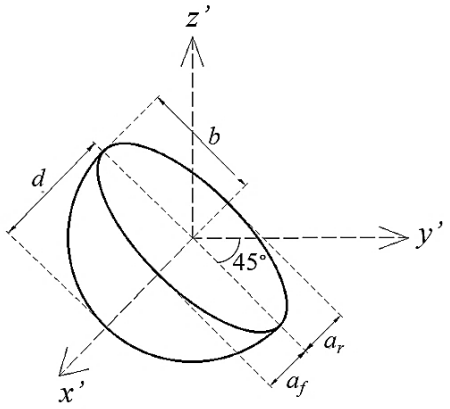

Fig. 2.4 Half ellipsoid volumetric heat source model [86].

2.2.2 HFMI simulation

HFMI has been widely used as an effective post-weld treatment in welding communities. It is also proven that HFMI treatment significantly increases the fatigue life of welded joints [7,9,11,19,24,27]. In HFMI treatment, a hardened metal pin with a spherical tip is employed for peening the weld transition region with a high frequency. This process induces local plastic deformation around the peened region, reducing the notch effect at the weld toe. It also induces compressive RS and local work hardening. All of these lead to improving the fatigue strength of the structure. For the assessment of fatigue strength of HFMI-treated welded structure, reliable numerical calculations are needed to accurately estimate the induced RS field.

For structural problems subjected to impact loadings with high frequency, explicit dynamics analysis is suitable as it can accurately simulate highly complex non-linear behavior for a short time [87]. In previous studies, numerical simulations of HFMI treatment are performed using commercial software such as Abaqus©Explicit, or the Explicit Elastic-Plastic FEA code MSC Dytran [7,23,25]. In HFMI-treatment simulations, two types of numerical simulations, force-controlled simulations (FCS) and displacement-controlled simulations (DCS) are generally used. However, it is observed that DCS gives more accurate results compared to FCS [10]. Therefore, in this study, DCS was chosen to perform HFMI simulation using the explicit code MSC Dytran.

The accuracy of the predicted RS strongly depends on the hardening law used in the analysis. It is needed to consider a material model that can correctly represent the

material behavior and evaluate the RS induced by HFMI. In this study, Chaboche's kinematic hardening law [23] is adopted (see Eq. (9)).

$$J_2 = (\boldsymbol{\sigma} - \boldsymbol{\alpha}) = \sigma_0 \tag{9}$$

Where $\boldsymbol{\sigma}$ represents the acting stress tensor, $\boldsymbol{\alpha}$ is the back-stress tensor, and σ_0 denotes the yield stress (scalar) value. The back-stress tensor, $\boldsymbol{\alpha}$, is calculated using Eq. (10) [23]:

$$d\alpha = \sum_{i=1}^{M} d\alpha_i' d\alpha_i = C_i \frac{d\varepsilon^p}{\sigma_0}(\sigma - \alpha) - \gamma_i \alpha_i d\varepsilon^p \,, \tag{10}$$

where M is the number of kinematic hardening components, set as 2 in this study, and i is the component number. C_i and γ_i denote the material parameters and $d\varepsilon^p$ the equivalent plastic strain increment. σ_0 is defined to consider the combined isotropic-kinematic hardening and strain rate dependency.

CHAPTER 3

Development of mixed-mode SIF calculation system

3.1 Introduction

This chapter presents the development of a NIFM-based MM-SIF calculation system and validation for its application in evaluating MM-SIFs under multi-axial loading. To accurately calculate the MM-SIFs of complicated structures subjected to arbitrary loading, a reliable and efficient MM-SIF calculation system is necessary. Given the literature review of SIF evaluation methods in Section 1.2, such methodology is still needed to develop. On the other hand, IFM is available to calculate SIFs under arbitrary stress distributions. Despite its utility, the man-hours required to establish ICDB for the existing analytical IFM calculation are nonpractical. For this reason, a fully-automated NIFM-based MM-SIF calculation system was developed in this study. The developed system was verified using the semi-infinite flat plate cracked bodies under remote tensile and shear loadings.

3.2 Methodology

The developed NIFM is a numerically discretized weight function method where the ICDB and CFT are superimposed. In the conventional weight function method, an analytical expression is established for each cracked geometry and the weight function values are superimposed with simplified stress distributions on the crack face. On the other hand, in the NIFM, the MM-SIFs due to UDL on the crack face are calculated and saved as ICDB. These IC values are employed instead of fixed weight function values. Moreover, the CFT on the crack face includes six components of stress values which assures the accuracy of calculated SIFs.

In the previous IFM equations proposed by Shiratori et al. [61], only TFV is considered in the MM-SIF evaluations. However, in this study, the MM-SIFs are estimated for the six components of traction stresses on the crack face. Therefore, the equations of NIFM are derived as in the following equations.

$$K_I^Q = \sum_{i,j} \sum_P C_I^{ij,QP} \sigma^{ij,P}$$
$$K_{II}^Q = \sum_{i,j} \sum_P C_{II}^{ij,QP} \sigma^{ij,P} \quad (11)$$
$$K_{III}^Q = \sum_{i,j} \sum_P C_{III}^{ij,QP} \sigma^{ij,P}$$

Where K_I^Q, K_{II}^Q, and K_{III}^Q denote the mode-I, -II, and -III SIFs at the SIF target points (*Q-th* nodes) due to applied arbitrary loading; $C_I^{ij,QP}$, $C_{II}^{ij,QP}$, and $C_{III}^{ij,QP}$ represent mode-I, -II, and -III IC values which are the MM-SIFs at the SIF target points due to UDL (six-components); $\sigma^{ij,P}$ are the six-components of CFT on the crack face nodes (UDL application nodes, *P-th* nodes) which are calculated using the superposition principle. Allocations of nodes and definition of UDL are illustrated in Figs. 2.1 and 2.2. The following sections explain the detail of the calculation procedure for IC and CFT.

3.2.1 Calculation of ICDB

The IC values, $C_{I,II,III}^{ij,QP}$, and the CFT, $\sigma^{ij,P}$, are superimposed to evaluate the SIFs along the crack front. The UDL for each node on the crack face is employed to calculate the IC values using the IIM. The efficiency of IIM to extract MM-SIFs is one of the advantages over the other numerical methods [45,77]. Further, it was demonstrated that the accuracy of SIF solutions is improved when the CFT integral is considered in the numerical procedure [4,17,45,47,71,88]. For this reason, the CFT-integral is included in the employed IIM in order to achieve an accurate estimation of MM-SIFs for cracks in arbitrary stress fields [4,45,71]. (The detailed theoretical explanation of IIM is described in Section 2.1.2.)

WARP3D [77] is a public domain code used for 3D fracture mechanics analysis in which the IIM considering the CFT integral term is accessible. The domain integral method available in commercial software does not support the CFT integral (e.g., MSC Marc [89]). Only pressure loading can be applied to the center of an element face using WARP3D in its current release. The applied pressure loading is internally converted into three components of TFV. The same values are then given to all Gaussian points and perform the CFT-integral. Gadallah et al. [45,71] modified the original WARP3D code so that the TFV can be applied at the element face's center instead of pressure

loading and perform the CFT-integral for non-uniform stress fields. Based on the WARP3D-TFV proposed by Gadallah et al. [45,71], the type of loading and format of the input file are modified to be used in the current study. On the other hand, six traction stress components (TSC) can be applied at each node on the element face of the crack face in the modified code, WARP3D-TSC. By using the modified WARP3D-TSC, different traction stresses on the crack face are considered in the evaluation of CFT-integral to obtain accurate and reliable MM-SIFs under arbitrary stress distribution. Table 3.1 shows the differences between the original WARP3D and the modified ones.

Table 3.1 Data of original WARP3D code and modified codes.

WARP3D versions	Target location	Quantity
Original WARP3D [77]	Element face's center	Pressure
WARP3D-TFV [45]	Element face's center	Traction force vectors
WARP3D-TSC	Each Gaussian point	Six components of traction stresses

Using the modified IIM, the ICs are calculated for each UDL and are then saved to the ICDB. Once the ICDB for UDL is established, SIFs of surface cracks in arbitrary stress fields can be calculated [63].

Hereafter, the procedures to calculate IC values are listed:

1) Firstly, a cracked FE mesh with desired configurations is constructed.
2) A WARP3D input file for the target FE mesh model is prepared.
3) Using a developed shell script, the UDL application nodes and SIF target nodes are searched. Then, the unit traction stresses data for each UDL application node are prepared automatically.
4) For each UDL application node, six components of unit traction stresses ($t^{ij,P}$) are employed and MM-SIFs for all SIF target nodes are evaluated using the IIM.
5) The MM-SIF solutions, which are known as $C_{I,II,III}^{ij,QP}$, are saved to the ICDB.

The example of a developed ICDB for one UDL application node is shown in Table 3.2 [90]. In the exampled table, the UDL application node (*P-th* node, refer to Fig. 2.1)

has a node ID of 28. It can be seen from the first row of Table 3.2 that when $t^{11,28}$ is applied, IC values ($C_I^{ij,QP}$, $C_{II}^{ij,QP}$, and $C_{III}^{ij,QP}$) are calculated for three SIF target nodes at φ=0°, 45°, and 90°. The same analysis procedure as in $t^{11,28}$ is followed for other traction stress components, and all UDL application nodes.

Table 3.2 Example of a developed ICDB for one UDL application node.

			SIF target nodes (*Q-th*) at φ location		
UDL application node ID. (*P-th*)	Unit traction stress component ($t^{ij,P}$)	IC values ($C_{I,II,III}^{ij,QP}$)	0°	45°	90°
28	11	$C_I^{ij,QP}$	-5.5E-03	-9.6E-03	-1.3E-02
28	11	$C_{II}^{ij,QP}$	-1.5E-08	-1.0E-08	-8.7E-09
28	11	$C_{III}^{ij,QP}$	4.5E-08	1.6E-09	-3.4E-08
28	22	$C_I^{ij,QP}$	3.8E-24	1.2E-24	-1.6E-24
28	22	$C_{II}^{ij,QP}$	-8.1E-19	-3.9E-18	2.5E-18
28	22	$C_{III}^{ij,QP}$	8.8E-19	3.4E-18	-1.6E-18
28	33	$C_I^{ij,QP}$	-2.4E-23	6.4E-24	2.0E-23
28	33	$C_{II}^{ij,QP}$	4.2E-18	-1.4E-17	-3.3E-17
28	33	$C_{III}^{ij,QP}$	-1.2E-17	-1.1E-17	-6.3E-17
28	12	$C_I^{ij,QP}$	5.0E-09	3.0E-09	-1.6E-09
28	12	$C_{II}^{ij,QP}$	-1.9E-03	-4.6E-03	2.8E-03
28	12	$C_{III}^{ij,QP}$	1.5E-03	2.9E-03	1.2E-02
28	23	$C_I^{ij,QP}$	1.3E-24	-5.1E-24	-3.6E-24
28	23	$C_{II}^{ij,QP}$	1.7E-19	1.5E-17	7.6E-18
28	23	$C_{III}^{ij,QP}$	2.7E-18	-3.5E-18	2.8E-17
28	13	$C_I^{ij,QP}$	9.2E-09	-7.1E-09	-1.5E-08
28	13	$C_{II}^{ij,QP}$	-4.1E-03	8.8E-03	1.9E-02
28	13	$C_{III}^{ij,QP}$	4.5E-03	3.3E-03	4.3E-02

3.2.2 Calculation of CFT

The second part of the NIFM equation, $\sigma^{ij,P}$, represents the CFT which is the traction stresses on the crack face. The approach of using traction stresses is based on the superposition principle. Fig. 3.1 states the evaluation of SIF under CFT following the superposition principle which can be expressed using the following equation:

$$K_I^{(a)} = K_I^{(b)} - K_I^{(c)}. \tag{12}$$

Where, $K_I^{(c)}$ is zero as the SIF due to remote and CFT loadings cancel out each other. From which, it can be deduced that SIF solutions ($K_I^{(a)}$) of a cracked body obtained by applying the CFT on the (fictitious) crack face of a non-cracked body are equal to those calculated for a cracked body under the remote loading ($K_I^{(b)}$) [2].

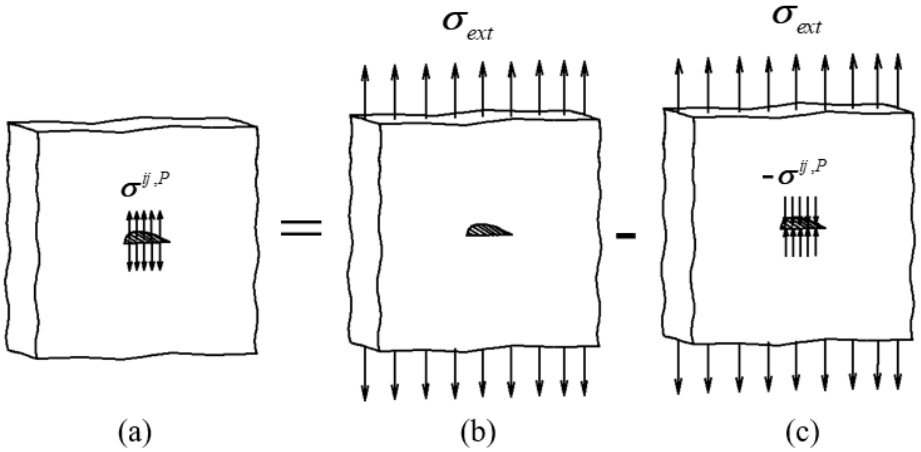

Fig. 3.1 Determination of SIF under CFT loading using the superposition principle. (a) A cracked body subjected to the stress field ($\sigma^{ij,P}$), (b) a geometrically identical cracked body subjected to a remote tensile loading (σ_{ext}), and (c) a geometrically identical uncracked model with a stress field ($-\sigma^{ij,P}$) produced by the applied remote loading (σ_{ext}).

$\sigma^{ij,P}$ can be calculated by averaging, translation, or interpolation of element stresses obtained by FEA using the uncracked body. It can be any arbitrary stress distribution, for example, RS distribution, multi-axial stress distribution, or measured stress distribution. Once the ICDB for a specific model has been established, the SIFs under arbitrary stress distribution can be readily calculated by applying the given CFT.

3.3 Verification of ICDB for semi-infinite bodies (pure mode-I loading)

The adequacy of the constructed ICDB for semi-infinite bodies is verified by using the surface-cracked flat plate model under external tensile loading. The results of SIFs calculated using NIFM are compared with analytical reference solution [34], as well as with the direct solutions and TFV solutions proposed by Gadallah et al. [45].

3.3.1 Model definition

For the sake of simplicity, a simple numerical example is chosen which represents a cracked flat plate subjected to a uniform external tensile loading. The model has a semi-circular surface crack with an aspect ratio of a/c = 1.0, where a and c are the crack depth and half-length, respectively. The model is a square plate of 762 mm on each edge and has a thickness of 381 mm. The dimensions of the model are chosen to be large enough compared to the crack size so that the model can be treated as a semi-infinite body. The external tensile loading, σ_{ext}, is applied in the z-direction.

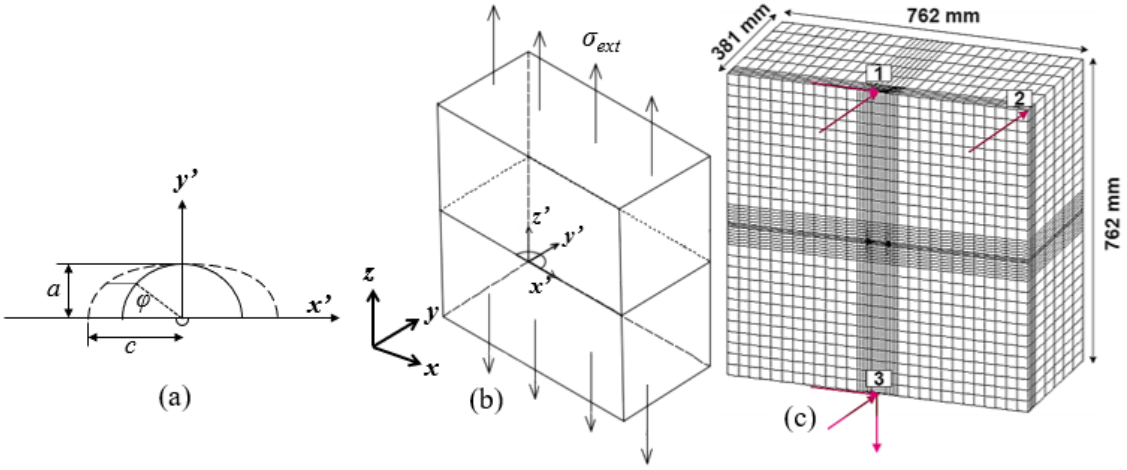

Fig. 3.2. A semi-circular surface crack in a semi-infinite flat plate body. (a) the geometry of the crack face, (b) geometry of the cracked body, and (c) FE model of the cracked body.

Fig. 3.2(a) illustrates the geometry of the crack face where φ represents the crack front location in degrees. The geometric configuration and corresponding FE model are shown in Fig. 3.2(b) and (c). The FE model is generated using 20-noded hexahedral elements. The FE model consists of 91,885 nodes and 21,168 elements. The elements in the vicinity of the crack tip are generated with quarter-point wedge elements to simulate the crack tip singularity ($1/\sqrt{r}$ singularity). Fig. 3.3 shows the FE mesh on

the crack face and at the crack front. Boundary conditions that prevent rigid body motion of the models are adopted. The details of displacement constraints applied in the analyses are given in Table 3.3. u_x, u_y and u_z are displacements in x-, y- and z-directions, respectively. Theree different Poisson's ratios of v = 0.0, 0.3, and 0.49 were used to examine the effect of Poisson's ratio on the SIF solutions.

Table 3.3. Location and type of displacement constraints for pure mode-I loading.

Location of constraints	Nodal Coordinates (mm)	Type of Constraints
Node at point 1	(0, 0, 381)	$u_x = 0$ $u_y = 0$
Node at point 2	(381, 0, 381)	$u_y = 0$
Node at point 3	(0, 0, -381)	$u_x = 0$ $u_y = 0$ $u_z = 0$

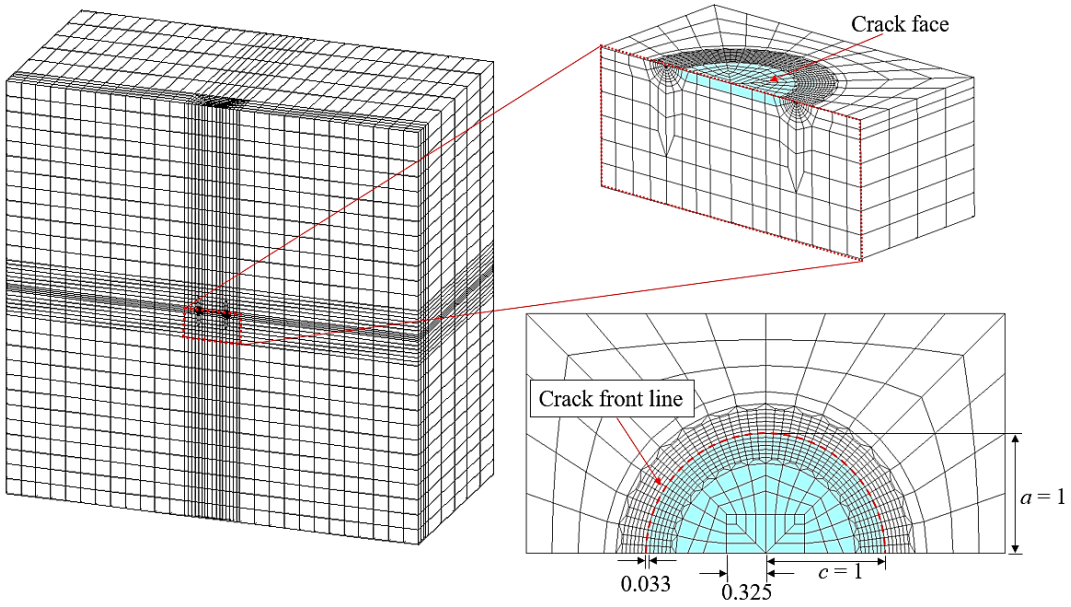

Fig. 3.3. The FE mesh on the crack face and at the crack front, a/c = 1.0.

3.3.2 Results and discussion

Table 3.4 gives the results of SIF solutions for three different Poisson's ratio values (v = 0.0, 0.3, 0.49). The mode-I SIFs calculated using NIFM are compared with the analytical reference solution reported by Noda et al. [34] and Noda et al. [32] as well

as the solutions obtained by Gadallah's technique [45,71]. Gadallah et al. have employed the superposition method in which the following steps were conducted [45,71]:

(1) SIFs are calculated for a flat cracked plate under external loading. SIF solutions obtained in this step are called "external".
(2) Traction stresses that arise over the crack face (namely CFT) are calculated using the same external loading to a geometrically identical non-cracked plate.
(3) Calculated traction stresses in step (2) are then applied with an opposite sign to the crack face for a geometrically identical cracked plate as that used in step (1). SIFs are evaluated using WARP3D-TFV and denoted as "TFV".

The solutions obtained through NIFM are described as "NIFM". Another solution referred from Noda et al.'s work [34] is denoted as "Noda" in which the MM-SIFs are calculated using the body force method. The calculated SIFs are normalized using Eq. (13) [34]:

$$F_I = \frac{K_I^Q}{\sigma\sqrt{\pi a}}, \tag{13}$$

where F_I and K_I^Q represent normalized and calculated mode-I SIF respectively. The locations along the crack front are represented by φ (in degrees) in which $\varphi = 0°$ denotes the crack mouth and $\varphi = 90°$ represents the crack deepest point (see Fig. 3.2(a)).

According to Fig. 3.7, in the case of $\nu = 0.0$ and 0.3, SIF solutions obtained by NIFM are in good agreement with the reference solutions. In the case of $\nu = 0.49$, no solutions were reported by Noda et al. [34], but the SIF solutions were compared with Noda et al. [32] evaluated for $\nu = 0.5$. In this study, $\nu = 0.49$ was chosen instead of $\nu = 0.5$ due to the limitation of WARP3D, calculation of stress fields under plane strain condition. However, the evaluated SIF solutions for $\nu = 0.49$ and those given by Noda et al. for $\nu = 0.5$ are in excellent agreement with a percentage difference of around 0.1.

Figure 3.4 reveals that the larger the value of Poisson's ratio, the larger the values of calculated SIFs along the crack front except in the vicinity of the crack mouth. SIF solutions near the crack mouth behave in a different trend compared to the other nodes

along the crack front. For example, when Poisson's ratio increases, the calculated SIFs at the crack mouth decrease. While the situation is different for the other nodes along the crack front in which by increasing Poisson's ratio, the calculated SIFs increase as well. The percentage difference of the SIFs obtained by NIFM with those given by the reference solutions at the crack mouth is not trivial; however, it is small enough.

Table 3.4. Normalized SIF, F_I, for different Poisson's ratios.

φ (deg.)	v	F_I^{TFV}	$F_I^{external}$	F_I^{NIFM}	F_I^{Noda}	% difference of Noda vs. NIFM
30	0	0.6545	0.6511	0.6545	0.6510	0.54
	0.3	0.6861	0.6827	0.6861	0.6821	0.59
	0.49	0.7306	0.7272	0.7306	0.7300	0.082
60	0	0.6415	0.6375	0.6415	0.6377	0.59
	0.3	0.6663	0.6629	0.6663	0.6627	0.54
	0.49	0.7092	0.7052	0.7086	0.7085	0.01
90	0	0.6387	0.6353	0.6387	0.6352	0.58
	0.3	0.6618	0.6584	0.6617	0.6585	0.48
	0.49	0.7035	0.6996	0.7029	0.7020	0.13

Based on the obtained results, the constructed ICDB is applicable to evaluate SIFs accurately for surface cracks in semi-infinite bodies. In addition, the results obtained by the employed FE model give the precise estimation with those given by Noda which are evaluated based on semi-infinite bodies.

3.4 Verification of ICDB for semi-infinite bodies (pure shear loading)

This section investigates the adequacy of the constructed ICDB for evaluating MM-SIFs in semi-infinite bodies. A surface-cracked flat plate model under pure shear loading was employed. The evaluated MM-SIFs using NIFM are compared with those given by Noda et al. [32] and solutions obtained by Gadallah's technique [45].

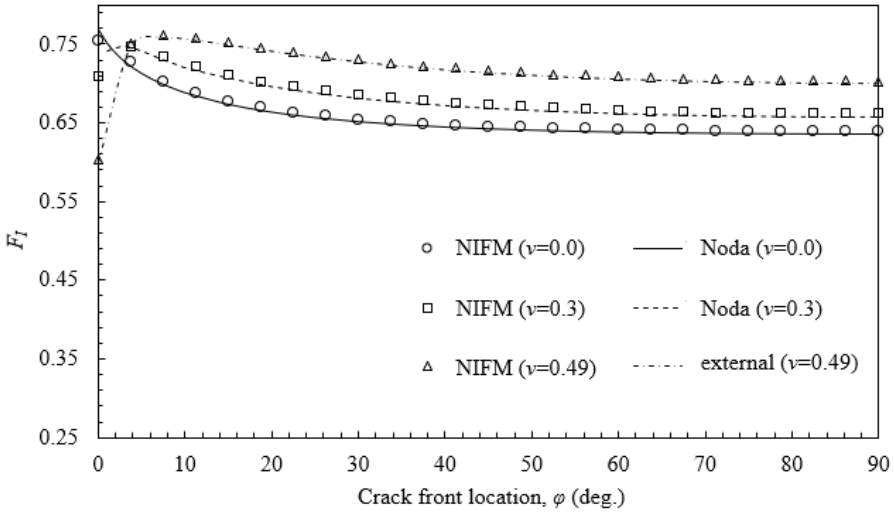

Fig. 3.4. Verification of the SIFs obtained by NIFM with different reference solutions.

3.4.1 Model definition

The surface-cracked flat plate model used in this section has the same geometric configurations as the one described in Section 3.3.1. The only difference is the applied loading and boundary conditions. To induce MM-SIFs, pure shear loading, σ_{xz}, is applied to the flat plate model. The rigid body motion is prevented by applying appropriate boundary conditions (see Fig. 3.5(c) and Table 3.5). The geometric configuration and corresponding FE model are shown in Fig. 3.5 and the crack face FE mesh is shown in Fig. 3.3. Different Poisson's ratios of ν = 0.0, 0.3, and 0.49 were also used to investigate the effect of Poisson's ratio on the evaluated SIFs.

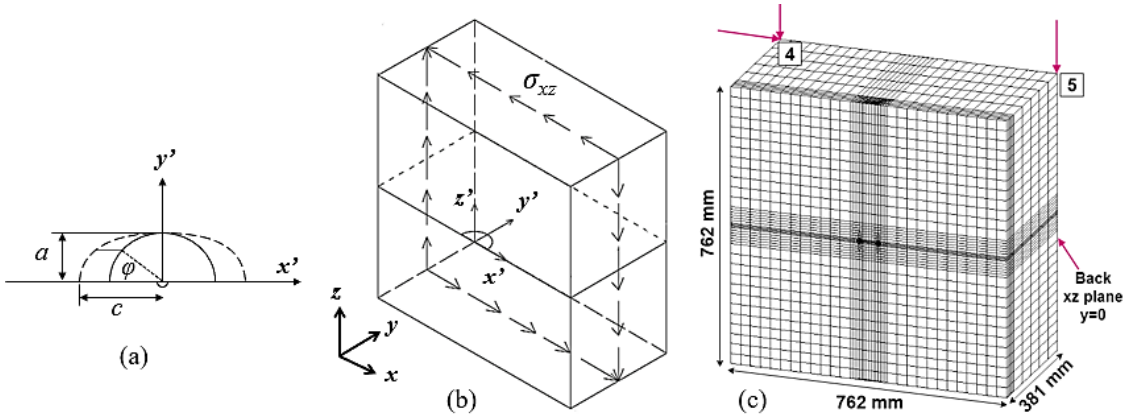

Fig. 3.5. A semi-circular surface crack in a semi-infinite flat plate body. (a) the geometry of the crack face, (b) geometry of the cracked body, and (c) FE model of the cracked body.

Table 3.5. Location and type of displacement constraints for pure shear loading.

Location of constraints	Nodal Coordinates (mm)	Type of Constraints
Node at point 4	(-381, 381, 381)	$u_x = 0$ $u_z = 0$
Node at point 5	(381, 381, 381)	$u_z = 0$
Back *x*-*z* plane of the model	$y = 381$	$u_y = 0$

3.4.2 Results and discussion

The evaluated MM-SIFs using NIFM are shown in Tables 3.6, 3.7, and Fig. 3.6. The calculated MM-SIFs are normalized as:

$$F_{II} = \frac{K_{II}^{Q}}{\sigma_{xz}\sqrt{\pi a}}, \text{ and} \tag{14}$$

$$F_{III} = \frac{K_{III}^{Q}}{\sigma_{xz}\sqrt{\pi a}}. \tag{15}$$

Where F_{II} and F_{III} denote normalized mode-II and -III SIFs while K_{II}^{Q} and K_{III}^{Q} are calculated mode-II and -III SIFs. Table 3.6 and Table 3.7 give the numerical values of MM-SIFs obtained employing NIFM and those given by Noda et al. [32] as well as the percentage difference between the solutions obtained by NIFM and Noda et al. [32]. The NIFM solutions are in good agreement with those given by the reference solution.

Figure 3.6 illustrates the effect of Poisson's ratio on the behavior of MM-SIFs. In the case of F_{II}, the SIF value increases by increasing the value of Poisson's ratio, especially near the crack mouth. On the other hand, F_{III} has the same behavior as in the case of F_I. It is noticed that by approaching $\varphi = 30°$, the difference in SIF values decreases by increasing the value of Poisson's ratio. On the other hand, by approaching the crack deepest point (i.e., $\varphi = 90°$), it is observed that the difference in SIF values increases by increasing the value of Poisson's ratio. The SIFs calculated for $\nu = 0.49$ are also in excellent agreement with the SIFs for $\nu = 0.5$ given by Noda et al. [32]. Based on the results shown in Table 3.6, Table 3.7, and Fig. 3.6, the developed ICDB

and NIFM-based SIFs calculation system are efficient in accurately estimating MM-SIFs for surface cracks in semi-infinite bodies.

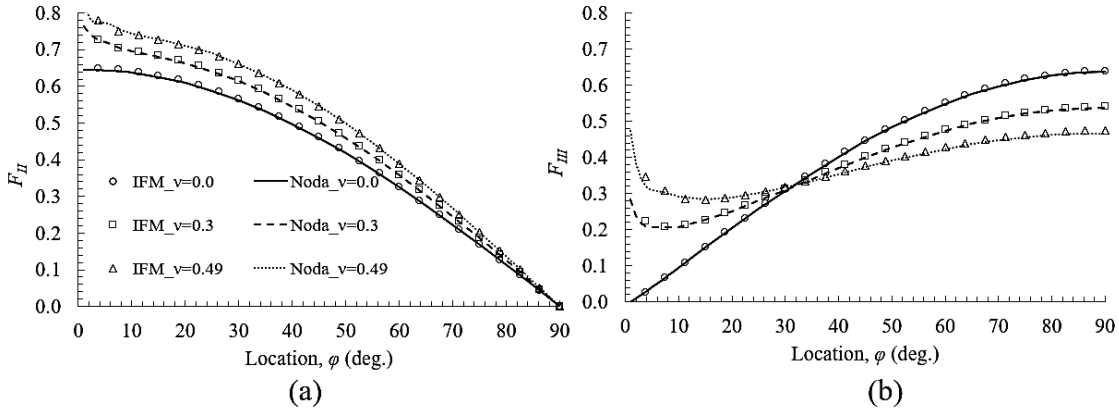

Fig. 3.6. Verification of the constructed ICDB with reference solutions. (a) F_{II} and (b) F_{III}.

3.5 Summary

In this Chapter, the NIFM-based MM-SIFs calculation system was developed and its adequacy was verified. Additionally, MM-SIFs for Poisson's ratios are evaluated to check the limit of application of the developed calculation system. The target FE models used in numerical examples are chosen to be large enough so that the finite width effect on the crack tip is negligible. The mode-I SIFs are calculated for a surface-cracked body under uni-axial tensile loading using the developed NIFM system.

In addition, mode-II and -III SIFs are also evaluated for the same cracked geometry subjected to pure shear loading. The MM-SIFs given by the NIFM-based SIF calculation system are compared with those obtained by the well-established analytical and numerical solutions. The percentage differences between the solutions are less than 2.0 in general. Therefore, the proposed NIFM-based SIF calculation system is reliable to calculate MM-SIFs under multi-axial loading. The proposed method is different from the previously reported studies in considering the CFT where six components of stresses on the crack face are taken into account in MM-SIF evaluation in the NIFM. It is also time-efficient compared to the IFM and improved in accuracy as CFT integral is integrated into the calculation system.

Table 3.6. Normalized SIF, F_{II}, for different Poisson's ratios.

φ (deg.)	v	F_{II}^{TFV}	$F_{II}^{external}$	F_{II}^{NIFM}	F_{II}^{Noda}	% difference of Noda vs. NIFM
30	0.0	0.5653	0.5619	0.5653	0.5623	0.53
	0.3	0.6167	0.6133	0.6167	0.6139	0.45
	0.49	0.6607	0.6601	0.6607	0.661	-0.05
60	0.0	0.3267	0.3246	0.3267	0.3249	0.56
	0.3	0.3596	0.3577	0.3596	0.358	0.45
	0.49	0.3884	0.3883	0.3884	0.3891	-0.17
90	0.0	0.0000	0.0000	0.0000	0	0.00
	0.3	0.0000	0.0000	0.0000	0	0.00
	0.49	0.0000	0.0000	0.0000	0	0.00

Table 3.7. Normalized SIF, F_{III}, for different Poisson's ratios.

φ (deg.)	v	F_{III}^{TFV}	F_{III}^{ext}	F_{III}^{NIFM}	F_{III}^{Noda}	% difference of Noda vs. NIFM
30	0.0	0.3098	0.3082	0.3098	0.3083	0.48
	0.3	0.3123	0.3107	0.3123	0.3108	0.49
	0.49	0.3190	0.3178	0.3191	0.3179	0.38
60	0.0	0.5518	0.5491	0.5518	0.5493	0.46
	0.3	0.4766	0.4738	0.4766	0.4739	0.56
	0.49	0.4284	0.4232	0.4285	0.4231	1.26
90	0.0	0.6404	0.6370	0.6404	0.6373	0.48
	0.3	0.5409	0.5377	0.5409	0.537	0.72
	0.49	0.4752	0.4682	0.4753	0.4662	1.91

CHAPTER 4

Calculation of mixed-mode SIFs for as-welded and HFMI-treated gusset welded joints

4.1 Introduction

For fabricating metallic structures, welding has been widely used due to its efficiency and handiness. However, there are some unavoidable problems with welding which endanger the integrity of the structures, such as high tensile RS, flaws, and other welding defects [28]. Post-weld treatments become the solution to prevent or, at least reduce the potential threats to the structure's strength after welding. One of the well-known methods is HFMI treatment in which the weld transition region is peened at a high frequency to induce compressive RS and to reduce the notch effect at the weld toe [6]. There are many recent works on HFMI, both numerically [7,11,22,23,26] and experimentally [9,24].

However, the effect of induced compressive RS after HFMI on the strength of structures has been barely discussed from the fracture mechanics point of view. It requires extensive study to understand the behavior of SIFs considering both welding and HFMI effects. In this chapter, a tee welded joint is employed for welding simulation using the in-house code JWRIAN [81]. Then, HFMI simulation is performed using explicit elastic-plastic dynamics simulation commercial code MSC Dytran. The RS of as-welded and HFMI-treated conditions are imported into the fracture mechanics analysis. Then, the MM-SIFs are evaluated for both as-welded and HFMI-treated conditions. This work shows the comparison of MM-SIFs after welding and HFMI-treated conditions and discusses the behavior of MM-SIFs under specified analysis conditions.

4.2 Analysis conditions

To study the effect of RS on MM-SIFs of as-welded and HFMI treated joints, numerical welding, cutting, and HFMI analyses are firstly carried out (refer to Appendix A.1 for more information on welding, cutting, and HFMI analyses). The MM-SIFs are then evaluated using the estimated RS. For MM-SIF evaluation, two different cracked models are employed: one represents the as-welded condition and the other one for the HFMI-treated conditions.

For the as-welded condition, the weld transition is assumed to be a sharp joint (without toe radius), ρ = 0.0 mm. The as-welded joint model has the same geometric configurations as the cutting model after welding simulation. In the case of the HFMI-treated welded joint, the weld toe profile has changed due to the effect of peening. Therefore, the profile at the weld transition also needs to be changed in the cracked model. For this reason, the deformed profile for the second cracked model was estimated using the shape function following the deformed shape after HFMI simulation.

Besides the RS, both models are subjected to remote tensile loading, σ = 100 MPa. In the case of the as-welded joint model, welding RS after cutting simulation (refer to Appendix A.2) is interpolated to the crack face and superimposed with the remote loading. The same procedure was applied for the HFMI-treated welded joint case in which RS induced in the HFMI simulation (refer to Appendix A.3-5) was used. The geometric configurations and the applied remote loadings are illustrated in Fig. 4.1.

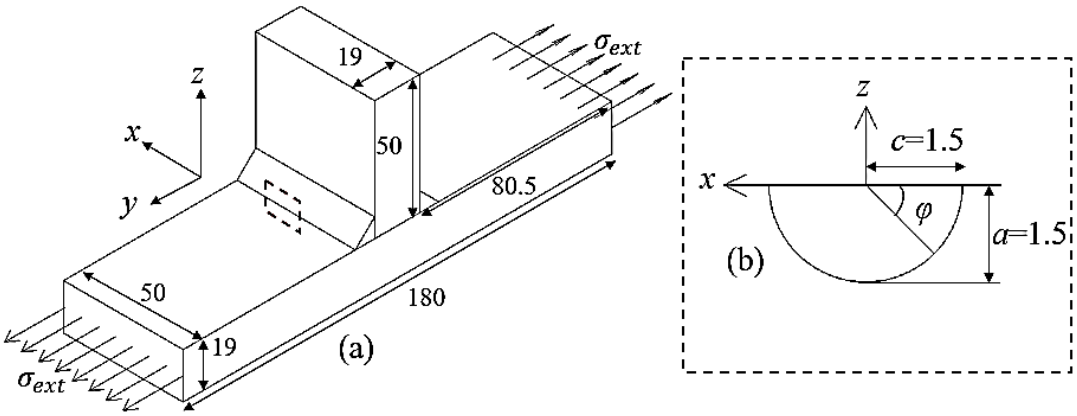

Fig. 4.1 Geometric configuration of the welded joint model used in fracture mechanics analysis. (a) Geometry of the cracked body, and (b) Geometry of the crack face. (All dimensions are in millimeters.)

A centered, semi-circular surface crack is located at the weld toe since the cracks are likely to appear at the weld toe due to local stress concentration and the effect of RS [27]. To compare the effect of RS induced by welding and HFMI on MM-SIFs, the cracks are placed at the weld toes in both FE models. The crack depth and half-length are chosen as a = 1.5 mm and c = 1.5 mm respectively. As mentioned in A.5, the compressive stresses were introduced up to the depth of 4.3 mm. Therefore, the chosen crack size is well within the range of affected RS in the HFMI-treated welded joint case.

The cracked FE models used in the fracture mechanics analyses are shown in Figs. 4.2 and 4.3. As the model is symmetric about the *y*-axis, only one-half models are employed for both analyses. The constraints are applied to prevent rigid body motions during the analysis. Young's modulus values and Poisson's ratio used in the analyses are E = 210 GPa and v = 0.3, respectively.

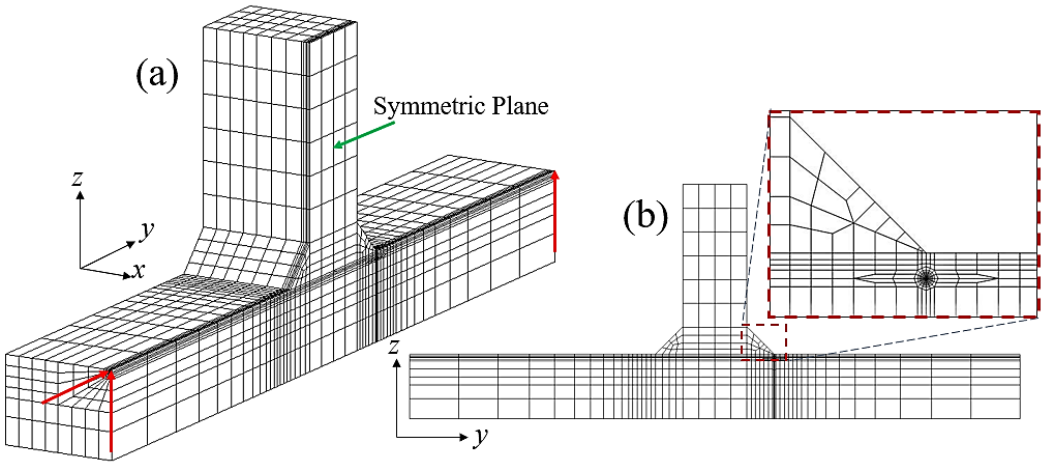

Fig. 4.2 FE model of the as-welded joint cracked model. (a) FE mesh and constraints of the whole model, and (b) FE model in the *y*-*z* plane and close-up view of the weld toe.

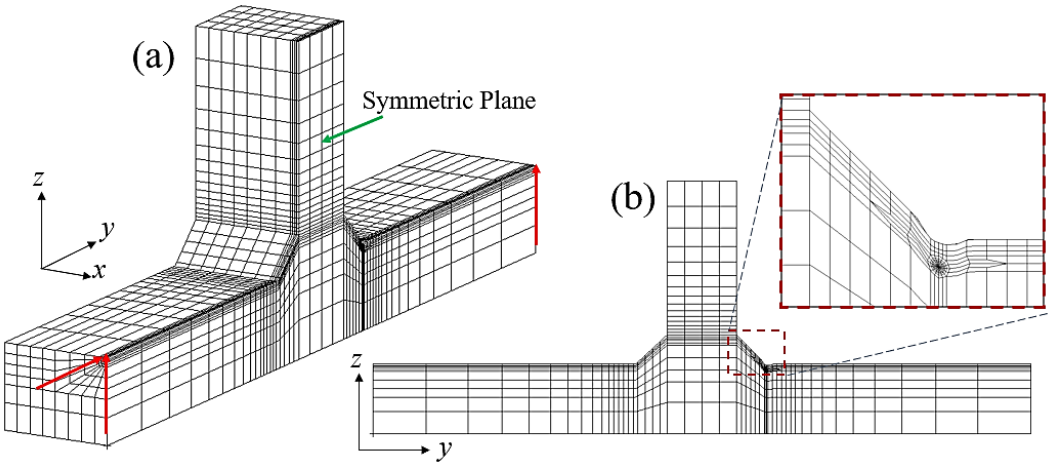

Fig. 4.3 FE model of the HFMI-treated joint cracked model. (a) FE mesh and constraints of the whole model, and (b) FE model in the *y*-*z* plane and close-up view of the weld toe.

4.3 Results and discussions

The MM-SIFs are evaluated for four different analysis conditions as shown in Table 4-1. The as-welded cracked model shown in Fig. 4.2 is employed for the analyses of

Cases 1 and 2. In Cases 3 and 4, HFMI-treated cracked model in Fig. 4.3 is used. The ICDBs for those models are firstly generated. In Case 1, only remote loading is applied to see the MM-SIF behavior without the effect of RS. The six components of RS after welding and HFMI simulations are interpolated to obtain the crack face loading. The interpolated traction stresses are superimposed to get the MM-SIFs for different analysis conditions. The calculated SIFs are normalized using Eq. (10) where $F_{I,II,III}$ represent normalized mode-I, -II, and -III SIFs, and Q_s denotes the flaw shape parameter.

$$F_{I,II,III} = \frac{K^{Q}_{I,II,III}}{\sigma_{yield}\sqrt{\frac{\pi a}{Q_s}}} \tag{16}$$

The comparisons of MM-SIFs for different analysis conditions are shown in Fig. 4.4 in which SIFs at the crack mouth are located at φ = 0°. and the deepest point SIF values are at φ = 90°. The reasonable behaviors of mode-I SIFs are observed for all the cases (see Fig. 4.4 (a)). Mode-I SIFs for Cases 1 and 2 are the largest at the crack mouth due to the stress concentration and high tensile RS at the weld toe. When HFMI-induced compressive RS is considered, the mode-I SIF solutions become fully negative.

As the applied remote loading is tensile load, only mode-I SIFs are dominant, and mode-II and -III SIFs should be negligible. However, unusual behavior of mode-II and -III SIFs are revealed in Cases 3 and 4. Positive mode-II SIFs appear up to 45° and SIFs then become negative as it approaches crack depth. In the case of mode-III SIF solutions, the spikes appear at the crack mouth and deepest point. The authors believed that this behavior is affected by the geometry of the welded joint and the RS distributions. However, further examinations shall be carried out on the reason behind this abrupt change of mode-III SIFs.

Table 4.1 Analysis conditions for evaluation of MM-SIFs.

Case	Model	Loading
Case 1	As-welded cracked model	Remote loading

Case 2	As-welded cracked model	Remote loading + welding RS
Case 3	HFMI-treated cracked model	Remote loading + RS induced after stress-free peening
Case 4	HFMI-treated cracked model	Remote loading + RS induced after peening with initial welding RS

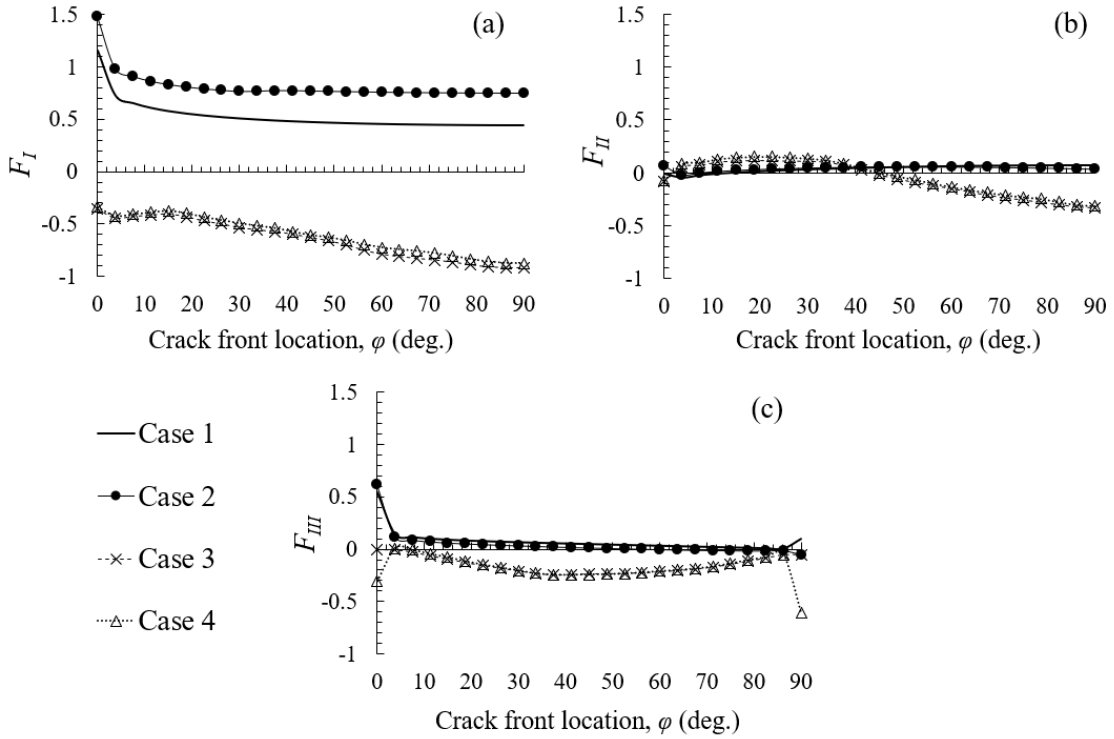

Fig. 4.4 Comparisons of the MM-SIF solutions for different analysis conditions. (a) F_I, (b) F_{II}, and (c) F_{III}.

4.4 Summary

In this chapter, the MM-SIFs of the T-joint are evaluated employing the developed NIFM-based-SIF calculation system, considering welding RS and HFMI-induced RS. The TEP simulation was carried out using in-house code, JWRIAN, and a cutting simulation was performed to proceed with further steps. The HFMI treatment was simulated in explicit code MSC Dytran for stress-free joint and joint with initial welding RS. The RS obtained by welding and peening simulations are superimposed with the applied remote loading and the MM-SIFs are calculated. Based on the obtained results, the followings are concluded.

1) Thermal and mechanical results obtained by welding analysis showed reasonable distributions. In future work, the RS of the T-joint specimen will be measured and compared with the numerical results.
2) The HFMI simulations provide the deformed welded profile following the IIW's recommendations. In addition, the maximum compressive RS induced by stress-free peening and those obtained from peeing with initial welding RS show only a few differences. In numerical HFMI simulations, welding RS can be omitted.
3) The comparisons of MM-SIFs reveal interesting behavior of SIFs when HFMI-induced RS is considered. Mode-I SIFs were greatly reduced when HFMI-induced RS are considered. Mode-II and -III SIFs show interesting trends and these solutions need further verification to clarify the reasons behind such behavior.
4) In future works, a fatigue test experiment will be conducted and fatigue crack propagation results will be validated with the numerical solutions based on this study.

CHAPTER 5

Evaluation of fatigue life for T-joints considering welding residual stress distributions

5.1 Introduction

FCP is the most threatening failure to welded joints due to high local stress concentration and the effect of welding RS. Therefore, fatigue life assessment of welded joints considering RS distribution is an important procedure in designing and maintaining welded structures. In this study, the fatigue life of welded structures is evaluated using the fracture mechanics approach. The welding RS is predicted by using the JWRIAN TEP-FEA code. SIFs of surface-cracked welded joints under CA loadings are evaluated using the NIFM. Although IFM has been widely employed for various research purposes using structures with different geometries [48,57,58,62,64], the application of NIFM to as-welded structures has not been investigated in the previous works. This section shows the applicability of the NIFM to the evaluation of SIF in as-welded structures by comparing the solutions of SIF obtained by NIFM against those given in previous studies.

In addition, the effect of welding RS on the behavior of SIFs is discussed. Fatigue life estimations are calculated for CA loadings with different stress ranges using the Paris-Elber law. Calculated fatigue life considering welding RS is compared with that ignored welding RS. This study demonstrates the applicability of the NIFM-based SIF calculation system to the fatigue life estimation considering welding RS. The proposed approach provides accurate solutions and an efficient calculation system for fatigue analysis under different loading conditions.

5.2 Analysis conditions

Two FE models were employed for different analyses. One FE model was used for TEP-FEA (TEP model) (Appendix B) while the other FE model was used for fracture analysis (cracked model).

To validate the application of NIFM and the developed ICDB for as-welded joints, surface-cracked T-joint models that have the same configuration as reported in Bowness's [72–74] were used. The cracked model consists of specially aligned FE

mesh on the crack face to accurately capture the stress singularity at the crack tip. To evaluate the fatigue life of the welded joint, SIFs were calculated for four different crack sizes. The crack sizes employed in the fracture analyses were adopted based on the FCP studies conducted by Kusuba [91] and Tanaka et al. [16]. Detailed information on the applied cracks is shown in Table 5.1.

Table 5.1 Details of the surface cracks employed in the analyses.

Crack No.	Crack size		Aspect ratio	
	a (mm)	*c* (mm)	*a/t*	*a/c*
1	1.1	2.1	0.14	0.52
2	2.4	2.85	0.30	0.84
3	3.7	5.4	0.46	0.69
4	4.7	6.35	0.59	0.74

For all crack sizes, four different cracked models with the same configurations were developed. The model configuration used in the fracture analyses is shown in Fig. 5.1(a), and Fig. 5.1(b) illustrates the configuration of the crack face. The flank angle, θ, is 45°. Due to symmetry about the *x*-axis, a one-half model only was used. The constraints were used to prevent rigid body motion (described with blue arrows in Fig. 5.2). The FE mesh and applied constraint conditions of the model (for Crack No. 4) are also shown in Fig. 5.2. Uniaxial remote tensile loading of σ_{ext} = 212.52 MPa in the *x*-direction was applied. Typical material properties for mild steel were used in the analysis: Young's modulus value, E = 210 GPa, and Poisson's ratio, v = 0.3.

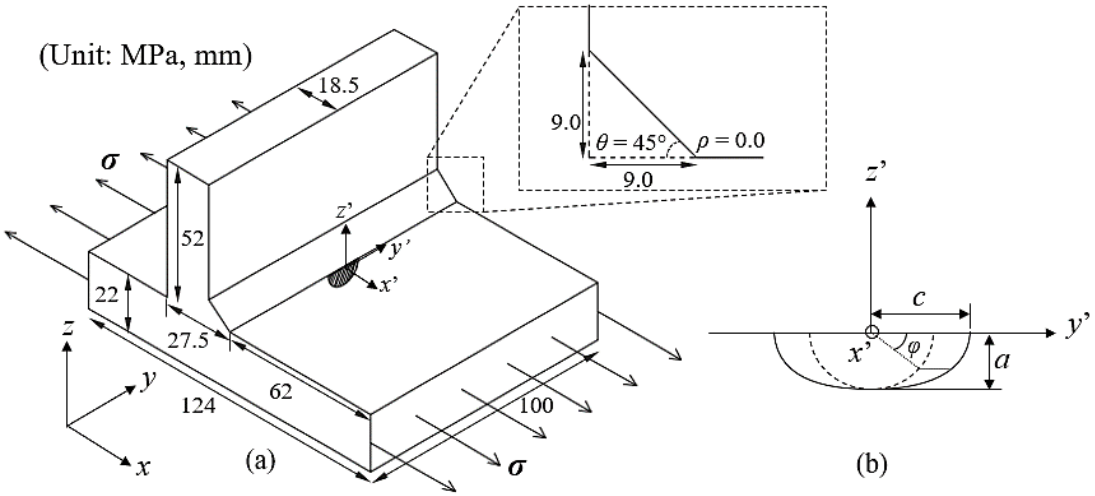

Fig. 5.1 Geometric configuration of cracked T-joint model. (a) Geometry of the cracked body and (b) Geometry of the crack face.

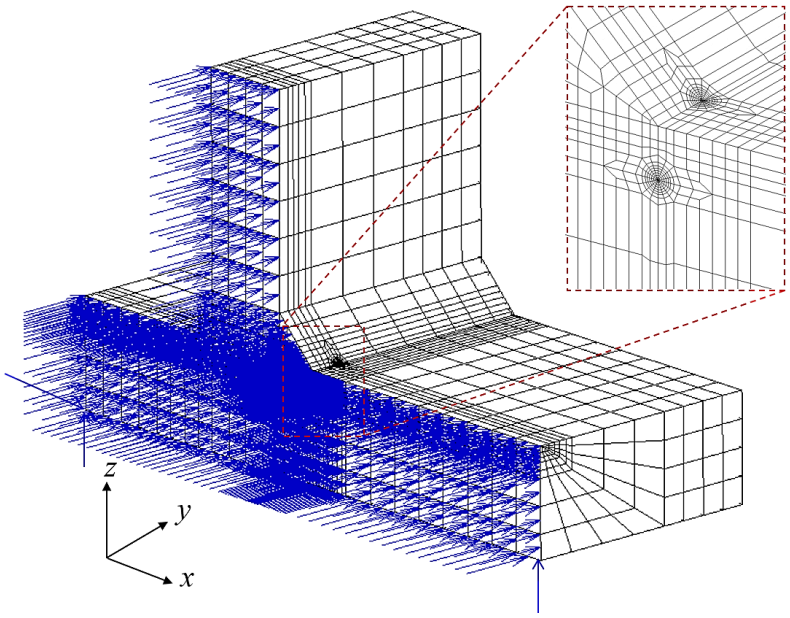

Fig. 5.2 FE model of the cracked T-joint, ρ = 0.0 and θ = 45°.

5.3 Calculation of SIFs

5.3.1 Calculation of SIFs under uniaxial tensile loading

SIFs of the cracked models mentioned in Section 5.2 were calculated by using the NIFM-based SIF calculation system. As the applied loading is uniaxial, only the results of mode-I SIFs are significant. To validate the developed ICDB and NIFM-based SIF calculation system for as-welded joints, the calculated SIF solutions obtained by NIFM were compared with those obtained by using analytical and numerical methods. The

SIF solutions described by “Bowness et al. (2002)” were obtained by employing the equations given in the report of Bowness et al. [72]. The values of SIFs calculated by the numerical method proposed by Gadallah et al. [71] are denoted as “Gadallah et al. (2017)” in the following discussion. The target solutions were also compared with the SIFs calculated from J-integral using the commercial software, MSC Marc (2014) [89]. The J-integral values given by MSC Marc were converted into SIF solutions using the K-J relation for linear-elastic material [39]:

$$J = \frac{K_I^2}{E^*}. \tag{17}$$

In Eq. (17), J represents the J-integral values, K_I is the calculated SIF solution, and E^* denotes the effective Young’s modulus values as mentioned in Section 2.1.2. The SIF values obtained from the conversion of J-integral are described as “Solution by MSC Marc” in the comparison. The SIF solutions were all normalized using Eq. (17) described in Section 4.3.

The comparisons of SIF solutions for Cracks No. 1, 2, 3, and 4 are shown in Fig. 5.3(a), (b), (c), and (d), respectively, in which the crack mouth is located at φ = 0° and the crack deepest point at φ = 90°. Except in the vicinity of crack mouth, the difference in SIF solutions with the reference solutions (Gadallah et al. (2017) and Solution by MSC Marc) are in excellent agreement. Although the SIFs at the crack mouth show a significant difference, those at the crack deepest point and along the crack front give good agreement with solutions of Gadallah et al. (2017) and Solution by MSC Marc for all cases, with a percentage difference of less than 1.0%.

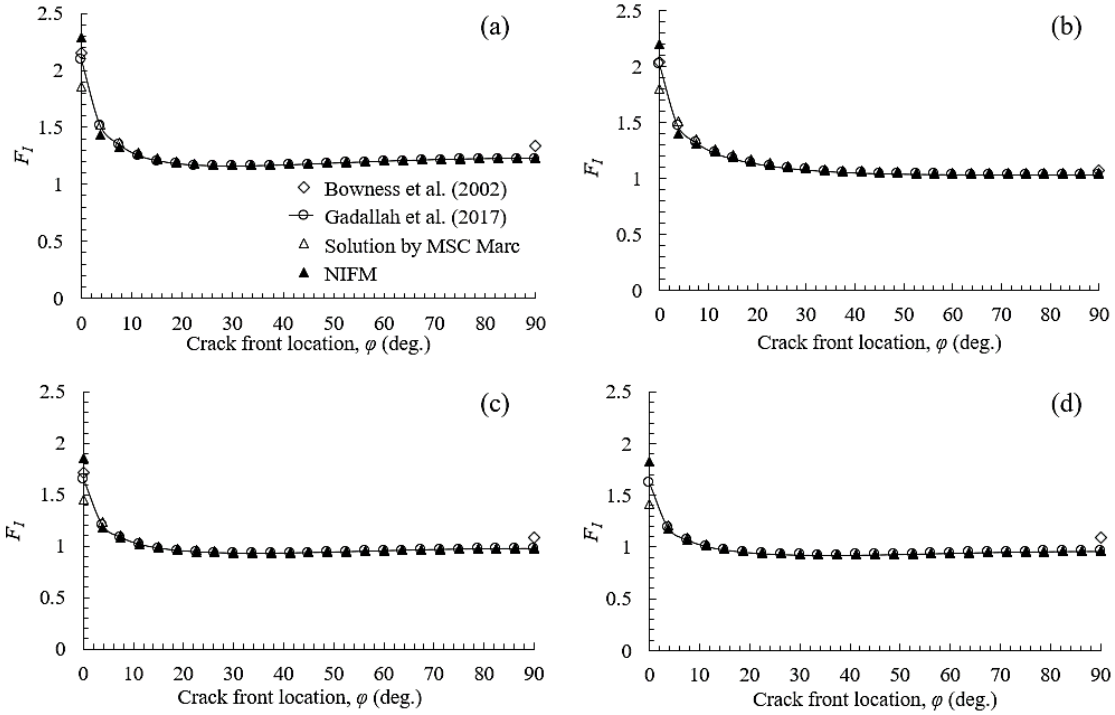

Fig. 5.3 Validation of SIF obtained by NIFM with different reference solutions. Cracks (a) No. 1, (b) No. 2, (c) No. 3 and (d) No. 4.

At the crack deepest points, the comparison with Bowness et al. (2002) shows up to about 10% difference for Cracks No. 1, 2, and 4 (see Fig. 5.3(a), (c) and (d)), and 3.141% in the case of Crack No. 2 (see Fig 5.3(b)). The reason behind this difference may be due to that Bowness's solutions were derived based on regression analysis where the solutions given by Bowness's equation [72] may show a substantial difference from those given by numerical analysis as the aspect ratios used in the current study are not included in their study [72]. The comparison of the SIF solutions demonstrated that the developed ICDB and NIFM calculation system are fully functional and reliable for the calculation of SIFs for surface-cracked T-joints.

5.3.2 Calculation of SIFs under CA loading considering welding RS

In this section, the SIFs under CA loading, which are to be used in the fatigue life estimation, were evaluated using NIFM. Two different CA loadings ($\Delta\sigma_1$ = 140.6 MPa and $\Delta\sigma_2$ = 196.9 MPa) were applied in the analyses to examine the effect of different stress range on SIFs and fatigue life. The stress ratios, $\sigma_{\min} / \sigma_{\max}$, of CA loadings are 0.0999 and 0.0735, respectively. By using NIFM, SIFs of surface-cracked T-joints with different crack sizes under CA loadings were calculated. There are two cases of SIF

solutions; one case was calculated using only the traction stresses generated by the CA remote loading without considering the influence of welding RS, which is denoted as "Without welding RS". For the other case, welding RS obtained in Appendix B was superimposed with the traction stresses generated by the applied CA remote loading. SIFs under the influence of welding RS were then calculated employing NIFM and are denoted as "With welding RS".

The results of K_{Imin} and K_{Imax} for different CA loadings are shown in Figs. 5.4-7. For all crack sizes, it is seen that the values of SIFs under $\Delta\sigma_2$ are larger than those under $\Delta\sigma_1$. In addition, the difference in SIFs with and without considering welding RS becomes smaller as the crack size increases. In the case of Crack No. 1 (see Fig. 5.4), the percentage difference of SIFs at the crack deepest point for K_{Imax} ($\Delta\sigma_2$) is 45.29 while that of Crack No. 4 is 15.96 (see Fig. 5.7). The same phenomenon is observed for other crack sizes under different loading conditions. It is also noticed that welding RS has a considerable influence on the behavior of SIF solutions where SIF solutions that consider welding RS are obviously higher than those ignore welding RS, especially at the crack mouth location of small cracks (47% increase in SIFs for Crack No. 1).

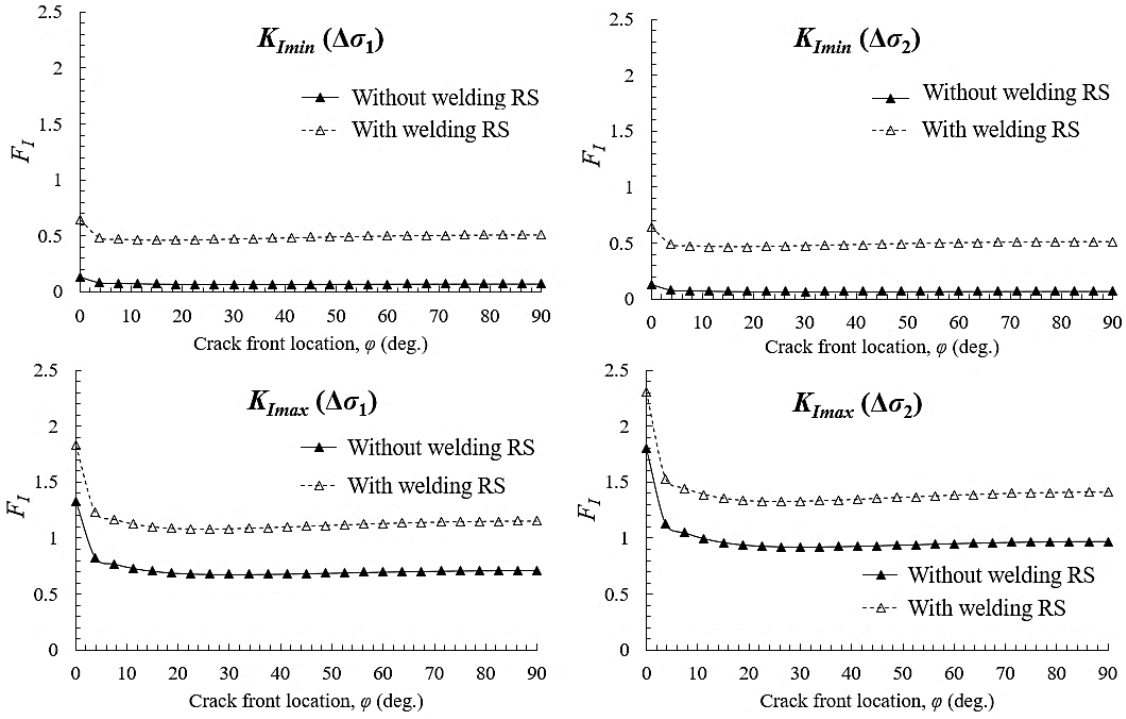

Fig. 5.4 Comparison of SIFs under different CA loadings with and without the influence of welding RS for Crack No. 1.

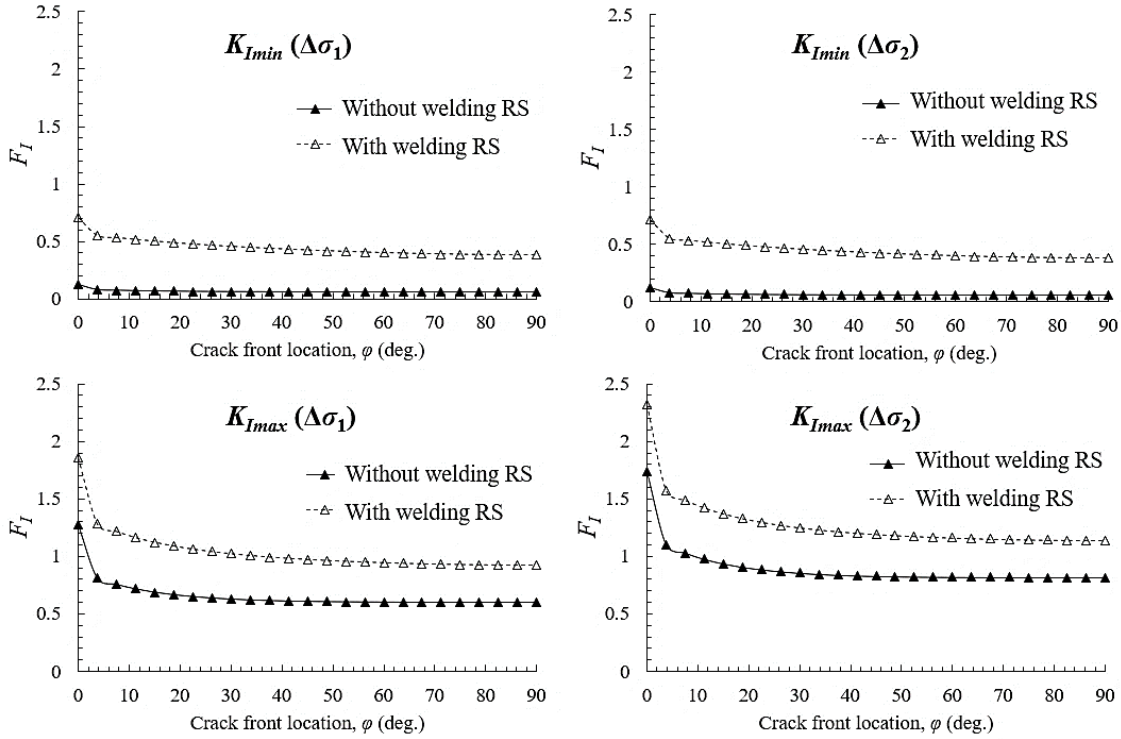

Fig. 5.5 Comparison of SIFs under different CA loadings with and without the influence of welding RS for Crack No. 2.

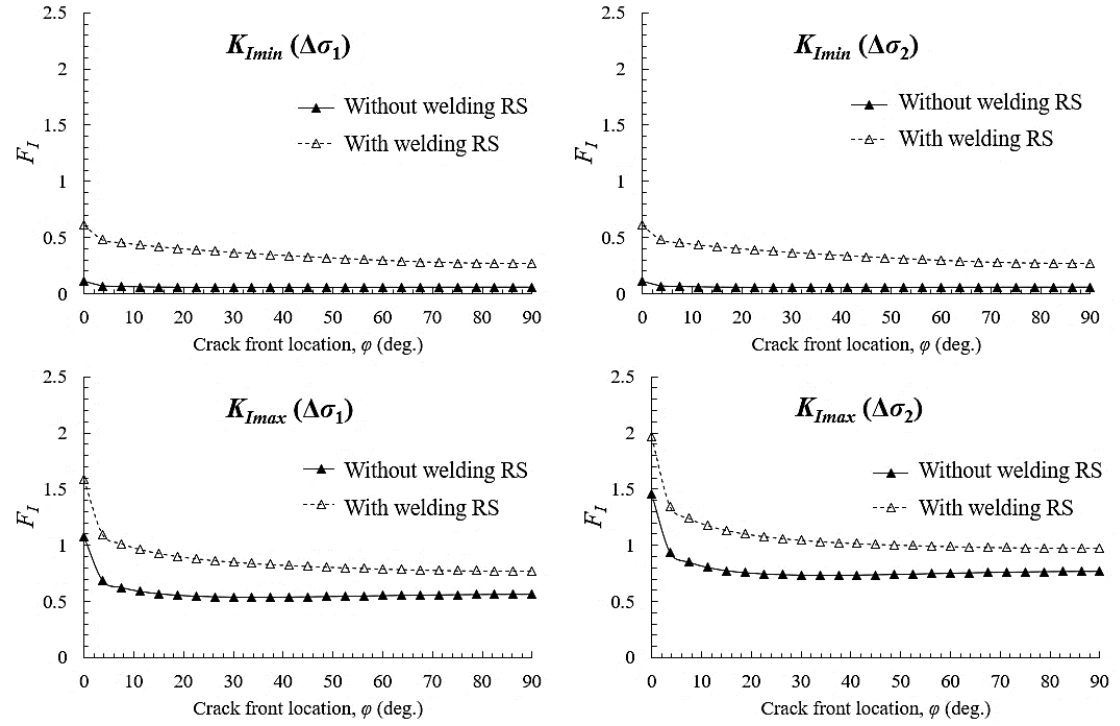

Fig. 5.6 Comparison of SIFs under different CA loadings with and without the influence of welding RS for Crack No. 3.

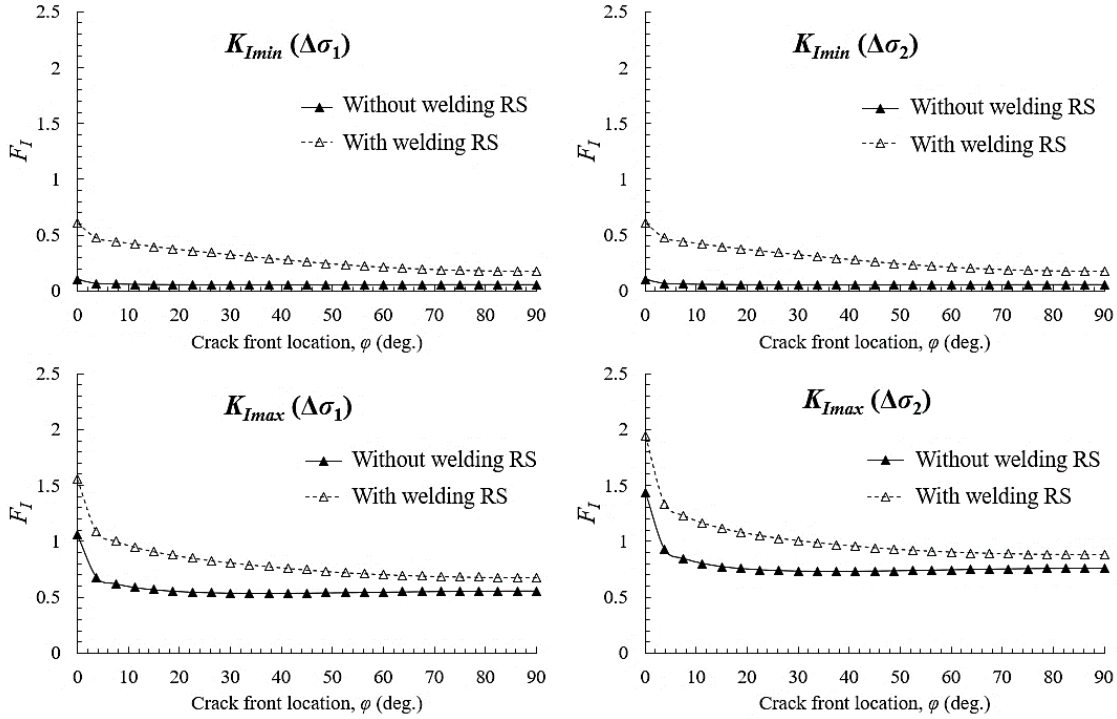

Fig. 5.7 Comparison of SIFs under different CA loadings with and without the influence of welding RS for Crack No. 4.

5.4 Calculation of fatigue life

Predicting the rate of crack growth under cyclic loading is an important assessment during the design and maintenance of structures. As well, considering the influence of welding RS in calculating the fatigue life for welded structures helps improve the accuracy of fatigue life estimation. Since welding RS represents an arbitrary stress distribution, it is challenging to include the welding RS distribution in the evaluation of fatigue crack propagation. However, many researchers have proposed methodologies and techniques to consider the effect of welding RS in fatigue life estimation [17,45,71].

One of the promising and convenient methods to include the influence of welding RS in FCP calculation is the IFM which was developed based on the weight function method. The NIFM proposed in this study enhanced the efficiency of a previously proposed IFM by changing it into a fully automated calculation system and considering the CFT-integral in the SIF evaluation. Using the proposed NIFM, the SIFs under arbitrary stress distribution are calculated accurately and efficiently. The advantage of the proposed NIFM which is efficient for handling the non-uniform stress distribution supports the calculation of SIFs under the influence of welding RS. Another benefit of

the NIFM is that the SIFs under different loading conditions and welding conditions can be repetitively calculated in a short time by giving the respective traction stress data. This makes comparative studies under different analysis conditions much easier and more efficient.

For fatigue crack propagation under cyclic loading, a well-established relationship proposed by Paris and Erdogan [40] has been widely used to estimate the fatigue life. However, to consider the crack closure phenomenon under cyclic tensile loading, Elber [70] suggested the crack growth relationship as in Eq. (18), in which the effective SIF range, ΔK_{eff}, was used instead of the SIF range, ΔK. The FCP constants C and m in Eq. (18) depend on the applied material and loading conditions, including environment and cyclic frequency.

$$\frac{da}{dN} = C\left(\Delta K_{eff}\right)^m \tag{18}$$

The effective SIF range is calculated as follows:

$$\Delta K_{eff} = U\Delta K, \tag{19}$$

where ΔK is calculated using Eq. (20): U is a stress range ratio and depends on stress range, crack length, material properties, and stress ratio R. However, in the work of Elber [70], U is calculated using Eq. (21) for steel material, and assumed to depend only on effective stress ratio R. While calculating R as in Eq. (22), the effect of welding RS are also considered by using the calculated SIFs instead of the applied stress values.

$$\Delta K = K_{Imax} - K_{Imin}, \tag{20}$$

$$U = 0.722 + 0.278R, \tag{21}$$

$$R = \frac{K_{Imin}}{K_{Imax}}. \tag{22}$$

The FCP material constants were chosen according to the recommendation in BS 7910 [28]. For assessing welded joints with steel in a marine environment, $C = 1.72 \times 10^{-13}$ N/cycle.mm$^{1/2}$ and $m = 3.42$ were adopted in the calculation. As described in

Section 5.3.2, two different CA loadings ($\Delta\sigma_1$ and $\Delta\sigma_2$) were employed for fatigue life estimation. SIFs for different crack aspect ratios were calculated using NIFM where SIF values with and without consideration of welding RS were utilized for the prediction of fatigue life. The calculated fatigue life based on the described conditions and parameters under $\Delta\sigma_1$ and $\Delta\sigma_2$ is shown in Fig. 5.8(a) and (b), respectively.

Based on the results shown in Fig. 5.8(a) and (b), the consideration of welding RS remarkably reduces the fatigue life of the welded joint. As the crack depth increases, the rate of reduction in fatigue life increases in both cases of CA loading. The reduction in fatigue life due to welding RS is 30% for $\Delta\sigma_1$ and 25% for $\Delta\sigma_2$. However, the number of cracks and crack sizes used in this study needs to be enhanced to fully understand the behavior of fatigue life of the T-joint until failure.

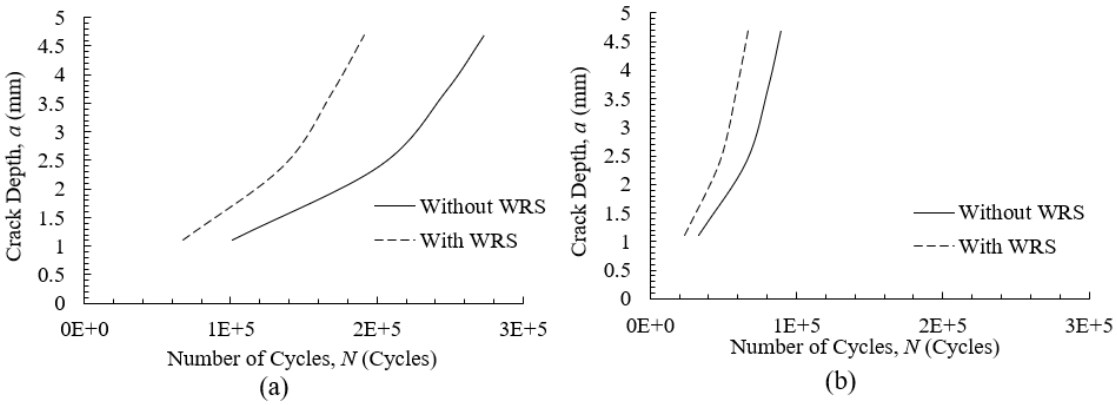

Fig. 5.8 Comparison of fatigue life under different CA loadings with and without welding RS. (a) $\Delta\sigma_1$ and (b) $\Delta\sigma_2$.

5.5 Summary

In this study, fatigue life for a surface-cracked T-joint was estimated by the fracture mechanics approach. The SIFs were calculated by using a fully automated NIFM. Two different CA loadings were employed to calculate the range of SIFs and fatigue life by using the Paris-Elber law. The welding RS was evaluated and included in the estimation of SIFs and fatigue life. Based on the results obtained, the following can be concluded:

1) The developed ICDB and NIFM-based SIF calculation system are fully functional for the evaluation of SIFs for surface-cracked T-joints under uniaxial loading.

2) The consideration of welding RS in the calculation of SIFs increases the resultant SIFs significantly, especially at the crack mouth.
3) The fatigue life of T-joints decreases by 30 % for $\Delta\sigma_1$ and 25 % for $\Delta\sigma_2$ when the welding RS was considered. It is important to examine different welding conditions for the optimum structure design, and fatigue life under each welding condition. The NIFM-based SIF calculation system proposed in this paper makes such studies easier in which welding specialists can evaluate the SIFs for various welding conditions without repeating the fracture analysis.

CHAPTER 6

Influence coefficient based fracture parameter modification factor in a cracked T-joint

6.1 Introduction

Despite the efficiency and accuracy of SIF solutions under arbitrary stress distributions, the NIFM still requires a highly qualified FE mesh of the cracked body which can be difficult for complicated welded joints. To reduce the computation step and obtain the utmost benefits, it is desirable to develop a database that gives the ratios ($\mu_k^{(IC)}$) of welded joint crack's ICs to those of a flat plate crack (IC's modification ratio database, IC-MRDB). $\mu_k^{(IC)}$ is not constant on the crack face by its nature, but, in Section 6.2, it is demonstrated that the calculated SIF has enough accuracy when $\mu_k^{(IC)}$ is approximated to be uniform across the crack face. In this simplified analysis, the representative single value ratio is called the weld modification factor (μ_k) for given SIF target nodes. The computation step for MM-SIFs analysis is saved drastically if μ_k for given crack geometry can be calculated by an engineering formula.

The μ_k can be used to calculate the SIF in a cracked T-joint under arbitrary stress distribution. By multiplying μ_k with the SIFs of a flat plate obtained by NIFM, MM-SIFs for a T-joint can be readily evaluated. In the numerical examples, T-joints with semi-circular surface cracks are employed. The MM-SIFs calculated by the μ_k method were verified against those given by directly computing MM-SIFs under membrane loading and welding RS conditions. An adequate agreement was achieved between the solutions given by the proposed μ_k method and the reference numerical analyses. Therefore, the MM-SIFs of surface-cracked T-joints under arbitrary stress distributions can be evaluated using the developed μ_k formulae.

In this study, an engineering formula that gives the approximate value of μ_k for a given crack and weld geometry is proposed. This formula considers multiaxial loadings and can be applied to T-joints with arbitrary stress distributions. The benefit of the μ_k

formula is demonstrated by comparing the MM-SIFs of T-joints considering welding RS obtained by the proposed method and those calculated using the NIFM. Section 6.2 explains the details of the methodology, analysis procedures to develop the μ_k formulae, its advantages, and application to evaluate the MM-SIFs of T-joints with arbitrary stress distributions. In Section 6.3, the numerical data required to derive the formulae are prepared. The developed μ_k formulae and validation are given in Section 6.4. And, Section 6.5 discusses the results of MM-SIFs in welded joints evaluated by the μ_k method considering welding RS. Finally, Section 6.6 summarizes the findings.

6.2 Methodology

6.2.1 Proposed method

The μ_k method is developed based on the NIFM as it is well-known for evaluating SIFs under arbitrary stress distribution. In the NIFM, the MM-SIFs of a surface crack are calculated by superimposing the ICs and CFT on the crack face, as [75]:

$$K_{I,II,III}^{Q} = \sum_{i,j} \sum_{P} C_{I,II,III}^{ij,QP} \sigma^{ij,P} , \tag{23}$$

where $K_{I,II,III}^{Q}$ denote the MM-SIF solutions along the crack front *Q-th* node (SIF target node, see Fig. 6.1(a)), $C_{I,II,III}^{ij,QP}$ are the ICs, and $\sigma^{ij,P}$ represents the CFT at the *P-th* node (UDL application node). The ICs are the calculated MM-SIFs at the SIF target nodes while each UDL application node is loaded with the unit load as demonstrated in Fig. 6.1(b). Following Eq. (23), SIFs of welded joints and flat plates can be calculated, as:

$$^{(w)}K_{I,II,III}^{Q} = \sum_{i,j} \sum_{P} {}^{(w)}C_{I,II,III}^{ij,QP} \, {}^{(w)}\sigma^{ij,P} , \tag{24}$$

$$^{(f)}K_{I,II,III}^{Q} = \sum_{i,j} \sum_{P} {}^{(f)}C_{I,II,III}^{ij,QP} \, {}^{(f)}\sigma^{ij,P} , \tag{25}$$

where the superscripts (*w*) and (*f*) indicate welded joint and flat plate, respectively. Differently, welded joint's SIF can also be calculated using IC-MRDB and flat plate's IC values, as:

$$ {}^{(w)}K^{Q}_{I,II,III} = \sum_{i,j}\sum_{P} \mu^{ij,QP}_{I,II,III}\ {}^{(f)}C^{ij,QP}_{I,II,III}\ {}^{(w)}\sigma^{ij,P}, \tag{26} $$

where,

$$ \mu^{ij,QP}_{I,II,III} = \mu^{(IC)}_{k} = \frac{{}^{(w)}C^{ij,QP}_{I,II,III}}{{}^{(f)}C^{ij,QP}_{I,II,III}}. \tag{27} $$

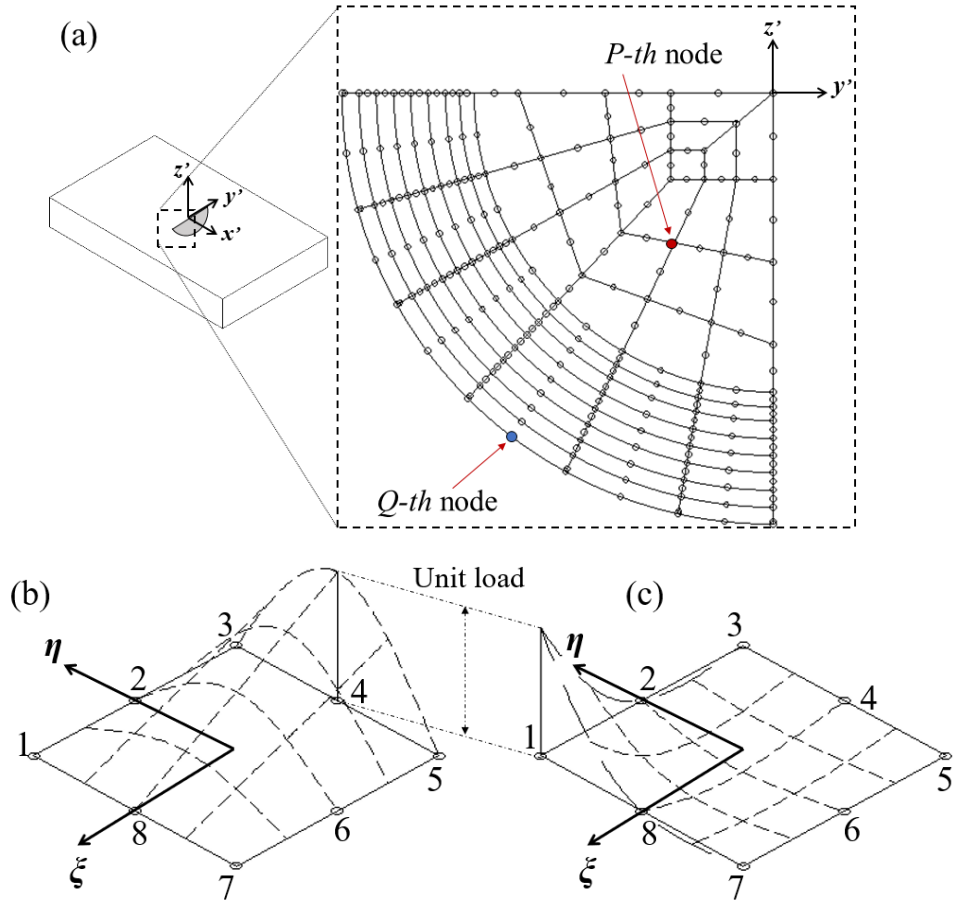

Fig. 6.1 Illustration of surface crack nodes and UDL used in the NIFM. (a) Notation of crack face node and crack front node on a surface crack, (b) UDL on an element face due to a unit load at the mid node, and (c) UDL on an element face due to a unit load at the edge node.

$\mu^{ij,QP}_{I,II,III}$ are the IC-MRDB's data record to be multiplied by the flat plate's ICs. However, developing IC-MRDB for various crack geometry is so laborious and time-consuming task due to the large numbers of data included in the ICDB. On the other hand, the IC becomes negligibly small when the distance between the SIF target and

the UDL application nodes is large enough [90]. As can be seen in Fig. 6.2, the normalized ICs near the SIF target node (crack mouth and deepest points) are around 1.0, while the ICs away from those points are negligibly small (minimum value is 0.0005). The IC distributions follow the same tendency for all SIF target nodes. From this, it can be deduced that the IC-MRDB's record $\mu_{I,II,III}^{ij,QP}$ can be approximated by a single value, $\mu_{k,I,II,III}^{Q}$, at the SIF target point, as:

$$^{(w)}K_{I,II,III}^{Q} \simeq \mu_{k,I,II,III}^{Q} \sum_{i,j} \sum_{P} {}^{(f)}C_{I,II,III}^{ij,QP} \, {}^{(w)}\sigma^{ij,P} , \tag{28}$$

$$\mu_{k,I,II,III}^{Q} = \frac{\sum_{i,j} \sum_{P} {}^{(w)}C_{I,II,III}^{ij,QP} \, {}^{(w)}\sigma^{ij,P}}{\sum_{i,j} \sum_{P} {}^{(f)}C_{I,II,III}^{ij,QP} \, {}^{(w)}\sigma^{ij,P}} . \tag{29}$$

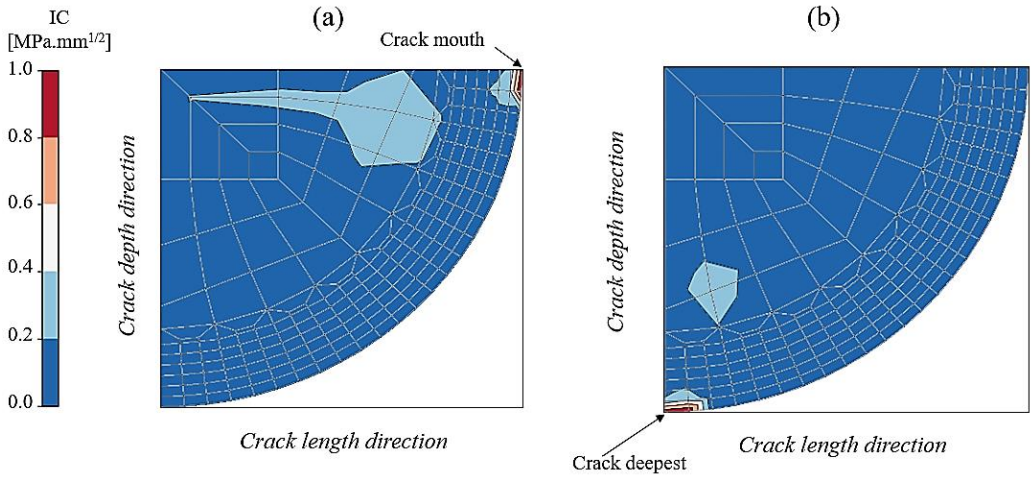

Fig. 6.2 Distribution of normalized ICs on the semi-circular crack face. (a) Crack mouth IC values, and (b) crack deepest IC values.

$\mu_{k,I,II,III}^{Q}$ is the modification factors for SIFs of the welded joint and flat plate where the CFT of the welded joints are employed in both SIF evaluations as in Eq. (29). It can be simplified by using a generic formula, as:

$$\mu_k = \frac{^{(w)}K}{^{(wf)}K} , \tag{30}$$

where, μ_k is the modification factor at the SIF evaluation point, $^{(w)}K$ and $^{(wf)}K$ are the calculated SIFs of welded joint and flat plates using the NIFM. The agreement

between $\mu_k^{(IC)}$ and μ_k also supports the inferred theory that employing the modification factor at the SIF evaluation points along the crack front is enough (see Appendix, Fig. C.1). Therefore, by using the proposed μ_k, the SIFs of welded joints under arbitrary stress distributions can be readily evaluated using the flat plate's ICDB. The developed formulae to calculate μ_k for semi-circular surface cracks are given in Section 6.4 and then validated for SIF evaluations under arbitrary stress distributions in Section 6.5.

6.2.2 Advantages and application of the proposed method

The proposed methodology is based on the NIFM which readily supports the MM-SIF calculation under arbitrary stress distribution (for example, stresses including notch effect and welding RS under different welding conditions). In the previous studies, the M_k are employed to evaluate the SIFs of a welded joint using the following equation [30]:

$$M_k = \frac{K_{weld}}{K_{flat}}, \tag{31}$$

where K_{weld} is the SIF of a welded joint and K_{flat} is the SIF of a flat plate under the same remote loading. The conventional approaches use the SIFs obtained under specific remote loadings and are only applicable for the cracks under the membrane, shear, or bending loading. However, to get a precise estimation of FCP, welding RS should be considered in the SIF evaluation process as it is an inevitable post-weld problem. The welding RS is usually arbitrary, and the RS components in the welding direction and normal to the welding direction are more significant than other RS components. In addition, due to the geometric configuration of the T-joint, not only the mode-I stress component but also mode-II and -III stress components are observed on the crack face at the weld toe. To accurately evaluate the FCP of a welded joint, MM-SIFs of T-joints which considers six components of tractions including welding RS should be investigated.

The proposed technique addresses the development of μ_k formula which can consider arbitrary stress distribution. Therefore, the main difference between the

conventional M_k and the proposed method is that the μ_k formula can be employed to get the MM-SIFs of the T-joint under arbitrary stress distribution while the conventional one is only for the specific loading. In addition, the M_k values are always larger than 1.0 due to the stress concentration at the weld toe of the welded joint than the flat plate. On the other hand, the μ_k values are lower than 1.0 as the CFT of the welded joint is applied in the SIF evaluation of flat plates. Hence, μ_k only gives the modification to the effect of geometry on the SIFs due to attachment while the M_k values magnify the SIFs of the flat plate to include the effect of stress concentration and geometry.

The application of the proposed μ_k formula is also different from those of the traditional approaches. The flat plate SIFs to be multiplied by the μ_k values are obtained by using the NIFM in which the stress distribution can be arbitrary including welding RS. To employ the proposed μ_k in the calculation of MM-SIFs under arbitrary stress distribution, the welding RS in the joint is firstly obtained by numerical TEP welding simulation. The RS is then imported as the CFT to a flat plate. When the ICDB for the target flat plate has been established, the ICDB and CFT are superimposed to get the flat plate SIFs, ${}^{(wf)}K$. The values are then multiplied by the μ_k to obtain the MM-SIFs of a welded joint. This application procedure is also illustrated in Fig. C.2.

6.2.3 Analysis procedure

1. To establish the μ_k formulae, the SIFs of T-joints and flat plates are firstly calculated using the NIFM in Section 6.3. Although applied loading is the uniform axial displacement at the end of the main plate, a non-zero bending moment arises due to the non-symmetric shape about the center of the model. Therefore, employing the NIFM, MM-SIFs of T-joints and flat plates under the same traction stresses are evaluated.
2. In Section 6.4.1, the evaluated MM-SIF values are then substituted into Eq. (30) to get the μ_k values at the SIF target points along the crack front. Using the calculated μ_k values, the regression models are developed to derive mixed-mode μ_k formulae. Section 6.4.3 presents the validation of the proposed method and μ_k formulae by

comparing the MM-SIFs obtained from the numerical analyses and those obtained by the proposed method.

3. Finally, the application of the proposed method is discussed in Section 6.5 in which MM-SIFs of T-joints with welding RS are calculated using the proposed method. The results are then validated with those obtained by numerical analyses.

6.3 Data preparation

The MM-SIF solutions of semi-circular surface cracks are calculated. Section 6.3.1 explains the theoretical background of NIFM. The geometric configuration of T-joints and flat plates, the FE mesh, and the detailed information on surface cracks are described in Section 6.3.2. In Section 6.3.3, the MM-SIFs obtained from the numerical analyses are presented, validated, and discussed.

6.3.1 The NIFM

The MM-SIF values are calculated using the NIFM-based SIF calculation system which is developed in CHAPTER 3. The UDL for each node on the crack face is employed to calculate the IC values, $C_{I,II,III}^{ij,QP}$, using the IIM. The second part of the NIFM equation, $\sigma_{ij,P}$, represents the CFT which are the traction stresses on the crack face.

6.3.2 Analysis conditions

6.3.2.1 T-joints

M_k solutions proposed by Bowness et al. [72] are recommended to calculate the SIFs of T-joints under the membrane and bending loading in BS 7910 [28]. To establish μ_k solutions for T-joints, the same geometric configurations of T-joints (Fig. 6.3(a)) as in Bowness et al. [72–74], are employed. The T-joint has a sharp weld toe with a semi-circular surface crack at the center of the joint. All cracks have the aspect ratio, a/c, of 1.0, where a is the crack depth and c denotes the half-crack length. The geometry of the crack face and the crack front locations, φ, are shown in Fig. 6.3(b). Uniform longitudinal displacements, U_x, which is equivalent to a tensile stress of 100 MPa are applied on one end of the main plate while the other is constrained in the x-direction.

FE models are generated for seven different surface cracks: a (= c) = 1.54, 2.0, 2.2, 4.4, 6.6, 11 and 15.4 mm. To prevent rigid body motion during analysis, boundary conditions are employed as shown in Fig. 6.4(a). As mentioned before, one end of the main plate is constrained in the x-direction to avoid rotation due to the attachment. The y-displacement constraints are applied on the x-z plane of the model as the model is symmetric about the x-axis. 20-noded hexahedral elements are employed. The crack front is surrounded by six domains, and the ratio of the biggest domain radius, R_D, to a is 0.25. Elements along the crack front have quarter-point nodes. The FE mesh on the crack face is shown in Fig. 6.4(b) and the ratio of the element's length at the crack front, L_e, to a is 0.033. The R_D/a and L_e/a ratios indicate the fineness of the mesh along the crack front, and the values are acceptable in the current study [92]. Young's modulus and Poisson's ratio employed in the analyses are 210 GPa and 0.3, respectively.

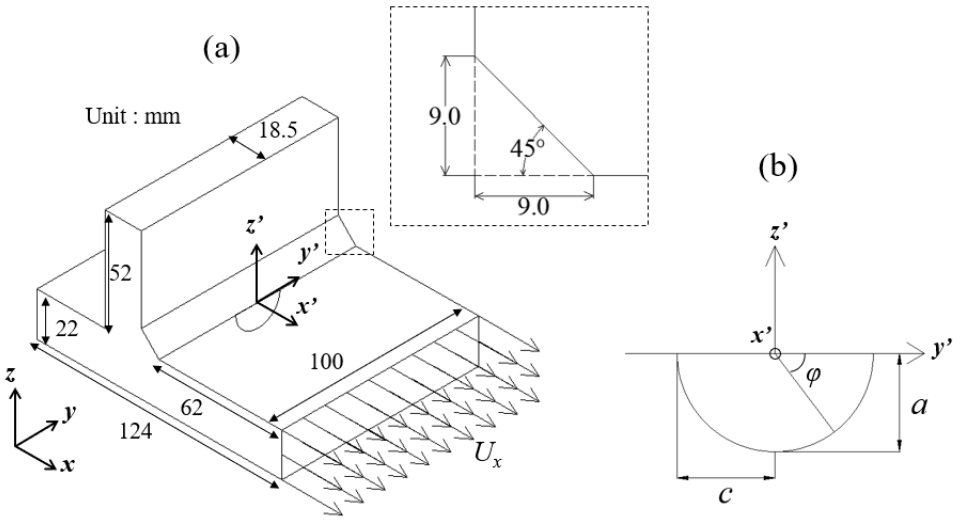

Fig. 6.3 Geometric configurations of a T-joint with a surface crack. (a) The geometric configuration of the cracked body, and (b) the geometric configuration of a surface crack.

6.3.2.2 Flat plates

To develop the M_k equations, flat plate SIFs are essential parameters. In Bowness's study, empirical SIF solutions proposed by Newman and Raju [31] were employed to obtain the SIF solutions using M_k. However, this study intends to develop μ_k for arbitrary stress distributions, flat plate SIFs are therefore evaluated as in Eq. (29).

Geometric configurations of the flat plate (see Fig. 6.5) are the same as the main plate of T-joints. However, the numerical analyses are performed using different loading conditions. For validation of the developed FE mesh and NIFM calculation system, remote tensile loadings, σ_{ext}, are applied on both ends of the flat plate (see Fig. 6.5(a)). While the T-joints are loaded with displacements only on one end, the uni-axial tensions on both ends are employed in the flat plate's fracture analysis as there is no need to consider the rotational movement due to attachment as in T-joints. On the other hand, to evaluate μ_k, the structural stresses of T-joints obtained by the superposition method are applied to the crack face of flat plates as illustrated in Fig. 6.5(b). For both loading conditions, the same boundary conditions that prevent rigid body motions are adopted. 20-noded hexahedral elements are also used for the flat plate models. The FE mesh of the cracked plate and cracked block are shown in Fig. 6.6(a) and (b). Crack blocks' mesh has the same L_e/a and R_D/a values as those used in the T-joints.

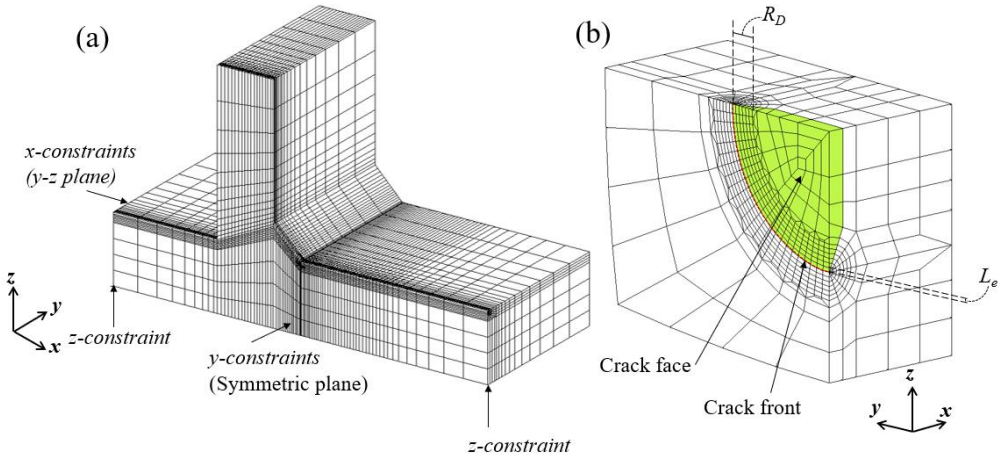

Fig. 6.4 FE model of a T-joint. (a) FE mesh and constraints of the cracked body and (b) FE mesh of the crack block.

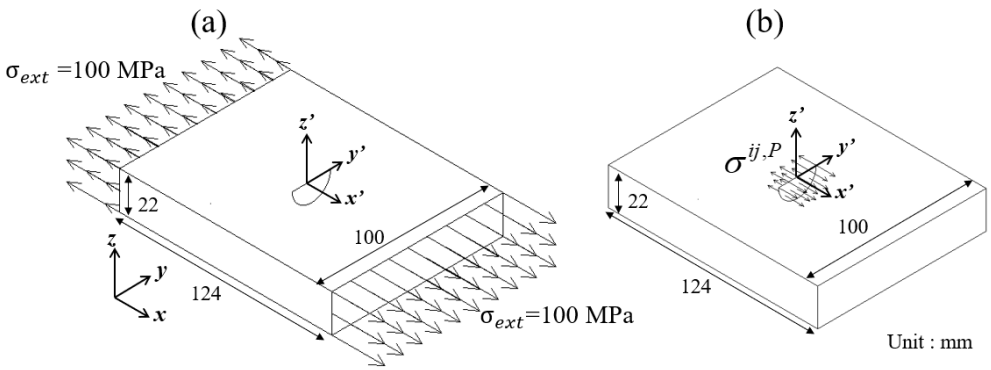

Fig. 6.5 Geometric configurations of a flat plate. (a) The flat plate under remote tensile loading, and (b) under CFT loading.

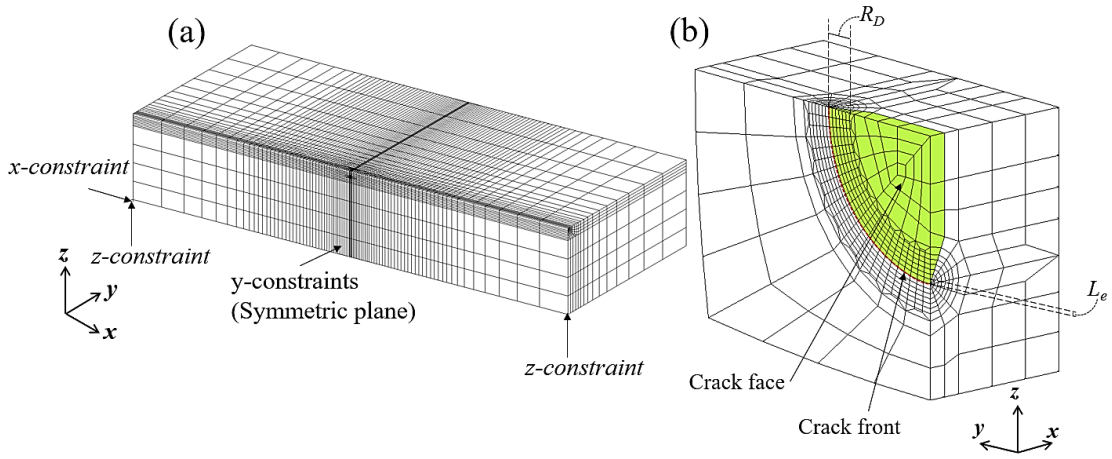

Fig. 6.6 FE model of the flat plate. (a) FE mesh and constraints of the cracked plate and (b) FE mesh of the crack block.

6.3.3 Numerical analysis and discussion

6.3.3.1 T-joints

MM-SIFs for T-joints under uniform displacement loadings are evaluated using the NIFM, J-integral available in the MSC Marc (2014), and analytical equations. The target SIF solutions obtained by NIFM are noted as "NIFM solution" in Fig. 6.7. MSC Marc supports the 3D J-integral method to calculate SIFs along the crack front [89]. It also provides a mode separation option for the models with isotropic materials. Therefore, MM-SIFs are directly obtained from the MSC Marc by conversion of J-integral to SIF values and described as "Solution by MSC Marc". In addition, Bowness's mode-I SIFs obtained by using M_k equations [72] are included as reference solutions and are represented as "Bowness et al., 2002 (Equation)" in Fig. 6.7. SIF solutions obtained by numerical analyses in Bowness's report are described as "Bowness et al., 2002 (FEA)". The calculated SIF solutions are normalized using the following equation:

$$F_{I,II,III} = \frac{K^{Q}_{I,II,III}}{\sigma_{ext}\sqrt{\frac{\pi a}{Q_s}}}. \tag{32}$$

$F_{I,II,III}$ and $K^{Q}_{I,II,III}$ are the normalized and calculated SIFs along the crack front. Normalized MM-SIF solutions of welded joint with Crack No. 1 obtained by NIFM are compared with the reference solutions in Fig. 6.7. For the other crack sizes (Cracks No. 2-7), the comparisons between the MM-SIFs obtained by NIFM and reference solutions are given in Appendix C (Figs. C.3-8). As the applied load is crack opening loading, mode-I SIF solutions are more dominant compared to mode-II and mode-III solutions (see Fig. 6.7(a)). The solutions given by MSC Marc are underestimated along the crack front while the NIFM solutions are relatively large due to the consideration of CFT-integral in the numerical integration. It was also noticed that the differences of F_I between NIFM and MSC Marc solutions become larger as the crack sizes increase where 0.425% was obtained for Crack No. 1 and 4.72% for Crack No. 7 at the crack deepest points.

At the crack mouth, the SIF solutions of Bowness and Lee [72] are considerably lower than those of NIFM. However, the larger the crack sizes, the lower the percentage differences at the crack mouth. As for the crack deepest point, the F_I solutions are in excellent agreement for all cracks with a percentage difference of about 1.0. Differences at the crack deepest point have the same behavior with MSC Marc solutions. The overall comparison shows a reasonable agreement and demonstrates the validity of the NIFM-based SIF calculation system and its solutions.

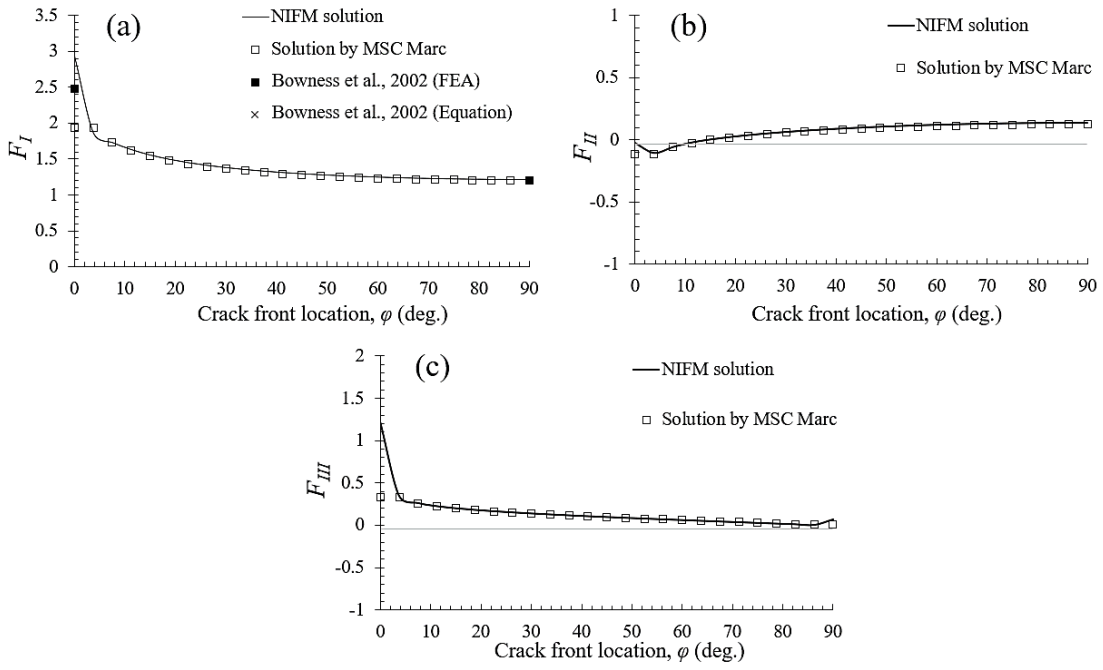

Fig. 6.7 Comparison of MM-SIF solutions for a welded joint under membrane loading (for Crack No. 1). (a) mode-I, (b) mode-II, and (c) mode-III SIFs.

In addition, the attachment on the left side of the surface crack makes asymmetric geometric configurations, leading to the occurrence of in-plane and out-of-plane shear stresses. Hence, mode-II and -III SIFs are also observed (see Fig. 6.7(b) and (c)). However, as the analytical solutions are not available for these SIF solutions, the validity is shown by comparing them with those obtained by J-integral in MSC Marc. The MM-SIF values given by MSC Marc are also slightly underestimated along the crack front, with an average of 5% lower than those given by NIFM.

Mode-II SIFs appear when the crack surfaces slide over one another, perpendicular to the leading edge of the crack [29]. F_{II} calculated by NIFM are in excellent agreement with those given by MSC Marc except at the crack mouth. However, F_{III} given by NIFM show unreasonable behavior at the crack mouth and deepest point locations. In the case of F_{III} at the crack deepest point ($\varphi = 90°$), F_{III} should be zero as the symmetric boundary condition is applied on the *x*-*z* plane. The values along the crack front are also obviously approaching zero near the crack deepest point. The reason for unstable crack ends' SIFs is due to the complicated stress fields and numerical analysis procedures defined in the IIM. On the other hand, it was noticed that crack mouth SIFs given by MSC Marc are the same as those at the adjacent crack front node for all modes of SIF solutions. Therefore, in the case of F_{III}, SIF solutions at the crack ends can be assumed to be equal to those at the adjacent crack front node. The rest of the SIF solutions along the crack front are well consistent.

6.3.3.2 Flat plates

SIF solutions for flat plates are evaluated for two different loading conditions. The first one, remote tensile loading, is to validate the FE mesh and the applied analysis condition. For this purpose, SIFs are compared with empirical solutions proposed by Newman and Raju [31] (described as "Newman et al., 1981") in Fig. 6.8, and those calculated by J-integral in MSC Marc. At the crack mouth, both reference solutions are about 4.3% larger than the SIFs given by NIFM. However, along the crack front including the deepest points, the differences are smaller than 1.0%.

After validating the mesh and analysis conditions for all flat plates, SIFs of flat plates loaded with CFT of T-joints are evaluated using NIFM. Those SIF solutions are noted as ${}^{(w)}K$, and will be used in the calculation of μ_k. As can be seen in Fig. 6.9, mode-II and -III SIFs also appeared since the employed tractions have six components of stresses including shear stresses. The same behavior of F_{III} at the crack mouth and deepest point as in Section 6.3.3.1 are observed due to the complex shear stress fields at these locations. F_I values along the crack front in Fig. 6.9 are relatively larger than those described in Fig. 6.8 as the axial stress component in welded joint's traction stress is larger than that in the flat plate.

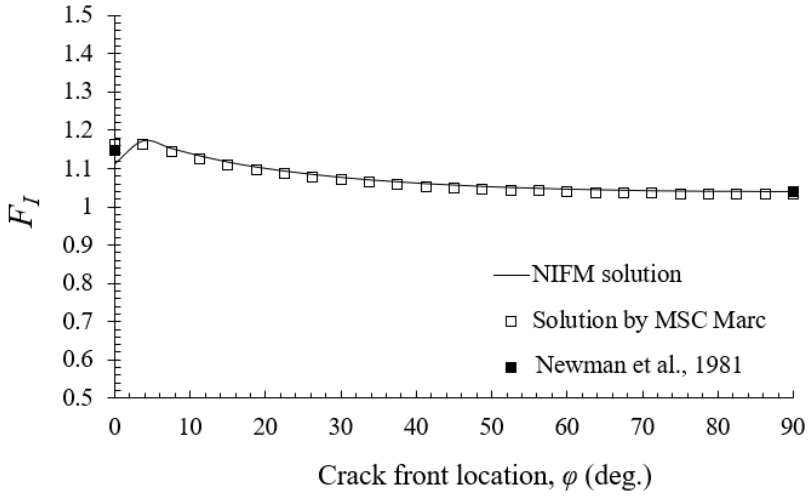

Fig. 6.8 Comparison of SIF solutions for the flat plate under membrane loading (for Crack No. 1).

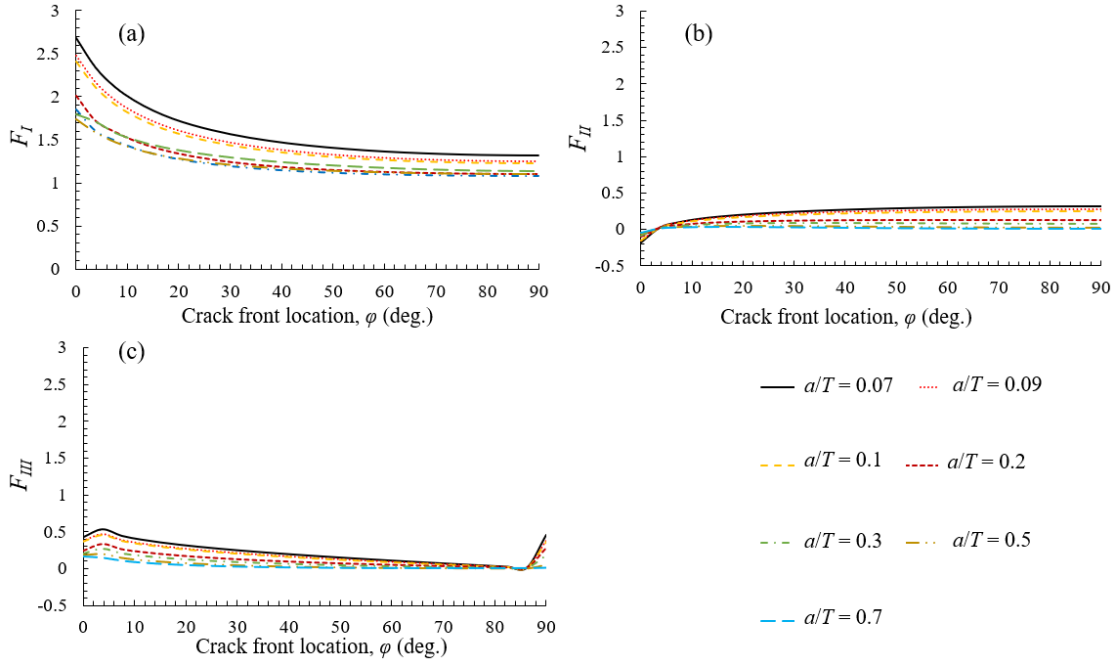

Fig. 6.9 MM-SIF solutions of a flat plate subjected to traction stresses of the welded joint. (a) mode-I, (b) mode-II, and (c) mode-III SIFs.

6.4 Development of μ_k formulae

As discussed in Section 6.3, mode-I SIFs are significantly larger than mode-II and -III SIFs along the crack front. In addition, due to the nature of the complicated stress fields at the crack end locations, SIF solutions given by the numerical methods at the crack ends are not reliable. Therefore, μ_k formulae for mode-I fracture are developed along the crack front. On the other hand, μ_k formulae for mode-II and III SIFs are estimated only for specific crack front locations.

6.4.1 Calculation of μ_k employing numerical solutions

μ_k is calculated by substituting ${}^{(w)}K$ and ${}^{(wf)}K$ in Eq. (30). The SIF solutions of welded joints in Section 6.3.3.1 are ${}^{(w)}K$ and those of flat plates using welded joint's traction stresses in Section 6.3.3.2 are ${}^{(wf)}K$. The calculated μ_k values from the numerical mode-I SIF solutions ($\mu_{k,I}$) are shown in Fig. 6.10. For all crack sizes, the values along the crack front except at the crack mouth (φ = 0°) show a quadratic trend. Under the same applied loading, mode-I SIFs for the welded joint at the crack mouth are usually larger than the flat plate SIFs due to the geometric effect and notch effect at

the weld toe, and so the M_k values are. Along the crack front, the μ_k values are smaller than 1.0. The reason is that the presence of the attachment creates local constraints to the crack opening in welded joints resulting in lower SIF values compared to the flat plate's solutions under the same traction stresses.

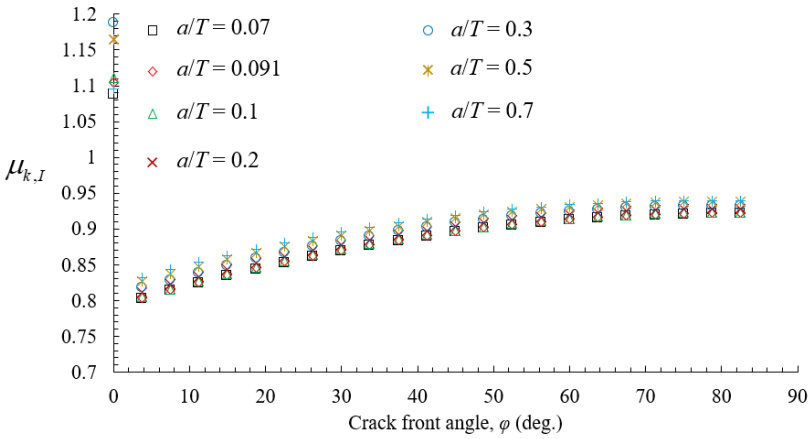

Fig. 6.10 Mode-I μ_k obtained from numerical SIF solutions.

The mode-II and -III μ_k ($\mu_{k,II}$ and $\mu_{k,III}$) values are shown in Fig. 6.11. As mentioned in Section 6.3.3.1, the crack end F_{III} given by the current analysis method are not reliable as well as those given by MSC Marc. Therefore, F_{II} and F_{III} at the adjacent crack front location are employed in the calculation of μ_k. Fig. 6.11(a) and (b) show $\mu_{k,II}$ and $\mu_{k,III}$, respectively at φ = 3.75°. At the crack deepest point location, only $\mu_{k,II}$ solutions are calculated (see Fig. 6.11(c)) as tearing fracture mode will not appear at the crack deepest point of surface crack in the flat plate and welded joint.

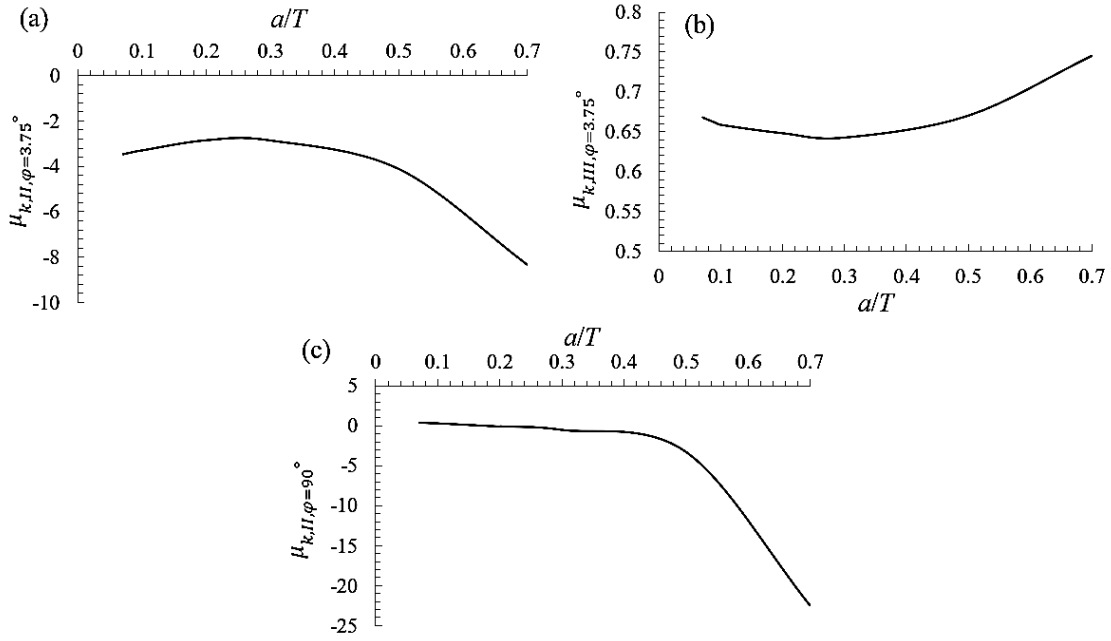

Fig. 6.11 $\mu_{k,II}$ and $\mu_{k,III}$ obtained from numerical SIF solutions. (a) $\mu_{k,II}$ at φ = 3.75°, (b) $\mu_{k,III}$ at φ = 3.75°, and (c) $\mu_{k,II}$ at φ = 90°.

6.4.2 Development of regression model and μ_k equations

Firstly, the equations for estimating $\mu_{k,I}$ solutions are developed using the regression method. As can be seen in Fig. 6.10, the $\mu_{k,I}$ values at the crack mouth are larger than the rest of the solutions along the crack front. In addition, the regression equation becomes complicated when the crack mouth and crack front values are considered together in one model. For these reasons, two different regression models are developed. For the values along the crack front (φ > 0°), the developed $\mu_{k,I}$ equation represents:

$$\mu_{k,I,\varphi>0^\circ} = f(\varphi, \frac{a}{T}). \tag{33}$$

As there are two variables in the equation, a multivariate regression model was chosen. As discussed in Section 6.4.1, the $\mu_{k,I}$ solutions show a quadratic trend along the crack front, hence, the quadratic regression model is also considered. Based on these conditions, the multivariate quadratic least squares regression model was constructed in this work. The regression model was developed based on the scipy.linalg.lstsq

function provided in Python programming language library [93] as shown in Fig. 6.12. Residue, the square of the 2-norm, is 4.707×10^{-3} in the developed regression model. The residue defines the accuracy of the regression model by showing the fitting deviations with the given data. Thus, the very low value of residue in the current regression indicates the excellent fitting of the regression plane.

The least squares equation and solutions given by the developed regression model are shown in the following equation;

$$\mu_{k,I,\varphi>0^\circ} = B_0 + B_1\varphi + B_2(\frac{a}{T}) + B_3\varphi(\frac{a}{T}) + B_4\varphi^2 + B_5(\frac{a}{T})^2 . \quad (34)$$

Where, the least squares solutions are: B_0 = 0.796877, B_1 = 3.085327 × 10^{-3}, B_2 = 0.081700, B_3 = -2.467194 × 10^{-4}, B_4 = -1.974010 × 10^{-5}, and B_5 = 0.044238.

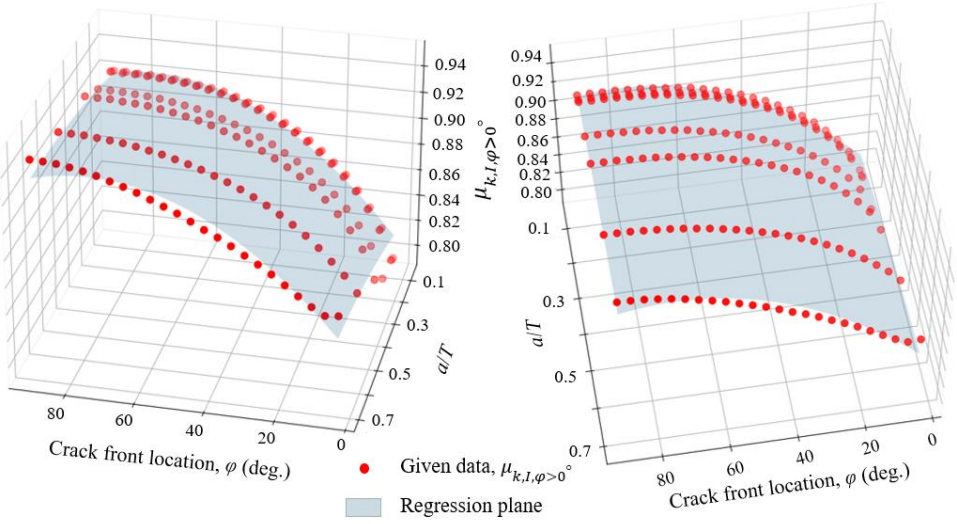

Fig. 6.12 Multivariate regression model for $\mu_{k,I}$ for $\varphi > 0.0°$.

Then, $\mu_{k,I}$ equation at the crack mouth ($\varphi = 0.0°$) is developed using the polynomial least squares regression method as follows (see Fig. 6.13):

$$\mu_{k,I,\varphi=0^\circ} = A_0 + A_1(\frac{a}{T}) + A_2(\frac{a}{T})^2 + A_3(\frac{a}{T})^3 . \quad (35)$$

Where, the coefficients are: A_0 = 1.0194, A_1 = 1.1292, A_2 = -2.2259, and A_3 = 1.0991.

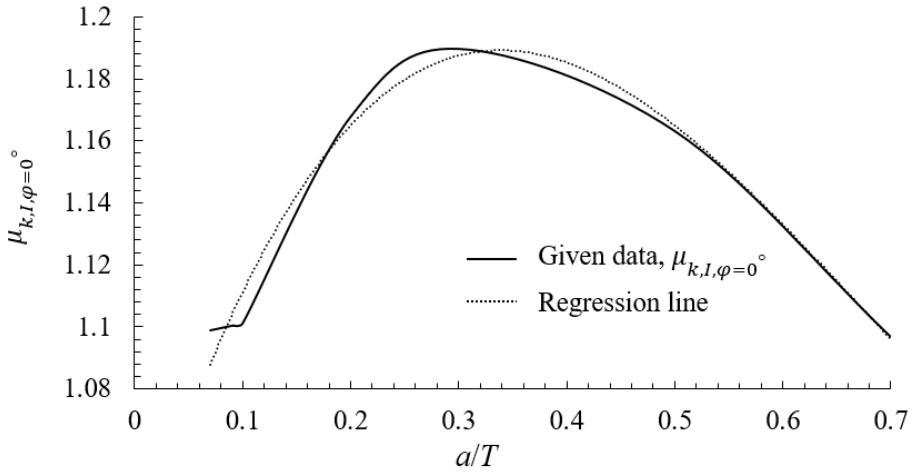

Fig. 6.13 Polynomial regression model of $\mu_{k,I}$ at $\varphi = 0.0°$.

A third-order polynomial regression equation is employed which gives the optimum R-squared value of 0.965. The R-squared values lie within the range of 0 to 1 in which high R-squared values show the capture of variance in given data well enough. It means that the current regression model has high accuracy for the estimation of $\mu_{k,I}$ at $\varphi = 0.0°$. For $\mu_{k,II}$ and $\mu_{k,III}$ equations, the solutions shown in Fig. 6.11 are employed to derive the regression equations. The same procedures are followed to get the μ_k equations in terms of a/T. The comparisons of regressed lines and original data are shown in Fig. 6.14. $\mu_{k,II}$ and $\mu_{k,III}$ equations at $\varphi = 3.75°$ (see Fig. 6.14(a) and (b)) have the same form as in Eq. (35).

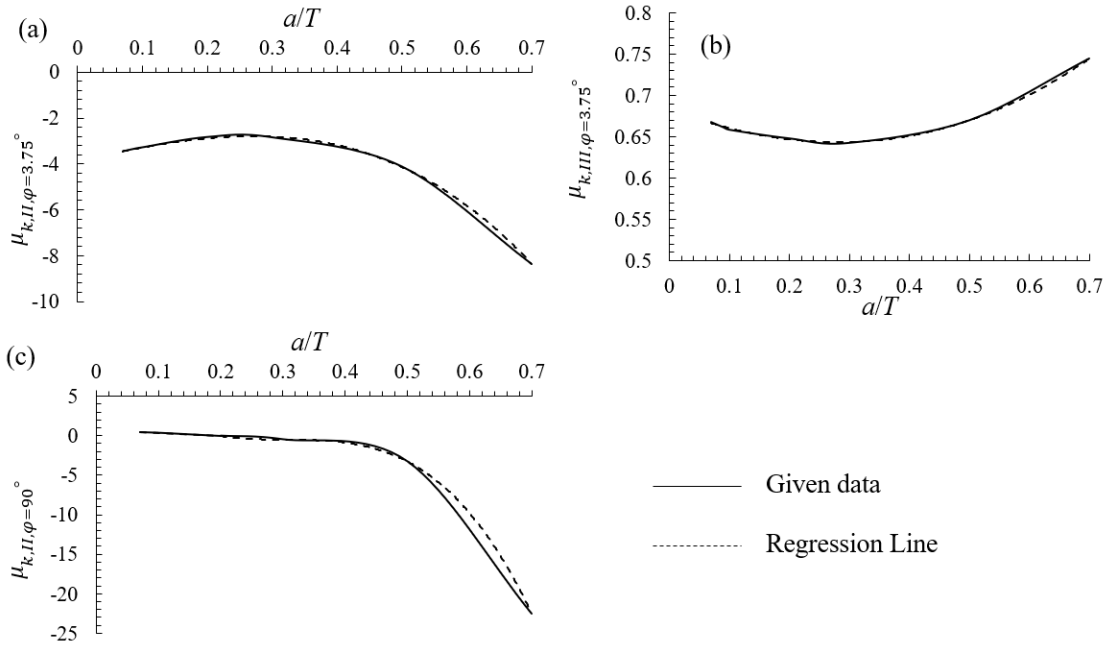

Fig. 6.14 Polynomial regression model for $\mu_{k,II}$ and $\mu_{k,III}$ μ_k. (a) $\mu_{k,II}$ at φ = 3.75°, (b) $\mu_{k,III}$ at φ = 3.75°, and (c) $\mu_{k,II}$ at φ = 90°.

The least-square solutions for $\mu_{k,II}$ equation at φ = 3.75° are: A_0 = -3.8713, A_1 = 6.3412, A_2 = -2.6044, and A_3 = -22.272. This regression model gave an R-squared value of 0.9998 so that the developed equation is reliable to estimate the $\mu_{k,II}$ values at φ = 3.75°. The coefficients of the regression line for $\mu_{k,III}$ at φ = 3.75° are listed as: A_0 = 0.6837, A_1 = -0.2782, A_2 = 0.4509, and A_3 = 0.1014. The R-squared value for this regression equation is 0.9988. Fig. 6.14(c) shows the regression line and the given numerical data of $\mu_{k,II}$ at φ = 90°. Due to the trend of the graph, this regression model is a combination of second-order polynomial and third-order polynomial equations. The R-squared value of the combined regression model is better than a single regression line. The combined regression model can be represented by the following equation:

$$\mu_{k,II,\varphi=90^\circ} = \begin{cases} \alpha_0 + \alpha_1(\frac{a}{T}) + \alpha_2(\frac{a}{T})^2, \frac{a}{T} \le 0.2 \\ A_0 + A_1(\frac{a}{T}) + A_2(\frac{a}{T})^2 + A_3(\frac{a}{T})^3, \frac{a}{T} > 0.2 \end{cases} . \quad (14)$$

Where, the values of α and A are: α_0 = 0.5354, α_1 = 0.8427, α_2 = -10.179, A_0 = 9.5085, A_1 = -97.519, A_2 = 318.85, and A_3 = -349.85. The differences between μ_k given by the proposed equations and numerical μ_k values are shown in Tables C.1-C.3. As can be seen in those Tables, the maximum percentage difference is 2.5987 and the minimum is 0.0037 for all μ_k values. Therefore, the proposed equations are reliable to evaluate the mixed-mode μ_k for semi-circular surface cracks in T-joints.

6.4.3 Validation of the proposed method and formulae

To validate the proposed method and formulae, MM-SIFs of T-joints under membrane loading are calculated using the μ_k method and compared with those obtained by the NIFM analysis. The flat plate SIFs are calculated by superimposing flat plate ICDB and traction stresses of the T-joint. Then, μ_k and the flat plate SIFs are multiplied to get the welded joint's SIFs. The solutions obtained by using the μ_k method are denoted as the "Proposed method". The solutions are validated by comparing them with those obtained by the NIFM, described as the "Numerical method". The analysis conditions for the calculation of MM-SIFs in Section 6.3.2 are followed.

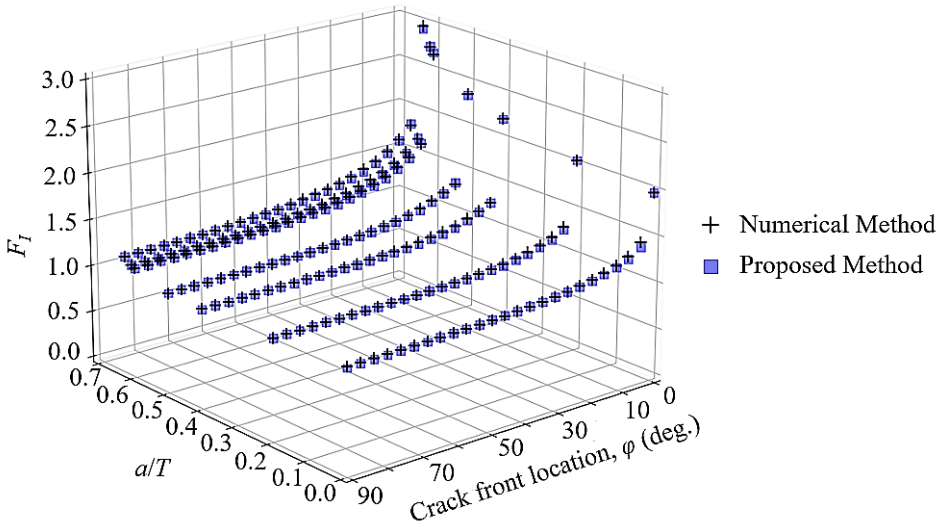

Fig. 6.15 Comparison of F_I solutions under membrane loading.

The comparison between F_I obtained by numerical and proposed methods (see Fig. 6.15) shows an excellent agreement with an absolute maximum percentage difference

of 3.177% and minimum percentage difference of 0.001%. The solutions and percentage differences are also tabularized in the appendix (Table C.4). Regarding the F_{II} and F_{III} solutions, the comparisons are shown in Fig. 6.16 and the data are given in Tables C.5 and C.6. Most of the F_{II} values obtained by the proposed method are underestimated than the numerical values, and this is due to the low fitting point in the regression model. However, the underestimated difference is only 1.712% and this value is adequate to estimate the F_{II} solutions under membrane loading. In the case of F_{III} solutions, the estimated values by the proposed method diverge from the numerical values in the range from -0.337% to 0.258%.

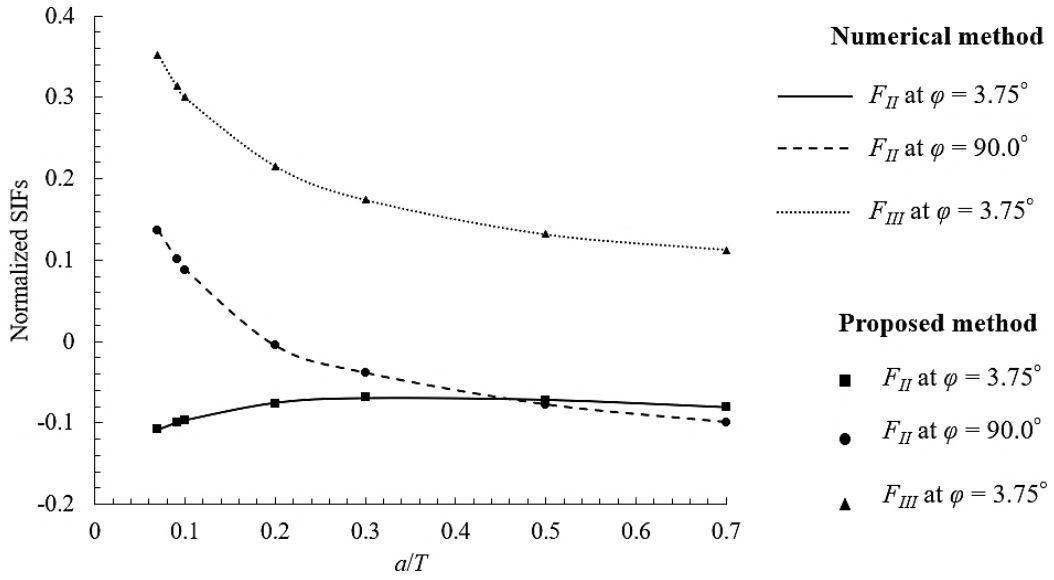

Fig. 6.16 Comparison of F_{II} and F_{III} solutions under membrane loading.

6.5 Application of the proposed methodology considering welding RS

The applicability of the proposed method to calculate MM-SIFs for welded joints with welding RS is demonstrated. The same procedures to get the MM-SIF values by the proposed method are employed as in Section 6.4.3. However, in this case, welding RS on the crack face is the important data input.

To simplify the calculation procedure, the welding analysis and its results are taken from a previous study in which Bowness's T-joint model was used to get the SIFs and fatigue life considering welding RS [94]. Further details of welding analysis and thermal results are described in the Appendix B. Longitudinal and transverse RS

obtained after thermal-mechanical analysis can be seen in Fig. 6.17(a) and (b), respectively.

The six components of welding RS obtained from the welding analysis are then combined with those of the traction stresses due to membrane loading. After the stress data has been prepared, the MM-SIFs are calculated by using an established flat plate's ICDB. The notations of results used in the comparisons are the same as those in Section 6.4.3. Mode-I SIFs are increased by about two times when welding RS is considered in the evaluation process. The calculated solutions by numerical approach and proposed method show consistency along the crack front (see Fig. 6.18). The deviations between these two solutions are listed in terms of percentage differences in Table C.7.

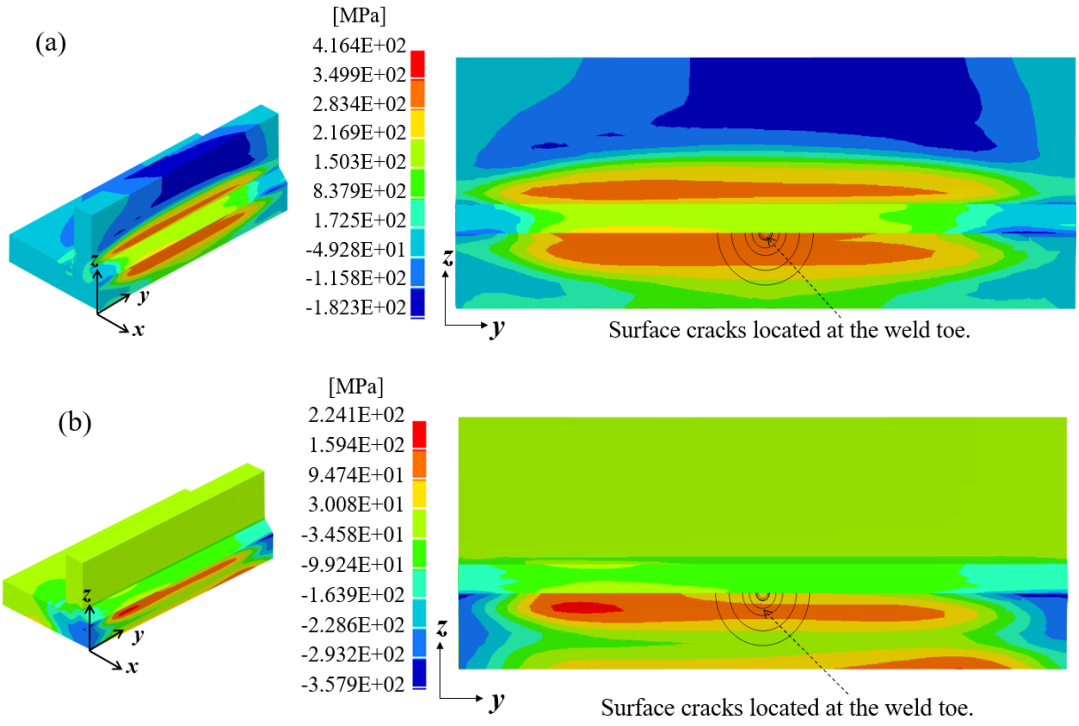

Fig. 6.17 Welding RS distributions of a T-joint. (a) Longitudinal stress component, σ_{yy}, and (b) transverse stress component, σ_{xx}.

In addition, F_{II} and F_{III} at specific crack front locations are also compared (see Fig. 6.19). The resultant values and their percentage differences between F_{II} and F_{III} are also shown in Tables C.8 and C.9. The percentages of deviations are larger in the case of F_{II} and F_{III} up to 6.644 % and -14.062% at some points than in F_I solutions. This is due to the change in shear stress distributions when the welding RS is considered. Shear stress components considerably increase in welding RS and the shape of stress distribution

affects the resultant F_{II} and F_{III}. On the other hand, the axial stress component is the largest in both loading conditions, membrane loading and welding RS distributions. When the stress distributions are combined, the effect of axial loading on F_I remains the same so that the differences between the solutions are smaller than in the case of F_{II} and F_{III}. In future works, the μ_k method will be employed for semi-elliptical cracks and welded joints with different geometries, and develop μ_k formulae for a wide range of applications.

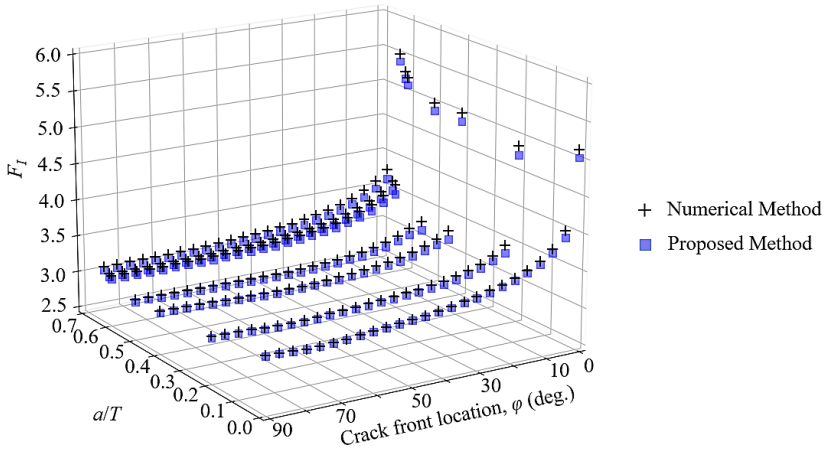

Fig. 6.18 Comparison of F_I under the membrane loading and welding RS.

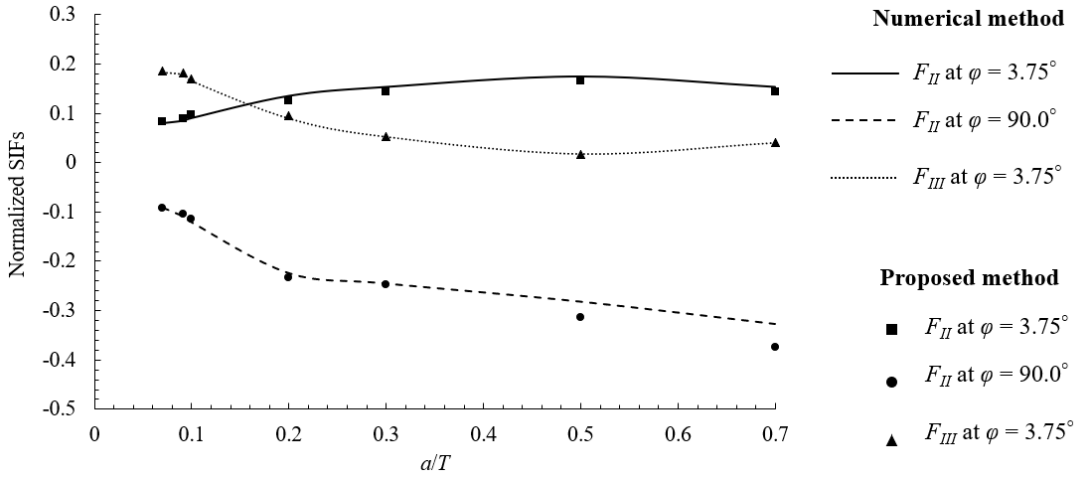

Fig. 6.19 Comparison of F_{II} and F_{III} under the membrane loading and welding RS.

6.6 Summary

A μ_k method for the calculation of SIFs under arbitrary stress distributions was introduced. The proposed method is employed to evaluate MM-SIFs of semi-circular surface cracks in T-joints. The difference between the conventional M_k method and the current μ_k method is the limitation of loading conditions, and methodology to calculate MM-SIFs of a flat plate. Although the M_k equations are limited for the specific loading conditions, the μ_k is applicable for any arbitrary stress distributions. An analytical or numerical method was used to get flat plate SIF solutions in the conventional method while the proposed technique is limited to employing the NIFM. In addition, the μ_k gives the modification factor to the effect of geometry on MM-SIF solutions where the M_k magnifies the flat plate SIF solutions taking into account the stress concentration.

The validity of the NIFM for evaluating MM-SIFs of welded joints and mode-I SIFs of flat plates were also proved by comparing them with well-established reference solutions. After that, μ_k equations were established using the regression method. To show the reliability and applicability of the presented technique and developed μ_k equations, the MM-SIF solutions are calculated by numerical and μ_k approaches and the results are compared. From the presented results, the following points can be concluded:

1) Due to the attachment, shear stresses appeared while the axial membrane loading is applied, thus, mode-II and -III SIFs are also observed. Yet, the values are negligible compared to mode-I SIFs. The evaluation of mode-I SIFs compared to analytical solutions shows reasonable agreement. Numerical MSC Marc solutions show great consistency with the MM-SIF solutions obtained by NIFM, except at the crack mouth. The unstable and complex stress fields at the crack end locations lead to such differences in MM-SIF solutions using different numerical methods. But, the adjacent crack front's solutions are in excellent agreement with those given by NIFM and MSC Marc.
2) In addition, flat plate SIFs obtained by NIFM are also compared with those given by the empirical equation. The deviations are only 4.58% at maximum and 0.19% at minimum.

3) The μ_k values estimated by the proposed equations and original values are only varying by 2.59% at most. The differences between solutions calculated by the proposed method and the NIFM method under membrane loading are less than 3.5% overall.
4) Applying the proposed μ_k equations and methodology, the MM-SIFs of T-joints with welding RS are also calculated. The results given by the proposed methods and those by the numerical analysis are in good agreement with acceptable deviations. Therefore, the proposed numerical μ_k method is efficient and accurate to determine MM-SIFs of T-joints under arbitrary stress distributions.

CHAPTER 7

Conclusions

The main objective of this study is to address the MM-SIF evaluation which is vital for crack propagation assessments under multi-axial loading. As the welded joints are inevitable parts of marine structures, fatigue cracks in welding RS fields were chosen as the target case study. According to the literature review, an accurate and efficient MM-SIF calculation system for surface cracks considering welding RS is still in need. This study fulfills the literature gap by proposing a NIFM-based-SIF-calculation system for evaluating MM-SIFs of welded joints under arbitrary stress distributions. In addition, a new approach for practical assessment of MM-SIFs is also developed by giving the μ_k formulae and introducing a procedure that can consider welding RS.

1. First of all, an effective technique to compute MM-SIFs under arbitrary stress fields was proposed and validated. The proposed numerical IFM technique was developed based on the IFM which is a discretized weight function method. As part of the NIFM, a fully-automated ICDB calculation system was developed. The IIM including the CFT integral, which can improve the accuracy of SIF solutions, was also modified and employed in the developed ICDB. Once the ICDB for UDL is established for a target FE model, MM-SIFs under arbitrary stress distributions can be calculated accurately in a short time. According to the validations of MM-SIF solutions obtained by NIFM with well-established reference solutions (analytical solutions and numerical solutions given by commercial software, MSC Marc), the developed NIFM-based-SIF-calculation system is fully functional and provides accurate MM-SIF solutions under arbitrary loading.

2. The proposed calculation system was then employed to evaluate MM-SIFs for as-welded and HFMI-treated welded joints. The comparison of MM-SIFs after welding and HFMI-treated conditions shows that: considering HFMI-induced compressive RS reduces the mode-I SIFs by 132-271%, mode-II and mode-III SIFs also appeared due to non-zero shear stresses by the HFMI-treatment. This comparison reveals that the mixed-mode fracture is possible

in the HFMI-treated joints caused by the in-plane and out-of-plane shears after HFMI treatment. Further investigations on the behaviors of MM-SIFs and crack propagation are needed by associating with experimental findings.

3. Thirdly, fatigue life for a surface-cracked T-joint was estimated by the developed NIFM-based-SIF-calculation system. Two different CA loadings were employed to calculate the range of SIFs and fatigue life by using the Paris-Elber law. The welding RS was evaluated and included in the evaluation of SIFs and fatigue life. The fatigue life of T-joints decreases by 30 % for $\Delta\sigma_1$ and 25 % for $\Delta\sigma_2$ when the WRS was considered. It is important to examine different welding conditions for the optimum structure design, and fatigue life under each welding condition. IFM-based SIF calculation system proposed in this paper makes such studies easier in which welding specialists can evaluate the SIFs for various welding conditions without repeating the fracture analysis. On the other hand, the crack growth prediction model (Paris-Elber's law) used in this study does not cover the mode-II and -III fracture. The development of mixed-mode crack propagation models is ongoing research, and the proposed MM-SIF calculation system can contribute to advancing the existing crack propagation model.

4. To facilitate the MM-SIF calculation of welded joints under arbitrary stress distribution, an IC-based modification factor μ_k method for a surface crack in a T-joint is proposed. By multiplying the proposed μ_k with the flat plate's SIFs obtained by NIFM, MM-SIFs for a T-joint subjected to arbitrary stress distributions on the crack face can be readily evaluated. The demonstration for application of the proposed μ_k method to the T-joints considering welding RS shows the accuracy and benefit of μ_k formulae and method. However, as the crack geometry is limited to semi-circular surface cracks, the application range should be extended for semi-elliptical cracks.

Appendix

A Thermal and mechanical analysis of T-joint

A.1 Welding and cutting analysis

The target specimen is a T-joint. The geometry of the target welded joint model is shown in Fig. A.1. A full 3D FE mesh model with linear hexahedron brick elements is applied for the welding simulation (see Fig.A.1 (a)). The total number of elements and nodes for welding mesh are 258,840 and 274,195, respectively. The elements with edge lengths of 0.7×0.7×2.5 mm are used in weld beads and heat-affected zone, and the larger elements are used for the rest of the mesh to balance computational efficiency and accuracy. The base plate and attachment are modeled with connected nodes at the intersections assuming full closure after the welding analysis.

Before mechanical analysis, thermal analysis is performed firstly to obtain the temperature history data. The temperature-dependent material properties for S355J2H are adopted, as reported in the literature [95]. A half ellipsoid moving heat source with uniform density [96] is used to calculate the welding temperature field. The arc efficiency of welding is assumed to be 0.9 in this study. The material properties of filler metal are assumed to be the same as that of base metal. The initial temperature of the specimen and the room temperature are set as 20 ^{o}C. The convection heat coefficient constant for the surface of the model is 20 W/m^2 K.

In the TEP analysis, the temperature history calculated by the thermal analysis is loaded on each node. The temperature-dependent mechanical properties of S355J2H [95] are taken into account. However, phase transformation and strain hardening are not considered in welding simulation. The constraints applied to prevent the rigid body motion, as shown in Fig. A.1. The welding sequence and welding conditions for each welding pass are described in Fig. A.1(b) and Table A.1.

To facilitate the fatigue test and numerical HFMI simulation, the target welded joint is cut into small specimens. To estimate the RS of the cut specimen, a cutting simulation is performed. The unwanted elements for welding mesh are deactivated, and as-welded RS is imported into the reserved mesh as the initial stress for cutting analysis, as shown in Fig. A.2. The boundary condition and material properties for cutting analysis are the same as that of welding analysis.

Table A.1 Welding conditions.

Pass	Joint Type	Heat input (kJ/mm)	Travel speed (mm/s)	Inter pass temperature (°C)
1	Fillet seam	2	8	60
2	Fillet seam	2	8	20

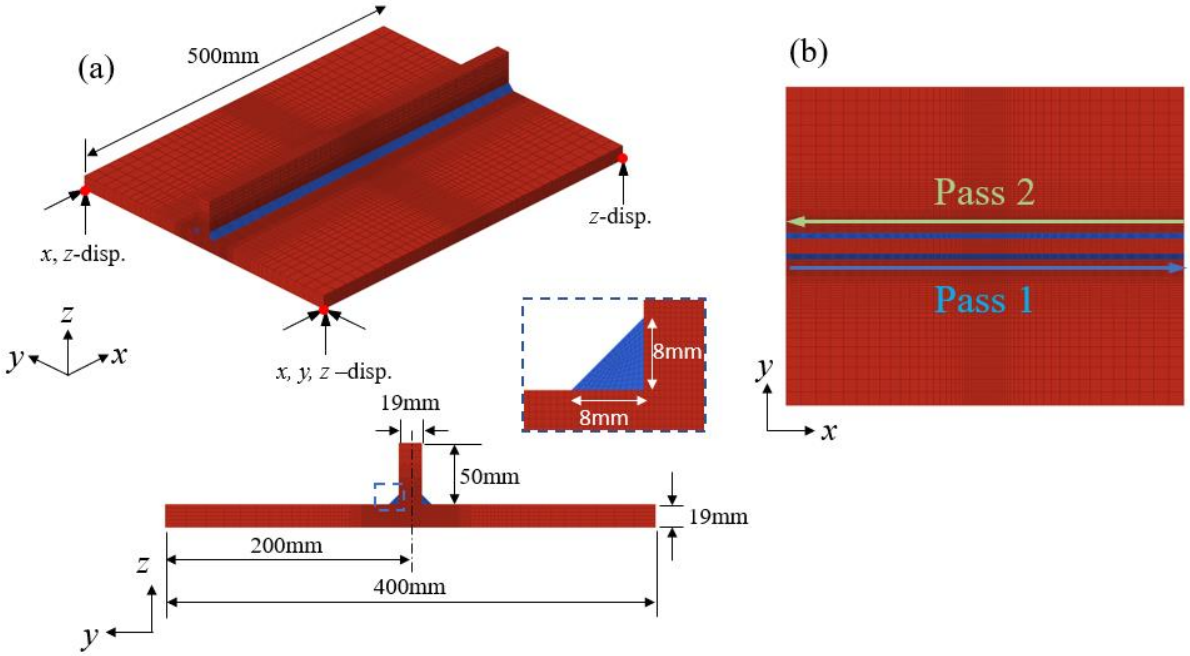

Fig. A.1 FE model for the welding simulation. (a) Constraints and weld profile of the FE model, and (b) Welding sequence used in the analysis.

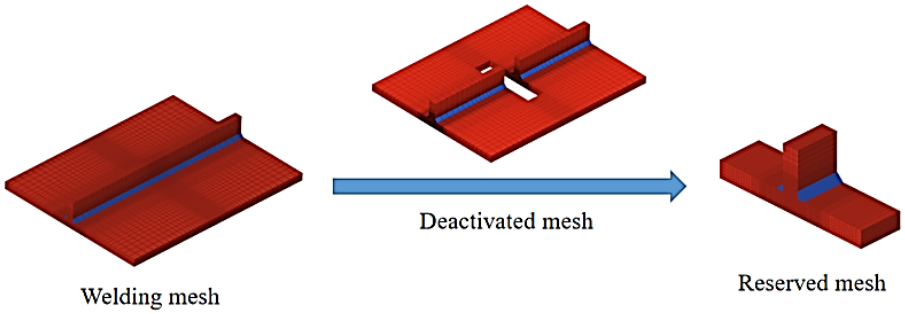

Fig. A.2 Illustration of cutting simulation.

A.2 Results and discussion for welding and cutting analyses

Fig. A.3 shows the simulated maximum attained temperature distribution on the center cross-section. The red zone, with a temperature greater than 1450 °C, represents the fusion

zone of the weld. A reasonable temperature field can be achieved by adjusting heat source parameters.

Considering the longitudinal stress on the center cross-section (see Fig. A.4(a)), high-tensile stress appears within the heat-affected zone because of relatively large constraint in the longitudinal direction, while the distribution of transversal stress (Fig. A.4(b)) is more complex and exhibits a self-balancing characteristic along the thickness direction.

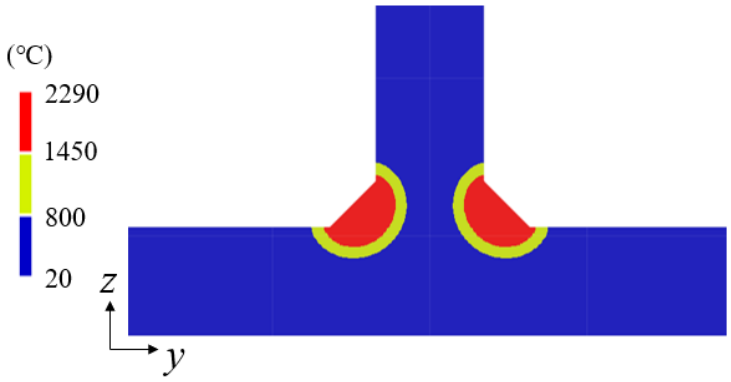

Fig. A.3 Distribution of peak temperature on the center cross-section.

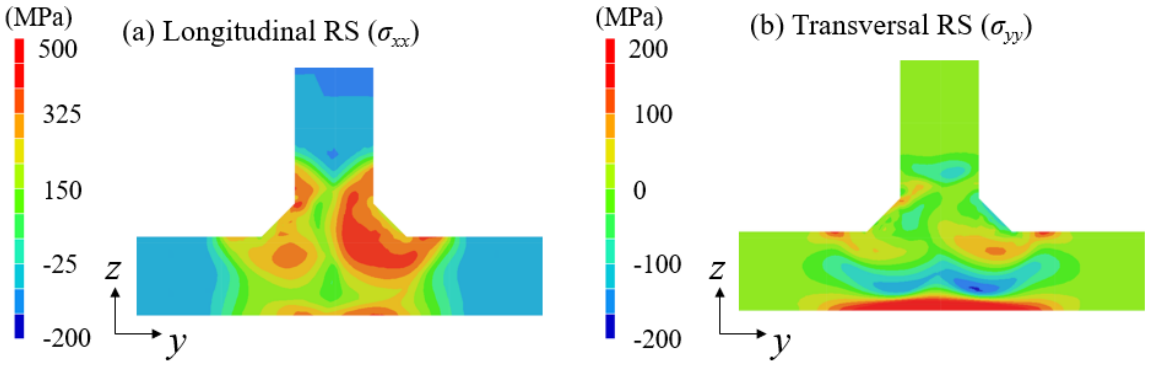

Fig. A.4 Distribution of as-welded RS on the center cross-section.

After welding simulation, cutting analysis was performed to obtain the redistributed RS on the remaining mesh model. The longitudinal and transversal RS distributions before and after cutting are shown in Figs. A.5 and A.6. After cutting, the peak tensile RS in the longitudinal direction is reduced by half, from 438 MPa to 224 MPa. For transversal RS, only a small amount of stress relaxation, less than 10 MPa, was observed. Therefore, the transverse RS which remains at a high value after cutting still has a significant influence on the fracture mechanics calculations.

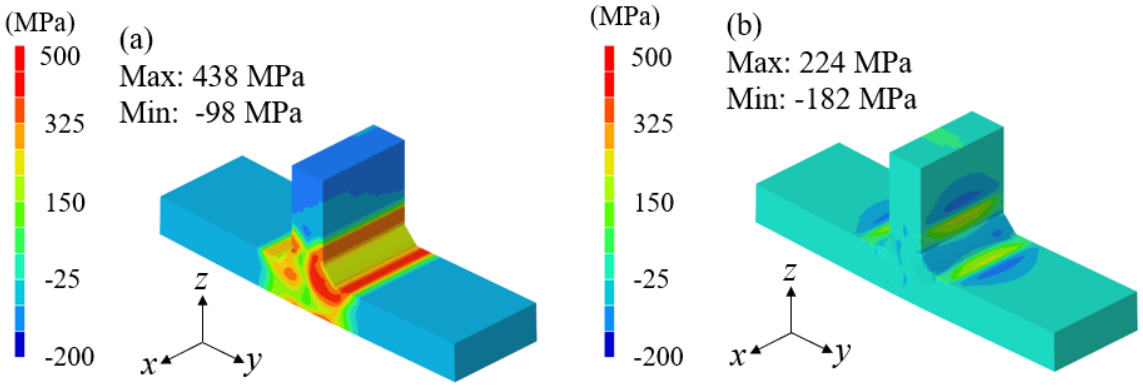

Fig. A.5 Comparison of longitudinal RS (σ_{xx}) before and after cutting analysis. (a) As-welded condition, and (b) After cutting condition.

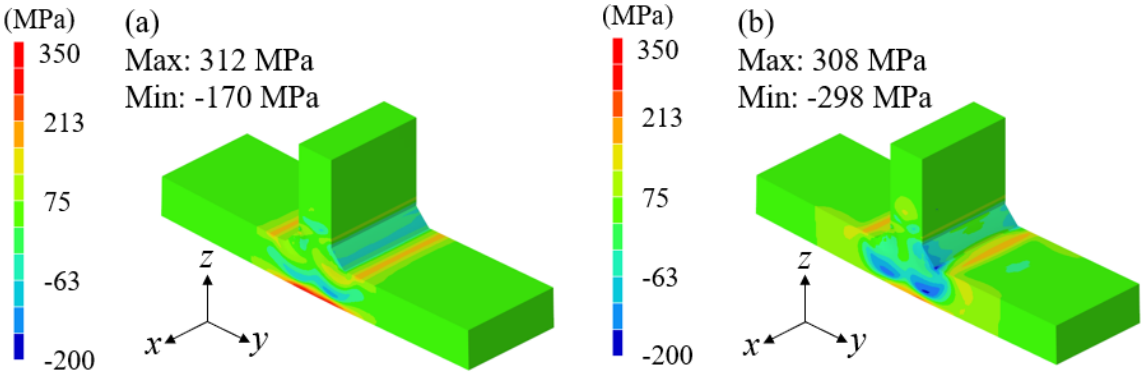

Fig. A.6 Comparison of transversal RS (σ_{yy}) before and after cutting analysis. (a) As-welded condition, and (b) After cutting condition.

A.3 Post weld treatment analysis

The target structure for the analysis has the same geometry as the cut welded joint mentioned in Section A.1 (see Fig. A.7). The HFMI equipment modeled in this simulation is referred to PITec Weld Line 10 device which is also used in Ernould et al. work [20]. The numerical simulation parameters adopted in this study were optimized by Valdes [10] so that the measurement data can be well simulated. The peening tool used in this simulation has a conical pin at the tip with a radius of 2.0 mm. The peening tool is modeled as a rigid shell and 8-nodes hexahedral elements are used for the welded joint in which the smallest element size is 0.2×0.2×0.2 mm. The FE mesh of the welded joint and peening tool used in the analysis is shown in Fig. A.8.

Peening is performed for 8 mm length at the weld toe in the middle of the joint. The simulation parameters are shown in Table A.2.

Table A.2 HFMI parameters.

Pitch (mm)	Pin Indentation (mm)	Frequency (Hz)	Linear Velocity (mm/s)
0.4	0.4	100	40

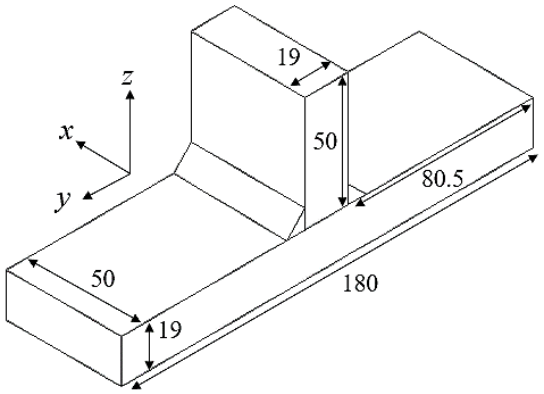

Fig. A.7 Geometry of the welded joint used in HFMI-treatment simulation. (All dimensions are in millimeters.)

The material parameters used in this analysis are shown in Table A.3.

Table A.3 Material parameters used in HFMI-treatment analysis.

Yield Stress, σ_0 (MPa)	C_1 (MPa)	C_2 (MPa)	γ_1	γ_2
435	8971.8	12654.8	218.65	106.98

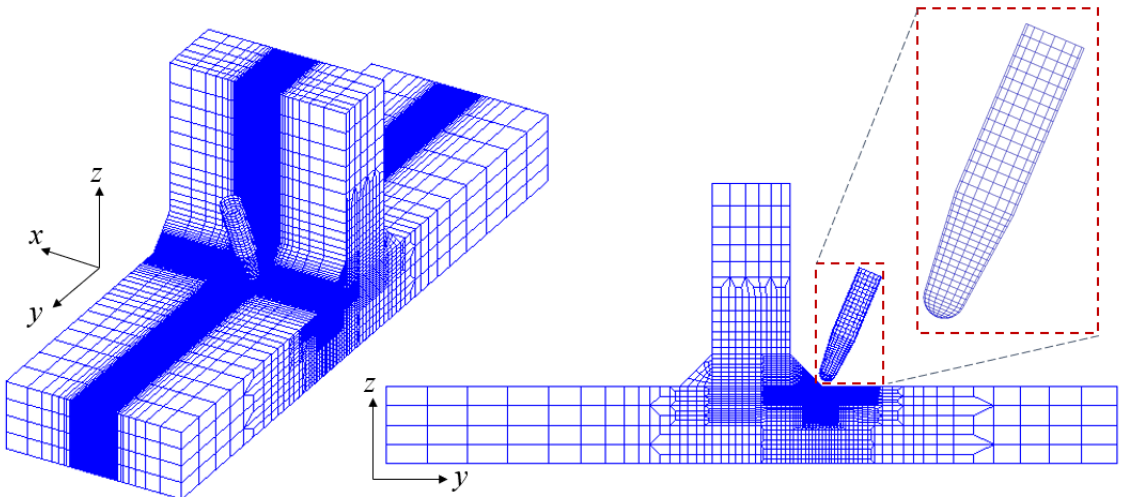

Fig. A.8 FE model of the welded-joint for HFMI-treatment simulation.

A.4 Importing the welding RS to HFMI simulation

The implicit elastic-plastic analysis in JWRIAN and explicit elastic-plastic analysis in MSC Dytran uses different element formulations, and different FE mesh models are used in each analysis. The welding RS of the cut specimen obtained by JWRIAN is interpolated and employed as the initial stress for the HFMI-treatment simulation in Dytran. Fig. A.9 shows the distribution in the through-thickness direction of RS after cutting simulation, after interpolation, and after achieving equilibrium condition in MSC Dytran. Longitudinal welding RS before and after interpolation, and after achieving equilibrium are in good agreement. In the case of transversal RS, a small deviation between the initial RS and RS after achieving equilibrium was observed near the upper surface of the joint which can be neglected.

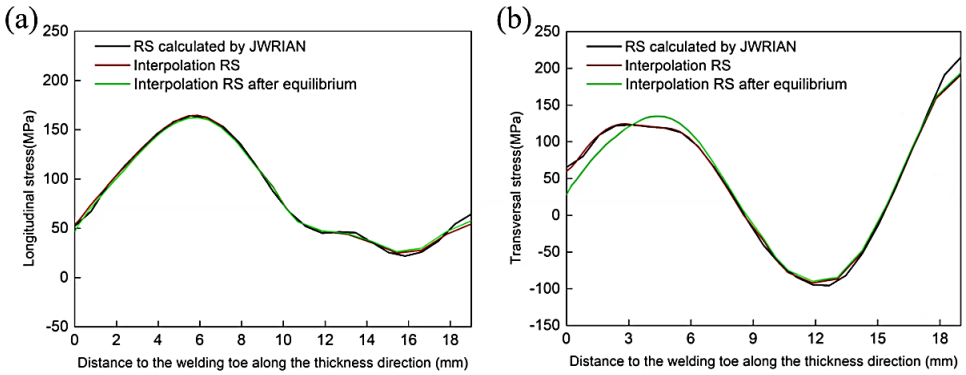

Fig. A.9 Through-thickness RS distribution. (a) Longitudinal RS, and (b) Transversal RS.

A.5 Results and discussions for post weld treatment analysis

The HFMI simulations are carried out for 2 different cases: stress-free peening and peening with initial welding RS. A stress-free welded joint was used in the first case and the interpolated welding RS is imported as the initial stress in the latter case. However, the maximum compressive RS after peening given in the two cases are not substantially different: 1.26% in the case of σ_{xx} and 6.46% in σ_{yy} (see Figs. A.10 and A.11). Maximum compressive stresses are observed up to a depth of around 4.3 mm at the weld toe for all stress components. The high tensile RS after welding around the weld toe completely vanishes after HFMI simulation.

The effective plastic strain and deformation around the weld toe are as shown in Fig. A.12. The parameters of the deformed profile after HFMI simulations at the weld transition region are well within the range recommended by the IIW. The measured peening depth is 0.246 mm at the maximum deformed location while the IIW recommendation is between

0.2-0.6 mm [19]. The recommended width of the peening region is 3-6 mm [19] and the simulation gives 3.53 mm. Although the enforced displacement penetration of the tool is set as 0.4 mm peening depth, the actual deformed depth is short of 0.154 mm which is due to spring back during peening.

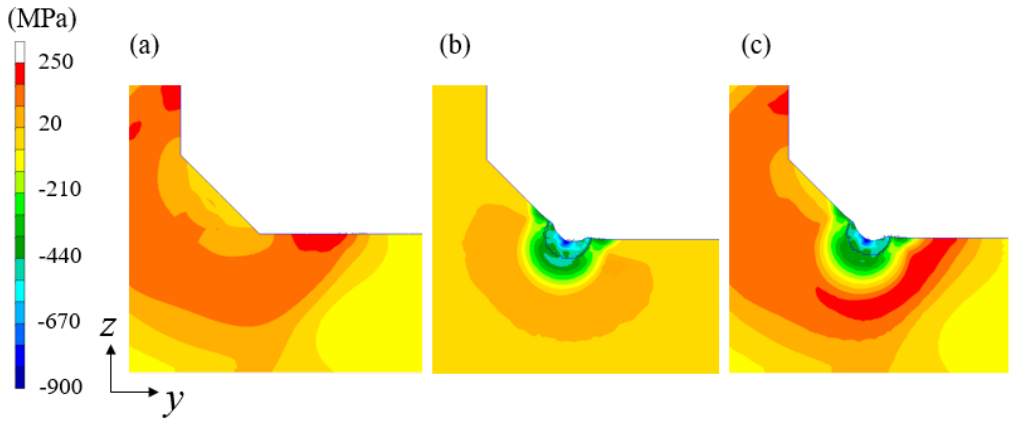

Fig. A.10 Longitudinal stress (σ_{xx}) distribution at the center cross-section. (a) Welding, (b) Stress-free peening, and (c) Peening with initial welding RS.

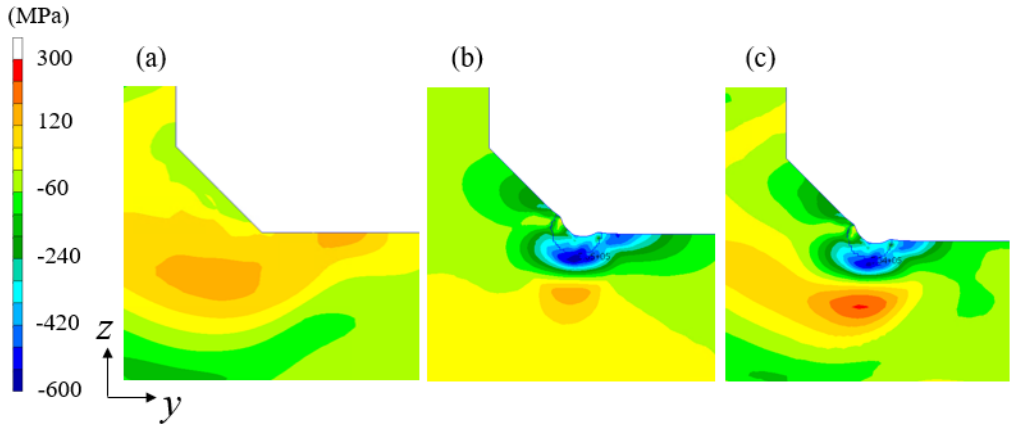

Fig. A.11 Transversal stress (σ_{yy}) distribution at the center cross-section. (a) Welding, (b) Stress-free peening, and (c) Peening with initial welding RS.

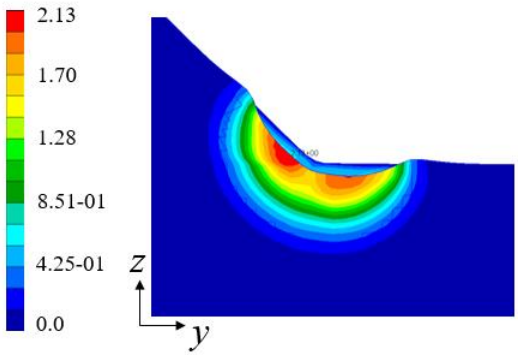

Fig. A.12 Effective plastic strain at the HFMI-treated region

B Welding analysis for Bowness T-joint

B.1 Analysis condition

The parameters of the TEP model were chosen to be suitable for the welding analysis of the Bowness's T-joint [72]. The geometric configuration of the TEP model is shown in Fig. B.1. The model is an as-welded joint (ρ = 0.0) with a flank angle (θ) of 45°. The height and length of the weld-bead are 9.0 mm, respectively, which are adopted from [72–74]. The 8-node hexahedral elements were employed in the TEP model and the mesh has been optimized for efficient welding analysis (see Fig. B.2). The boundary conditions (*x*, *y*, *z* constraints which are shown as blue arrows in Fig. B.2) were applied to prevent rigid body motion.

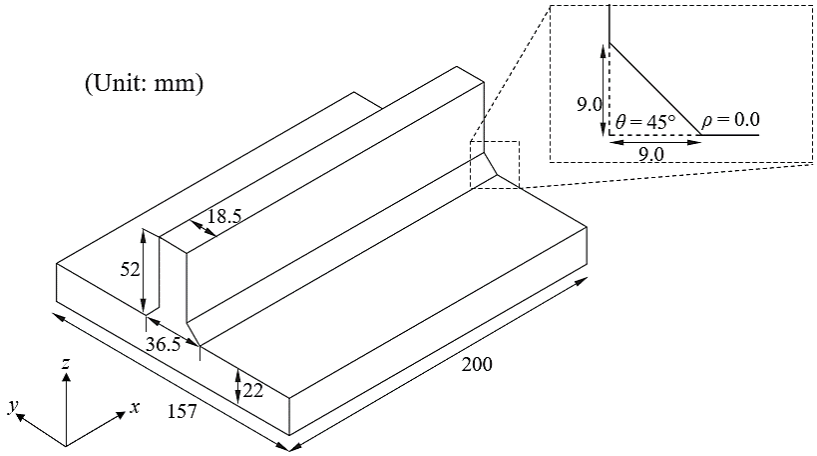

Fig. B.1 Geometric configurations of the TEP model.

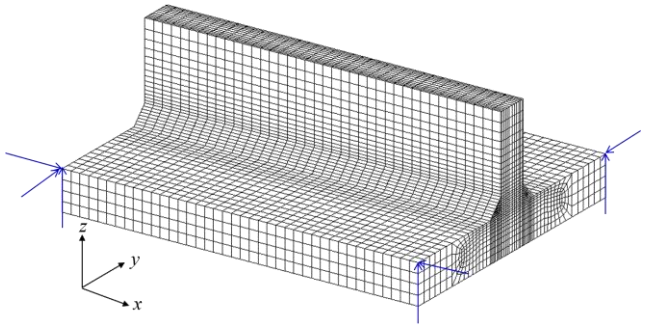

Fig. B.2 FE mesh and boundary conditions of the TEP model.

For the heat source in thermal analysis, a half ellipsoid moving heat source was employed [86]. The shielded metal arc welding was simulated with welding conditions; heat input = 2,000 J/mm and welding speed = 8.0 mm/sec. The sequence of welding and weld direction are shown in Fig. B.3 in which two welding passes are represented by green and blue colors and the base metal in red color. The welding simulation was carried out using mild steel

(SM 400B) properties [17]. The same temperature-dependent material properties were used for both base metal and filler metal. Fig. B.4(a) and (b) show the temperature-dependent thermal-physical properties and mechanical properties used in welding simulation. The initial room and inter-pass temperatures were set to 20°C.

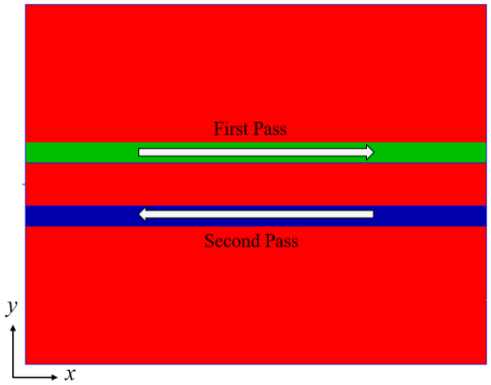

Fig. B.3 Sequence of the applied weld passes.

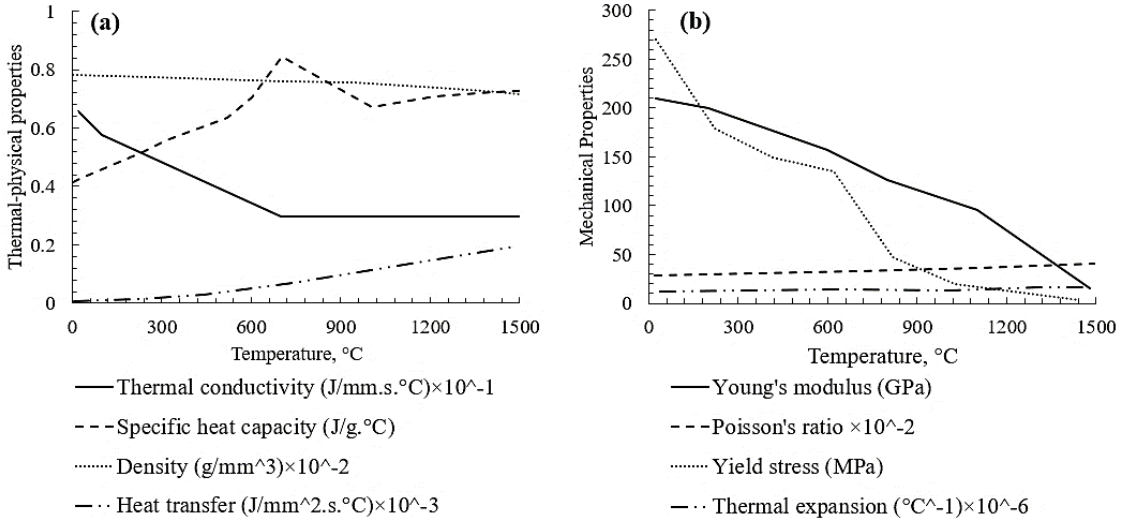

Fig. B.4 Temperature-dependent material properties used in TEP analysis. (a) Temperature-dependent thermal-physical properties and (b) Temperature-dependent mechanical properties. [17]

B.2 Results and discussion

The welding simulation was carried out using the analysis conditions mentioned in Section B.1, and the results obtained are discussed in this section. The thermal distribution of the weld profile at the mid-length of the model is shown in Fig. B.5. It shows the three typical regions of a welded joint: fusion zone, heat affected zone, and unaffected base material. The size and shape of the fusion and heat affect zones show realistic thermal distribution.

The longitudinal welding RS (σ_{xx}), transversal welding RS (σ_{yy}), and von Mises welding RS, obtained by the mechanical simulation after the model has cooled down to room temperature, are shown in Figs. B.6-8, respectively. Referring to Fig. B.6(a) and (b), the large tensile welding RS was obtained at and near the weld region and compressive RS at the edges of the model which is a typical longitudinal welding RS distribution. High-tensile transversal welding RS (σ_{yy}) in 3D view and *x*-*y* plane view (Fig. B.7(a) and (b), respectively) are also observed near the weld region. In the case of von-Mises stress (see Fig. B.8(a) and (b)), as the strain hardening was considered during the welding simulation, the maximum von-Mises stress is larger than the material initial yield stress. To consider the induced welding RS in calculating SIFs and fatigue life, the surface cracks were placed at the weld toe of the joint. The welding RS was interpolated to be employed in the fracture analysis following the crack size and location as shown in Fig. B.9 in which the dashed box represents the location of cracks.

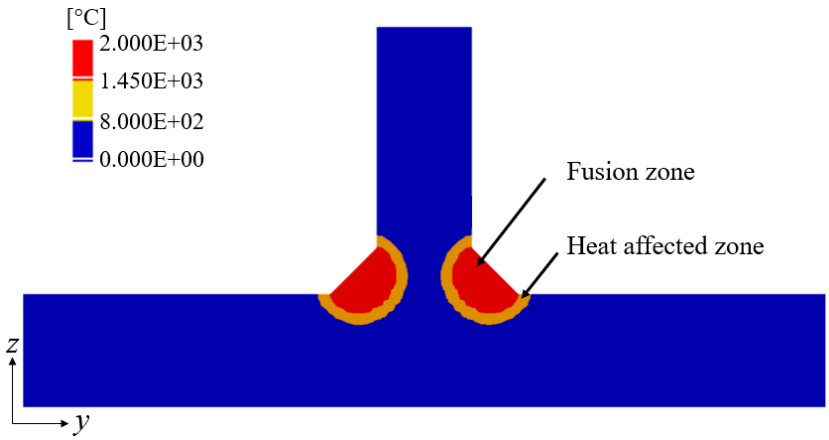

Fig. B.5 Fusion zone and heat affected zone at the mid-length of the welded joint.

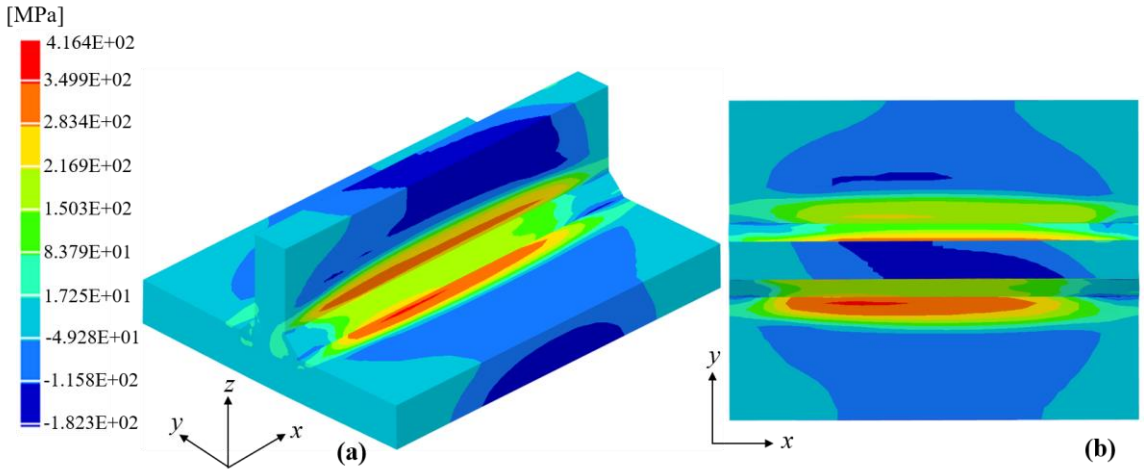

Fig. B.6 Longitudinal welding RS (σ_{xx}). (a) 3D view and (b) *x*-*y* plane view.

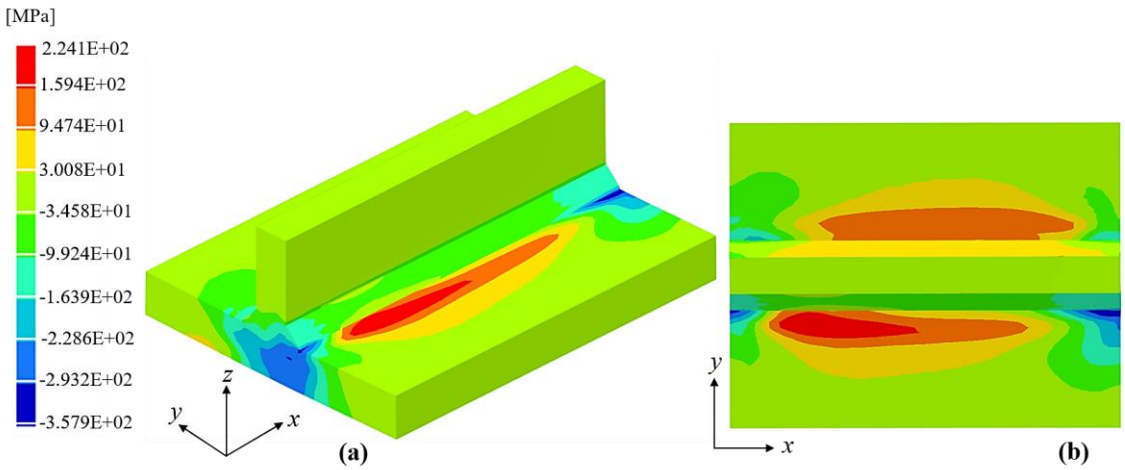

Fig. B.7 Transversal welding RS (σ_{yy}). (a) 3D view and (b) *x*-*y* plane view.

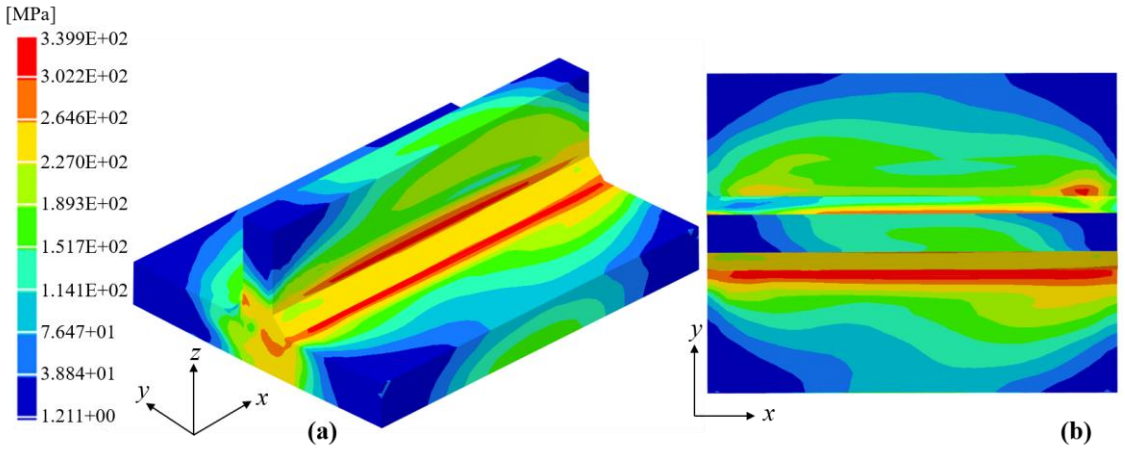

Fig. B.8 von-Mises welding RS. (a) 3D view and (b) *x*-*y* plane view.

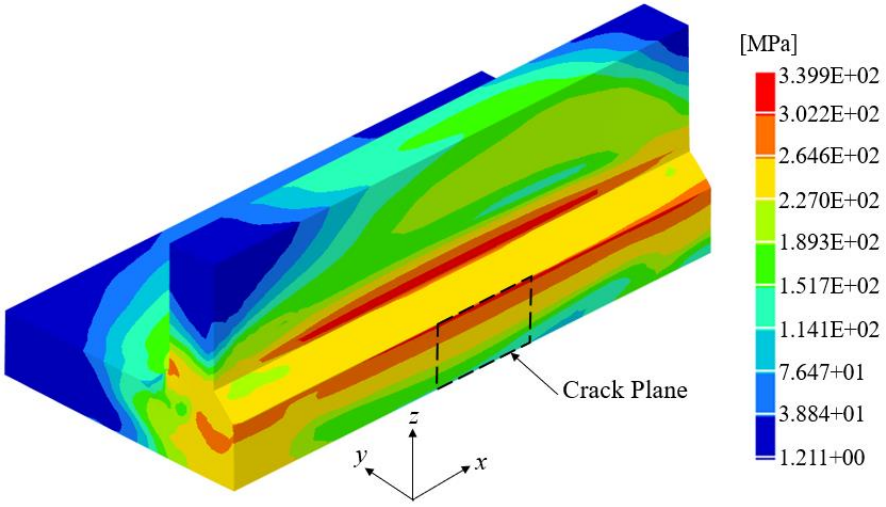

Fig. B.9 Section view (*x*-*z* plane) of von Mises welding RS distribution on the crack plane.

C Comparison of solutions for weld modification factor method

C.1 The proposed μ_k method

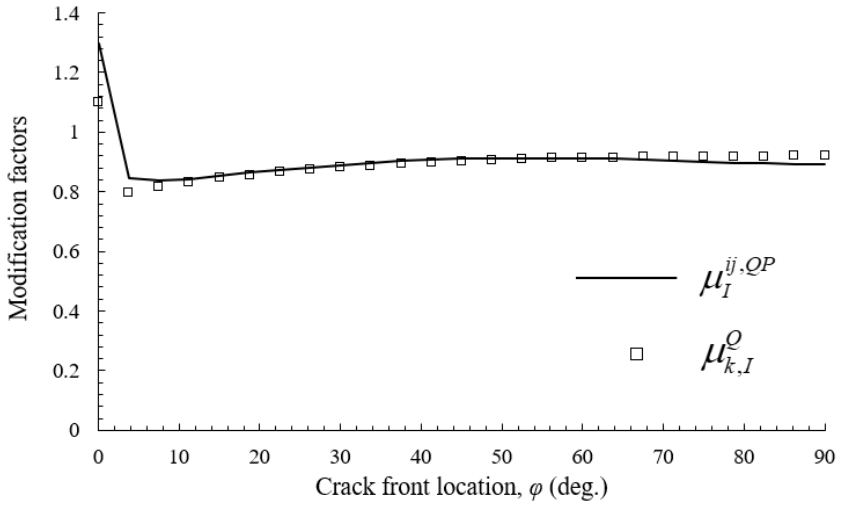

Fig. C.1 Comparison of $\mu_I^{ij,QP}$ and $\mu_{k,I}^{Q}$ for Crack No. 1.

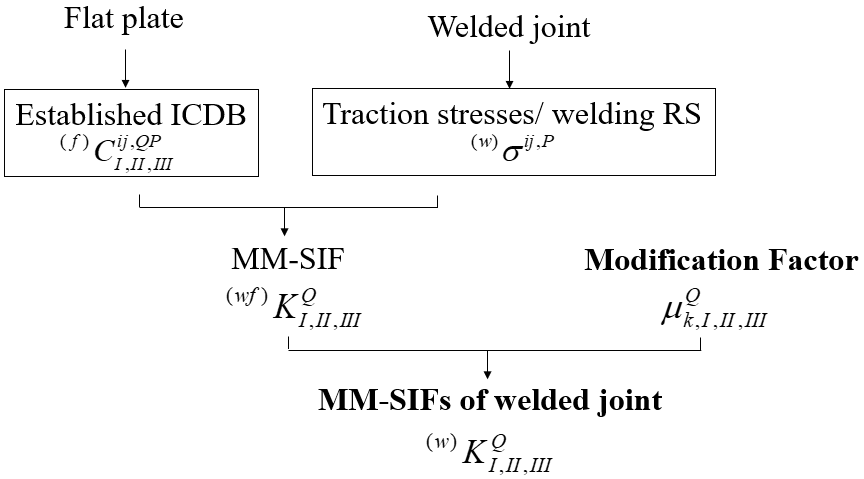

Fig. C.2 Procedures for the application of the proposed μ_k method and equations.

C.2 Validation of FE mesh and NIFM calculation system

Figures C.3-8 show the additional information on comparisons of SIF solutions obtained by using NIFM and reference solutions for Cracks No. 2-7, respectively which has mentioned in Section 6.3. In each figure, (a), (b), and (c) correspond to the F_I, F_{II}, and F_{III} of welded joints, and F_I of the flat plate are shown in (d).

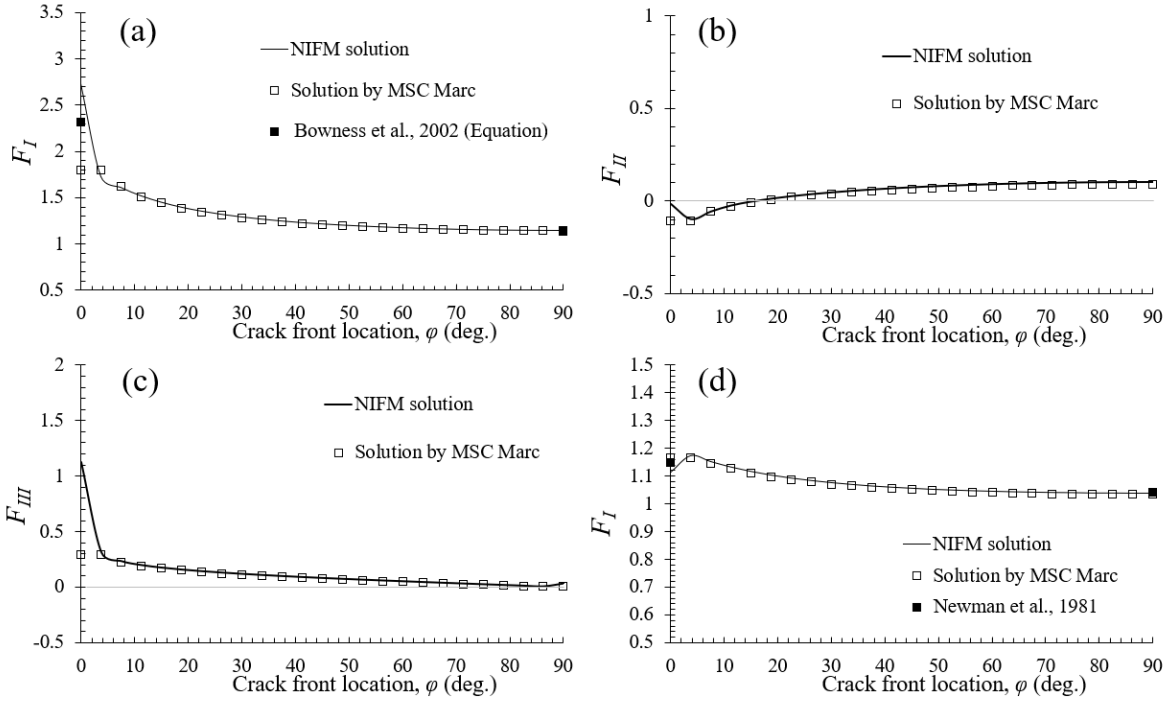

Fig. C.3 Comparison of SIF solutions for Crack No. 2. (a) F_I, (b) F_{II}, (c) F_{III} of the welded joint, and (d) F_I of the flat plate.

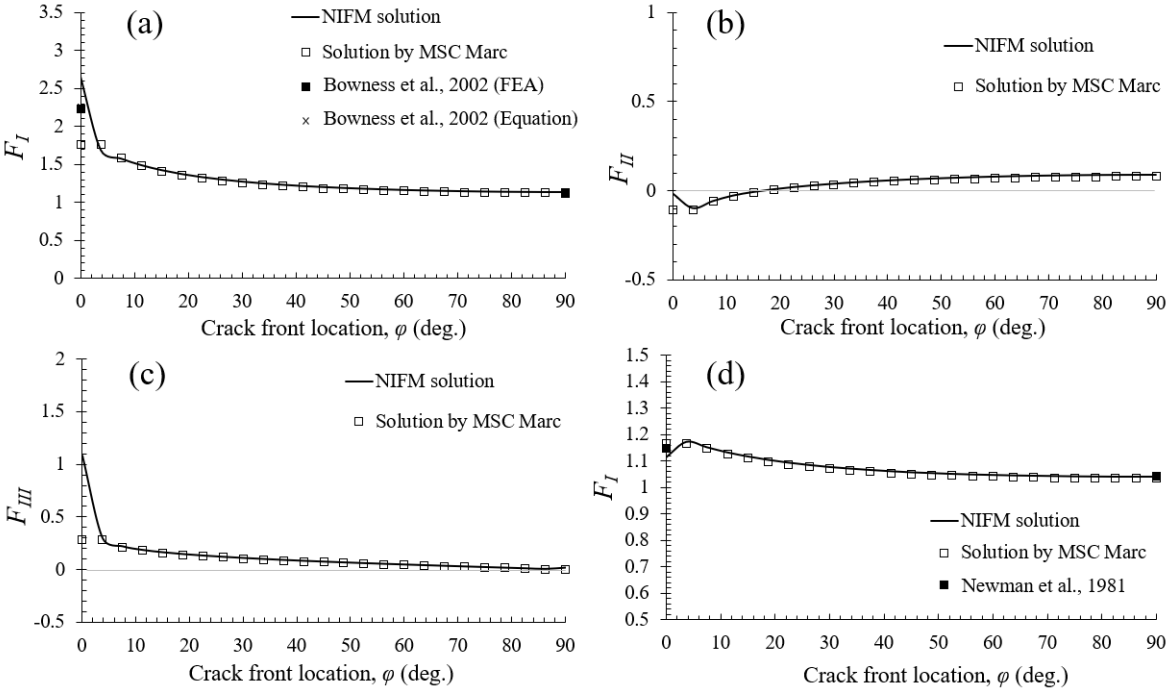

Fig. C.4 Comparison of SIF solutions for Crack No. 3. (a) F_I, (b) F_{II}, (c) F_{III} of the welded joint, and (d) F_I of the flat plate.

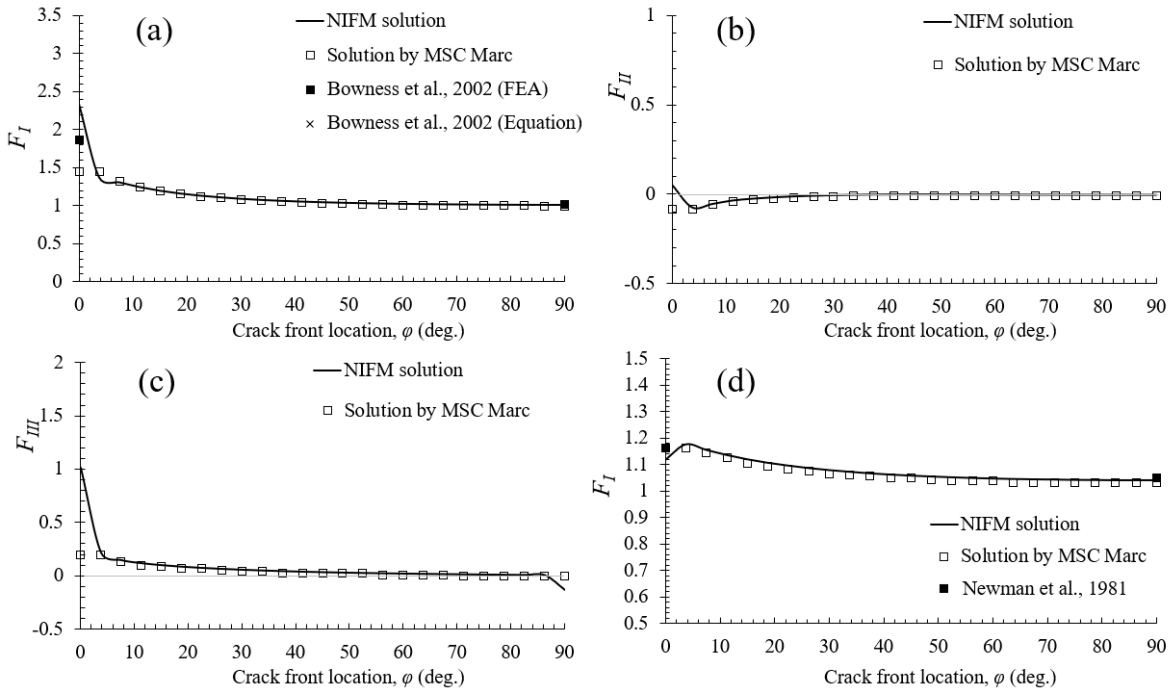

Fig. C.5 Comparison of SIF solutions for Crack No. 4. (a) F_I, (b) F_{II}, (c) F_{III} of the welded joint, and (d) F_I of the flat plate.

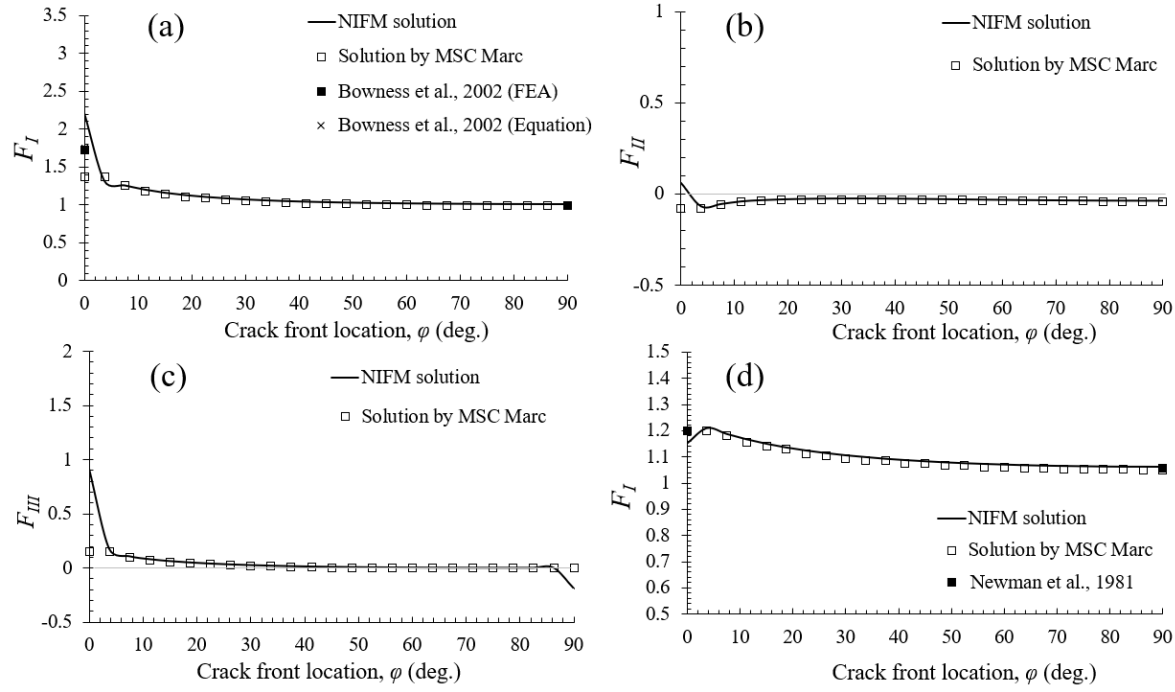

Fig. C.6 Comparison of SIF solutions for Crack No. 5. (a) F_I, (b) F_{II}, (c) F_{III} of the welded joint, and (d) F_I of the flat plate.

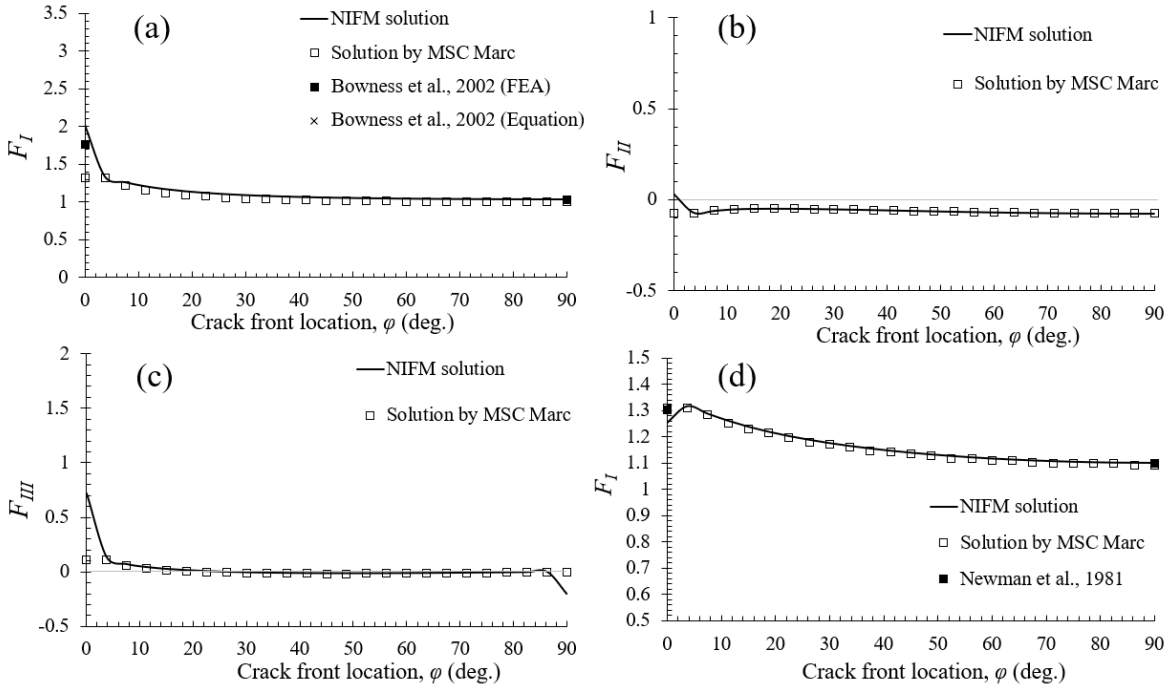

Fig. C.7 Comparison of SIF solutions for Crack No. 6. (a) F_I, (b) F_{II}, (c) F_{III} of the welded joint, and (d) F_I of the flat plate.

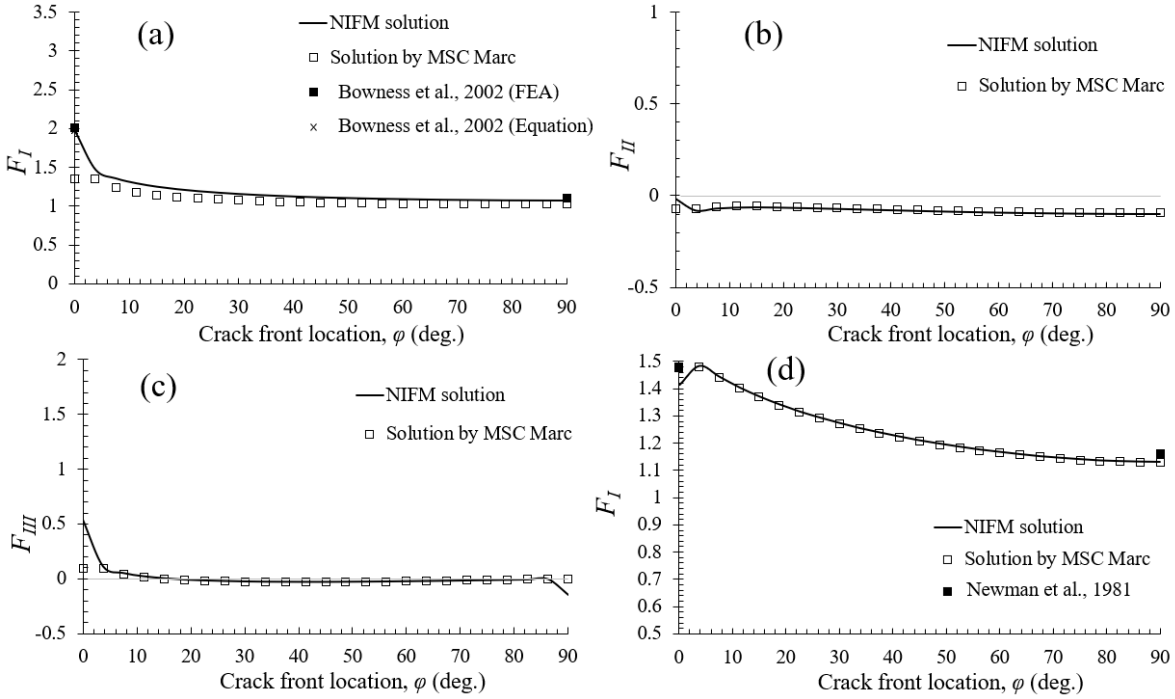

Fig. C.8 Comparison of SIF solutions for Crack No. 7. (a) F_I, (b) F_{II}, (c) F_{III} of the welded joint, and (d) F_I of the flat plate.

C.3 Comparison of μ_k given by numerical solutions and proposed μ_k equations

Tables C.1-3 list the μ_k values and percentage differences between those given by numerical solutions and proposed μ_k equations in Section 6.4.2.

Table C.1 Comparison between $\mu_{k,I}$ obtained by numerical solutions and proposed equations.

φ *(deg.)*	a/T	μ_k from numerical solutions	μ_k by equations	Difference (%)
0	0.07	1.098719	1.087914	0.983
	0.091	1.100278	1.104484	-0.38
	0.1	1.100965	1.111160	-0.926
	0.2	1.167823	1.164997	0.242
	0.3	1.189786	1.187505	0.192
	0.5	1.163193	1.164913	-0.148
	0.7	1.096584	1.096140	0.040
15	0.07	0.846304	0.843959	0.277
	0. 091	0.848995	0.845441	0.419
	0.1	0.850000	0.846073	0.462
	0.2	0.852739	0.852546	0.023
	0.3	0.864781	0.858134	0.769
	0.5	0.872311	0.866656	0.648
	0.7	0.870745	0.871639	-0.103
30	0.07	0.881170	0.876655	0.512
	0. 091	0.883810	0.878060	0.651
	0.1	0.884679	0.878659	0.680
	0.2	0.884877	0.884761	0.013
	0.3	0.896224	0.889979	0.697
	0.5	0.899449	0.897761	0.188
	0.7	0.895866	0.902004	-0.685
45	0.07	0.902244	0.900469	0.197
	0. 091	0.904408	0.901796	0.289
	0.1	0.905192	0.902361	0.313
	0.2	0.904866	0.908094	-0.357

Table C.1 *(Continued.)* Comparison between $\mu_{k,I}$ obtained by numerical solutions and proposed equations.

φ (deg.)	*a*/*T*	μ_k from numerical solutions	μ_k by equations	Difference (%)
45	0.3	0.915043	0.912941	0.230
	0.5	0.917053	0.919983	-0.320
	0.7	0.916033	0.923485	-0.814
60	0.07	0.914001	0.915399	-0.153
	0.091	0.916342	0.916649	-0.034
	0.1	0.916824	0.917180	-0.039
	0.2	0.917011	0.922543	-0.603
	0.3	0.926402	0.927020	-0.067
	0.5	0.928639	0.933322	-0.504
	0.7	0.932409	0.936084	-0.394
75	0.07	0.918730	0.921446	-0.296
	0. 091	0.920777	0.922618	-0.200
	0.1	0.922072	0.923116	-0.113
	0.2	0.922871	0.928109	-0.568
	0.3	0.932063	0.932216	-0.016
	0.5	0.934908	0.937778	-0.307
	0.7	0.943590	0.943589	0.000
90	0.07	0.919696	0.918610	0.118
	0. 091	0.922189	0.919705	0.269
	0.1	0.923452	0.920169	0.356
	0.2	0.924405	0.924792	-0.042
	0.3	0.933716	0.928529	0.556
	0.5	0.937046	0.933350	0.394
	0.7	0.947850	0.934632	1.395

Table C.2 Comparison between $\mu_{k,II}$ obtained by numerical solutions and proposed equations.

φ (deg.)	*a/T*	μ_k from numerical solutions	μ_k by equation	Differences (%)
3.75	0.07	-3.459435	-3.447817	0.336
	0.091	-3.329843	-3.333085	-0.097
	0.1	-3.287977	-3.285496	0.076
	0.2	-2.838898	-2.885412	-1.638
	0.3	-2.852713	-2.804680	1.684
	0.5	-4.118548	-4.135800	-0.419
	0.7	-8.351213	-8.347912	0.040
90	0.07	0.426759	0.426534	0.053
	0.091	0.373695	0.374667	-0.260
	0.1	0.350047	0.349340	0.202
	0.2	-0.040331	-0.040100	0.573
	0.3	-0.497120	-0.496650	0.095
	0.5	-3.270965	-3.269750	0.037
	0.7	-22.519201	-22.516850	0.010

Table C.3 Comparison between $\mu_{k,III}$ obtained by numerical solutions and proposed equations.

φ (deg.)	*a/T*	μ_k from numerical solutions	μ_k by equation	Differences (%)
3.75	0.07	0.668062	0.667050	0.152
	0.091	0.661555	0.662406	-0.129
	0.1	0.658837	0.660541	-0.259
	0.2	0.648381	0.646204	0.336
	0.3	0.642939	0.643189	-0.039
	0.5	0.670112	0.671125	-0.151
	0.7	0.744706	0.744349	0.048

C.4 Comparison of MM-SIF solutions given by numerical method and proposed method under membrane loading

Tables C.4-6 describe the MM-SIF solutions and percentage differences between those given by numerical solutions and proposed equations in Section 6.4.3.

Table C.4 Comparison between F_I obtained by NIFM and proposed μ_k method under membrane loading.

φ (deg.)	a/T	F_I by NIFM method	F_I by μ_k method	Differences (%)
0	0.07	2.938809	2.909908	0.983
	0. 091	2.727836	2.738265	-0.382
	0.1	2.656418	2.681017	-0.926
	0.2	2.344481	2.338807	0.242
	0.3	2.208656	2.204421	0.192
	0.5	2.026973	2.029969	-0.148
	0.7	1.970376	1.969579	0.040
15	0.07	1.552188	1.530351	1.407
	0. 091	1.454095	1.431664	1.543
	0.1	1.421055	1.398551	1.584
	0.2	1.202850	1.189260	1.130
	0.3	1.159657	1.138206	1.850
	0.5	1.169295	1.149431	1.699
	0.7	1.252727	1.241094	0.929
30	0.07	1.375917	1.357404	1.346
	0. 091	1.295660	1.276496	1.479
	0.1	1.268800	1.249676	1.507
	0.2	1.096878	1.087783	0.829
	0.3	1.071752	1.055760	1.492
	0.5	1.089188	1.078736	0.960
	0.7	1.159071	1.158268	0.069
45	0.07	1.290992	1.281124	0.764
	0. 091	1.220513	1.210103	0.853
	0.1	1.197150	1.186670	0.875
	0.2	1.052124	1.050064	0.196
	0.3	1.035900	1.027966	0.766

Table C.4 *(Continued)* Comparison between F_I obtained by NIFM and proposed μ_k method under membrane loading.

φ (deg.)	*a/T*	F_I by NIFM method	F_I by μ_k method	Differences (%)
45	0.5	1.056878	1.054812	0.196
	0.7	1.115290	1.118838	-0.318
60	0.07	1.243891	1.241847	0.164
	0. 091	1.179808	1.176494	0.281
	0.1	1.158339	1.155160	0.274
	0.2	1.031014	1.034109	-0.300
	0.3	1.019698	1.017422	0.223
	0.5	1.042459	1.044906	-0.235
	0.7	1.092722	1.094314	-0.146
75	0.07	1.218200	1.220901	-0.222
	0. 091	1.157264	1.158749	-0.128
	0.1	1.137441	1.137927	-0.043
	0.2	1.020459	1.025633	-0.507
	0.3	1.012114	1.011774	0.034
	0.5	1.035516	1.038383	-0.277
	0.7	1.079633	1.075187	0.412
90	0.07	1.209636	1.210235	-0.050
	0.091	1.150375	1.149225	0.100
	0.1	1.130874	1.128776	0.186
	0.2	1.017082	1.019336	-0.222
	0.3	1.010046	1.006333	0.368
	0.5	1.033380	1.031443	0.187
	0.7	1.074668	1.062091	1.170

Table C.5 Comparison between F_{II} obtained by NIFM and proposed μ_k method under membrane loading.

φ (deg.)	*a/T*	F_{II} by NIFM method	F_{II} by μ_k method	Differences (%)
3.75	0.07	-0.108332	-0.107968	0.336
	0.091	-0.099570	-0.099667	-0.097
	0.1	-0.096668	-0.096595	0.076
	0.2	-0.075490	-0.076699	-1.602

Table C.5 *(Continued)* Comparison between normalized SIFs F_{II} obtained by NIFM and proposed μ_k method under membrane loading.

φ (deg.)	*a/T*	F_{II} by NIFM method	F_{II} by μ_k method	Differences (%)
3.75	0.3	-0.069772	-0.068598	1.683
	0.5	-0.071803	-0.072103	-0.418
	0.7	-0.080815	-0.080783	0.040
90	0.07	0.136807	0.136735	0.053
	0.091	0.100885	0.101147	-0.260
	0.1	0.088368	0.088190	0.201
	0.2	-0.005345	-0.005314	0.580
	0.3	-0.038678	-0.038642	0.093
	0.5	-0.077490	-0.077461	0.037
	0.7	-0.099252	-0.099242	0.010

Table C.6 Comparison between normalized SIFs F_{III} obtained by NIFM and proposed μ_k method under membrane loading.

φ (deg.)	*a/T*	F_{III} by NIFM method	F_{III} by μ_k method	Differences (%)
3.75	0.07	0.353042	0.352508	0.151
	0.091	0.313363	0.313766	-0.129
	0.1	0.299795	0.300570	-0.259
	0.2	0.215576	0.214852	0.336
	0.3	0.174052	0.174120	-0.039
	0.5	0.131589	0.131788	-0.151
	0.7	0.112703	0.112648	0.049

C.5 Comparison of MM-SIF solutions given by numerical method and proposed μ_k method under membrane loading considering welding RS

The MM-SIF solutions under membrane loading considering welding RS obtained by NIFM and those calculated by the μ_k method, and percentage differences are listed in Tables C.7-9.

Table C.7 Comparison between F_I obtained by NIFM and μ_k method under membrane loading considering welding RS.

φ *(deg.)*	a/T	F_I by NIFM method	F_I by μ_k method	Differences (%)
0	0.07	5.495816	5.392260	1.884
	0.091	5.277198	5.174552	1.945
	0.1	5.201780	5.097221	2.010
	0.2	4.994636	4.886185	2.171
	0.3	5.005415	4.888985	2.326
	0.5	4.862493	4.739751	2.524
	0.7	5.131868	5.023691	2.108
15	0.07	3.537561	3.451051	2.445
	0.091	3.430461	3.350531	2.330
	0.1	3.394412	3.316134	2.306
	0.2	3.127242	3.065990	1.959
	0.3	3.163891	3.106330	1.819
	0.5	3.271035	3.221384	1.518
	0.7	3.642408	3.607852	0.949
30	0.07	3.354153	3.284466	2.078
	0.091	3.265763	3.202344	1.942
	0.1	3.235588	3.174112	1.900
	0.2	3.007336	2.962990	1.475
	0.3	3.044961	3.006713	1.256
	0.5	3.148204	3.115053	1.053
	0.7	3.430273	3.410698	0.571
45	0.07	3.273511	3.214281	1.809
	0.091	3.195626	3.141050	1.708
	0.1	3.170506	3.116913	1.690
	0.2	2.968916	2.934411	1.162
	0.3	2.994975	2.966700	0.944
	0.5	3.092129	3.063379	0.930
	0.7	3.315178	3.301424	0.415
60	0.07	3.232119	3.179848	1.617
	0.091	3.163689	3.115359	1.528
	0.1	3.141249	3.092919	1.539

Table C.7 *(Continued)* Comparison between F_I obtained by NIFM and μ_k method under membrane loading considering welding RS.

φ *(deg.)*	a/T	F_I by NIFM method	F_I by μ_k method	Differences (%)
60	0.2	2.967227	2.936629	1.031
	0.3	2.983599	2.959775	0.798
	0.5	3.049405	3.027693	0.712
	0.7	3.249732	3.240502	0.284
75	0.07	3.210710	3.160894	1.552
	0.091	3.148033	3.101029	1.493
	0.1	3.126919	3.082543	1.419
	0.2	2.976516	2.948773	0.932
	0.3	3.003594	2.980114	0.782
	0.5	3.044065	3.025664	0.604
	0.7	3.193313	3.187793	0.173
90	0.07	3.204287	3.155030	1.537
	0.091	3.146155	3.100585	1.448
	0.1	3.126919	3.083298	1.395
	0.2	2.987493	2.959919	0.923
	0.3	3.023588	2.999559	0.795
	0.5	3.076108	3.055102	0.683
	0.7	3.218137	3.212882	0.163

Table C.8 Comparison between F_{II} obtained by NIFM and μ_k method under membrane loading considering welding RS.

φ (deg.)	a/T	F_{II} by NIFM method	F_{II} by μ_k method	Differences (%)
3.75	0.07	0.080214	0.082748	-3.159
	0.091	0.085104	0.088677	-4.198
	0.1	0.090697	0.096665	-6.580
	0.2	0.135020	0.126049	6.644
	0.3	0.152920	0.143297	6.293
	0.5	0.173886	0.165101	5.052
	0.7	0.152918	0.142583	6.759
90	0.07	-0.091989	-0.091334	0.712
	0.091	-0.109965	-0.104903	4.603
	0.1	-0.122223	-0.115061	5.860
	0.2	-0.224949	-0.233736	-3.906
	0.3	-0.245824	-0.246961	-0.463
	0.5	-0.282511	-0.314054	-11.165
	0.7	-0.327681	-0.373759	-14.062

Table C.9 Comparison between F_{III} obtained by NIFM and proposed method under membrane loading considering welding RS.

φ (deg.)	a/T	F_{III} by numerical NIFM method	F_{III} by proposed method	Differences (%)
3.75	0.07	0.183051	0.186578	-1.927
	0.091	0.178474	0.182148	-2.059
	0.1	0.165093	0.169464	-2.648
	0.2	0.088915	0.095888	-7.842
	0.3	0.051605	0.052191	-1.136
	0.5	0.016630	0.016747	-0.704
	0.7	0.039426	0.041372	-4.936

References

[1] M.L. Williams, G.A. Ellinger, Investigation of structural failures of welded ships, Weld. J. 32 (1953) 498–528.

[2] T.L. Anderson, Fracture mechanics: fundamentals and application, Third Edit, Taylor & Francis Group, 2005.

[3] W. Fricke, Fatigue and fracture of ship structures, in: Encycl. Marit. Offshore Eng., John Wiley & Sons, Ltd, Chichester, UK, 2017: pp. 1–12. https://doi.org/10.1002/9781118476406.emoe007.

[4] R. Gadallah, N. Osawa, S. Tanaka, Numerical estimation on stress intensity factors for surface cracks in a welding residual stress field, in: Vol. 3 Struct. Saf. Reliab., ASME, 2016: p. V003T02A026. https://doi.org/10.1115/omae2016-54495.

[5] K. Masubuchi, Analysis of welded structures: Residual stresses, distortion and their consequences, Pergamon Press, Oxford, 1980.

[6] A. Hobbacher, Recommendations for fatigue design of welded joints and components, Paris, France, 2008.

[7] M. Leitner, M. Khurshid, Z. Barsoum, Stability of high frequency mechanical impact (HFMI) post-treatment induced residual stress states under cyclic loading of welded steel joints, Eng. Struct. 143 (2017) 589–602. https://doi.org/10.1016/j.engstruct.2017.04.046.

[8] D.Y. Kim, M.H. Kim, Fatigue life estimation for HFMI treated weldments considering weld toe magnification factors, J. Offshore Mech. Arct. Eng. 142 (2020) 1–9. https://doi.org/10.1115/1.4046676.

[9] H.C. Yildirim, G.B. Marquis, Z. Barsoum, Fatigue assessment of high frequency mechanical impact (HFMI)-improved fillet welds by local approaches, Int. J. Fatigue. 52 (2013) 57–67. https://doi.org/10.1016/j.ijfatigue.2013.02.014.

[10] H.O.R. Valdes, Numerical study on the stability of residual stresses induced by HFMI into a welded joint under cyclic loading, Dissertation, Osaka University, 2019. https://doi.org/10.18910/73578.

[11] M. Leitner, D. Simunek, S.F. Shah, M. Stoschka, Numerical fatigue assessment of welded and HFMI-treated joints by notch stress/strain and fracture mechanical

approaches, Adv. Eng. Softw. 120 (2018) 96–106. https://doi.org/10.1016/j.advengsoft.2016.01.022.

[12] P. Paris, F. Erdogan, A critical analysis of crack propagation laws, J. Basic Eng. 85 (1963) 528–533. https://doi.org/10.1115/1.3656900.

[13] J.D. Wood, C.M. Harvey, S. Wang, Partition of mixed-mode fractures in 2D elastic beams with through-thickness shear forces, in: 19th Int. Conf. Compos. Struct., © The Authors, Porto, 2016: pp. 103–103. https://repository.lboro.ac.uk/account/articles/9221621.

[14] D. Sun, J. Gan, Z. Wang, P. Luo, W. Wu, Experimental and analytical investigation of fatigue crack propagation of T-welded joints considering the effect of boundary condition, Fatigue Fract. Eng. Mater. Struct. 40 (2017) 894–908. https://doi.org/10.1111/ffe.12550.

[15] W. Fricke, L. Gao, H. Paetzold, Fatigue assessment of local stresses at fillet welds around plate corners, Int. J. Fatigue. 101 (2017) 169–176. https://doi.org/10.1016/j.ijfatigue.2017.01.011.

[16] S. Tanaka, T. Kawahara, H. Okada, Study on crack propagation simulation of surface crack in welded joint structure, Mar. Struct. 39 (2014) 315–334. https://doi.org/10.1016/j.marstruc.2014.08.001.

[17] R. Gadallah, N. Osawa, S. Tanaka, S. Tsutsumi, Critical investigation on the influence of welding heat input and welding residual stress on stress intensity factor and fatigue crack propagation, Eng. Fail. Anal. 89 (2018) 200–221. https://doi.org/10.1016/j.engfailanal.2018.02.028.

[18] D. Tchoffo Ngoula, H.T. Beier, M. Vormwald, Fatigue crack growth in cruciform welded joints: Influence of residual stresses and of the weld toe geometry, Int. J. Fatigue. 101 (2017) 253–262. https://doi.org/10.1016/j.ijfatigue.2016.09.020.

[19] G.B. Marquis, Z. Barsoum, IIW Recommendations for the HFMI Treatment, Springer Singapore, Singapore, 2016. https://doi.org/10.1007/978-981-10-2504-4.

[20] C. Ernould, J. Schubnell, M. Farajian, A. Maciolek, D. Simunek, M. Leitner, M. Stoschka, Application of different simulation approaches to numerically optimize high-frequency mechanical impact (HFMI) post-treatment process, Weld. World. 63 (2019) 725–738. https://doi.org/10.1007/s40194-019-00701-8.

[21] H.O.R. Valdes, N. Osawa, H. Murakawa, S. Rashed, Stability of compressive residual stress introduced by HFMI technique, Proc. Int. Conf. Offshore Mech. Arct. Eng. - OMAE. 4 (2018) 1–10. https://doi.org/10.1115/OMAE2018-77887.

[22] M. Leitner, S. Gerstbrein, M.J. Ottersböck, M. Stoschka, Fatigue strength of HFMI-treated high-strength steel joints under constant and variable amplitude block loading, Procedia Eng. 101 (2015) 251–258. https://doi.org/10.1016/j.proeng.2015.02.036.

[23] H. Ruiz, N. Osawa, S. Rashed, A practical analysis of residual stresses induced by high-frequency mechanical impact post-weld treatment, Weld. World. 63 (2019) 1255–1263. https://doi.org/10.1007/s40194-019-00753-w.

[24] H.C. Yildirim, G.B. Marquis, Fatigue strength improvement factors for high strength steel welded joints treated by high frequency mechanical impact, Int. J. Fatigue. 44 (2012) 168–176. https://doi.org/10.1016/j.ijfatigue.2012.05.002.

[25] E. Mikkola, H. Remes, G. Marquis, A finite element study on residual stress stability and fatigue damage in high-frequency mechanical impact (HFMI)-treated welded joint, Int. J. Fatigue. 94 (2017) 16–29. https://doi.org/10.1016/j.ijfatigue.2016.09.009.

[26] M. Leitner, M. Stoschka, W. Eichlseder, Fatigue enhancement of thin-walled, high-strength steel joints by high-frequency mechanical impact treatment, Weld. World. 58 (2014) 29–39. https://doi.org/10.1007/s40194-013-0097-4.

[27] M. Leitner, Z. Barsoum, F. Schäfers, Crack propagation analysis and rehabilitation by HFMI of pre-fatigued welded structures, Weld. World. 60 (2016) 581–592. https://doi.org/10.1007/s40194-016-0316-x.

[28] Guide to methods for assessing the acceptability of flaws in metallic structures, BS 7910, BSI Standards Limited 2013, 2013.

[29] H.F. Bueckner, A novel principle for the computation of stress intensity factors, Zeitschrift Für Angew. Math. Und Phys. ZAMP. 50 (1970) 529–546.

[30] S.J. Maddox, R.. Andrews, Stress intensity factors for weld toe cracks, in: Proc. Conf. Comput. Aided Assess. Control Localised Damage, Portsmouth, UK, 1990: pp. 329–342.

[31] J.C. Newman, I.S. Raju, An empirical stress-intensity factor equation for the surface crack, Eng. Fract. Mech. 15 (1981) 185–192. https://doi.org/10.1016/0013-7944(81)90116-8.

[32] N. Noda, T. Kihara, D. Beppu, Variations of stress intensity factor of a semi-elliptical surface crack subjected to mixed mode loading, Int. J. Fract. 127 (2004) 167–191. https://doi.org/10.1023/B:FRAC.0000035054.88722.43.

[33] N. Noda, K. Kobayashi, M. Yagishita, Variation of mixed modes stress intensity factors of an inclined semi-elliptical surface crack, Int. J. Fract. 100 (1999) 207–225. https://doi.org/10.1023/A:1018666110597.

[34] N. Noda, S. Miyoshi, Variation of stress intensity factor and crack opening displacement of semi-elliptical surface crack, Int. J. Fract. 75 (1996) 19–48. https://doi.org/10.1007/BF00018524.

[35] G. Shen, G. Glinka, Weight functions for a surface semi-elliptical crack in a finite thickness plate, Theor. Appl. Fract. Mech. 15 (1991) 247–255. https://doi.org/10.1016/0167-8442(91)90023-D.

[36] W. Xu, C. Zhang, X.R. Wu, Y. Yu, Weight function method and its application for orthotropic single edge notched specimens, Compos. Struct. 252 (2020) 112695. https://doi.org/10.1016/j.compstruct.2020.112695.

[37] S. Tanaka, H. Suzuki, S. Sadamoto, S. Okazawa, T.T. Yu, T.Q. Bui, Accurate evaluation of mixed-mode intensity factors of cracked shear-deformable plates by an enriched meshfree Galerkin formulation, Arch. Appl. Mech. 87 (2017) 279–298. https://doi.org/10.1007/s00419-016-1193-x.

[38] S. Tanaka, S. Okazawa, H. Okada, Y. Xi, Y. Ohtsuki, Analysis of three-dimensional surface cracks in a welded joint structure using the shell-solid mixed method, in: Int. Soc. Offshore Polar Eng., 2013.

[39] S. Tanaka, H. Suzuki, S. Sadamoto, M. Imachi, T.Q. Bui, Analysis of cracked shear deformable plates by an effective meshfree plate formulation, Eng. Fract. Mech. 144 (2015) 142–157. https://doi.org/10.1016/j.engfracmech.2015.06.084.

[40] S. Tanaka, H. Suzuki, S. Sadamoto, S. Sannomaru, T. Yu, T.Q. Bui, J-integral evaluation for 2D mixed-mode crack problems employing a meshfree stabilized conforming nodal integration method, Comput. Mech. 58 (2016) 185–198. https://doi.org/10.1007/s00466-016-1288-9.

[41] K. Yagi, S. Tanaka, T. Kawahara, K. Nihei, H. Okada, N. Osawa, Evaluation of crack propagation behaviors in a T-shaped tubular joint employing tetrahedral FE modeling,

Int. J. Fatigue. 96 (2017) 270–282. https://doi.org/10.1016/j.ijfatigue.2016.11.028.

[42] R. Bao, X. Zhang, N.A. Yahaya, Evaluating stress intensity factors due to weld residual stresses by the weight function and finite element methods, Eng. Fract. Mech. 77 (2010) 2550–2566. https://doi.org/10.1016/j.engfracmech.2010.06.002.

[43] R. Gadallah, Evaluation of SIFs for fatigue cracks in welding residual stress fields using the crack face traction force analysis, Dissertation, valdesOsaka University, 2017. https://doi.org/10.18910/67160.

[44] R. Gadallah, N. Osawa, S. Tanaka, Evaluation of stress intensity factor for a surface cracked butt welded joint based on real welding residual stress, Ocean Eng. 138 (2017) 123–139. https://doi.org/10.1016/j.oceaneng.2017.04.034.

[45] R. Gadallah, N. Osawa, S. Tanaka, S. Tsutsumi, A novel approach to evaluate mixed-mode SIFs for a through-thickness crack in a welding residual stress field using an effective welding simulation method, Eng. Fract. Mech. 197 (2018) 48–65. https://doi.org/10.1016/j.engfracmech.2018.04.040.

[46] R. Gadallah, S. Tsutsumi, K. Hiraoka, H. Murakawa, Prediction of residual stresses induced by low transformation temperature weld wires and its validation using the contour method, Mar. Struct. 44 (2015) 232–253. https://doi.org/10.1016/j.marstruc.2015.10.002.

[47] R. Gadallah, S. Tsutsumi, S. Tanaka, N. Osawa, Accurate evaluation of fracture parameters for a surface-cracked tubular T-joint taking welding residual stress into account, Mar. Struct. 71 (2020) 102733. https://doi.org/10.1016/j.marstruc.2020.102733.

[48] F. Iwamatsu, K. Miyazaki, M. Shiratori, Development of evaluation method of stress intensity factor and fatigue crack growth behavior of surface crack under arbitrarily stress distribution by using influence function method, Nihon Kikai Gakkai Ronbunshu, A Hen/Transactions Japan Soc. Mech. Eng. Part A. 77 (2011) 1613–1624. https://doi.org/10.1299/kikaia.77.1613. (in Japanese)

[49] K. Saito, T. Hirashima, N. Ma, H. Murakawa, Characteristic Tensor for Evaluation of Singular Stress Field under Mixed-mode Loadings, Comput. Model. Eng. Sci. 122 (2020) 415–432. https://doi.org/10.32604/cmes.2020.08847.

[50] K. Saito, T. Hirashima, N. Ma, H. Murakawa, Crack singular field evaluation with

characteristic tensor considering residual stress, Weld. Int. 36 (2022) 158–170. https://doi.org/10.1080/09507116.2021.2014662.

[51] K. Saito, T. Hirashima, N. Ma, H. Murakawa, Characteristic-tensor method for efficient estimation of stress-intensity factors of three-dimensional cracks, Eng. Fract. Mech. 257 (2021) 108016. https://doi.org/10.1016/j.engfracmech.2021.108016.

[52] J.R. Rice, Some remarks on elastic crack-tip stress fields, Int. J. Solids Struct. 8 (1972) 751–758. https://doi.org/10.1016/0020-7683(72)90040-6.

[53] J.H. Kim, K.W. Lee, D.C. Seo, S.B. Lee, Calculation of stress intensity factor using weight function method for a patched crack, Key Eng. Mater. 183–187 (2000) 103–108. https://doi.org/10.4028/www.scientific.net/KEM.183-187.103.

[54] I. Gledic, J. Parunov, Application of weight function method in the assessment of crack propagation through stiffened panel, in: Towar. Green Mar. Technol. Transp., 1st Editio, CRC Press, 2015: p. 6.

[55] A. Chattopadhyay, G. Glinka, M. El-Zein, J. Qian, R. Formas, Stress analysis and fatigue of welded structures, Weld. World. 55 (2011) 2–21. https://doi.org/10.1007/BF03321303.

[56] G. Glinka, G. Shen, Universal features of weight functions for cracks in mode I, Eng. Fract. Mech. 40 (1991) 1135–1146. https://doi.org/10.1016/0013-7944(91)90177-3.

[57] P.M. Besuner, The influence function method for fracture mechanics and residual fatigue life analysis of cracked components under complex stress fields, Nucl. Eng. Des. 43 (1977) 115–154. https://doi.org/10.1016/0029-5493(77)90135-2.

[58] M. Shiratori, T. Miyoshi, Analysis of stress intensity factors for surface cracks subjected to arbitrarily distributed stresses, in: G. Yagawa, S.N. Atluri (Eds.), Comput. Mech. ’86, Springer Japan, Tokyo, 1986: pp. 1027–1032. https://doi.org/10.1007/978-4-431-68042-0_148. (in Japanese)

[59] M. Shiratori, T. Miyoshi, Analysis of stress intensity factors for surface cracks subjected to arbitrarily distributed surface stresses (2nd Report), Trans. Japan Soc Mech Eng A. 52 (1986) 390–398. https://doi.org/10.1299/kikaia.52.390. (in Japanese)

[60] M. Shiratori, T. Miyoshi, Y. Sakai, Analysis of stress intensity factors for surface cracks subjected to arbitrarily distributed surface stresses (4th report, Application of

influence coefficients for the cracks originating at the notches and welding joints), Trans. Japan Soc. Mech. Eng. Ser. A. 53 (1987) 1651–1657. https://doi.org/10.1299/kikaia.53.1651. (in Japanese)

[61] M. Shiratori, K. Ubukata, Analysis of stress intensity factors for three dimensional mixed mode cracks by an influence function method, Trans. Japan Soc. Mech. Eng. Ser. A. 56 (1990) 265–271. https://doi.org/10.1299/kikaia.56.265. (in Japanese)

[62] M. Shiratori, M. Nagai, N. Miura, Development of surface crack analysis program and its application to some practical problems, in: ASME 2011 Press. Vessel. Pip. Conf. Vol. 6, Parts A B, ASME, 2011: pp. 929–939. https://doi.org/10.1115/PVP2011-57115.

[63] M. Shiratori, T. Miyoshi, K. Ubukata, Analysis of stress intensity factors for surface cracks subjected to arbitrarily distributed surface stresses, Bull. Fac. Eng. Yokohama Natl. Univ. 35 (1986) 1–25. https://doi.org/10.1007/978-4-431-68042-0_148. (in Japanese)

[64] M. Nagai, N. Miura, M. Shiratori, Stress intensity factor solution for a surface crack with high aspect ratio subjected to an arbitrary stress distribution using the influence function method, Int. J. Press. Vessel. Pip. 131 (2015) 2–9. https://doi.org/10.1016/j.ijpvp.2015.04.003.

[65] N. Osawa, J. Sawamura, S. Okada, K. Shigeta, T. Tsuji, Study on the accuracy of influence factor method when applied to surface cracks in a welded joint of a ship structure, in: Japan Soc. Nav. Archit. Ocean Eng. 12 (2010) 201–208. https://doi.org/10.2534/jjasnaoe.12.201. (in Japanese)

[66] S. İriç, Experimental and numerical investigations of crack growth under mixed-mode loading, Emerg. Mater. Res. 9 (2020) 1319–1324. https://doi.org/10.1680/jemmr.20.00269.

[67] M. Duda, D. Rozumek, G. Lesiuk, M. Smolnicki, B. Babiarczuk, J. Warycha, Fatigue crack growth under mixed-mode I + II and I + III in heat treated 42CrMo4 steel, Int. J. Fract. (2021). https://doi.org/10.1007/s10704-021-00585-0.

[68] A.K. Syed, B. Ahmad, H. Guo, T. Machry, D. Eatock, J. Meyer, M.E. Fitzpatrick, X. Zhang, An experimental study of residual stress and direction-dependence of fatigue crack growth behaviour in as-built and stress-relieved selective-laser-melted

Ti6Al4V, Mater. Sci. Eng. A. 755 (2019) 246–257. https://doi.org/10.1016/j.msea.2019.04.023.

[69] Ž. Božić, S. Schmauder, H. Wolf, The effect of residual stresses on fatigue crack propagation in welded stiffened panels, Eng. Fail. Anal. 84 (2018) 346–357. https://doi.org/10.1016/j.engfailanal.2017.09.001.

[70] W. Elber, The significance of fatigue crack closure, in: Damage Toler. Aircr. Struct., ASTM International, 100 Barr Harbor Drive, PO Box C700, West Conshohocken, PA 19428-2959, 1971: pp. 230–13. https://doi.org/10.1520/STP26680S.

[71] R. Gadallah, N. Osawa, S. Tanaka, Evaluation of stress intensity factor for a surface cracked butt welded joint based on real welding residual stress, Ocean Eng. 138 (2017) 123–139. https://doi.org/10.1016/j.oceaneng.2017.04.034.

[72] D. Bowness, M.M.K. Lee, Fracture mechanics assessment of fatigue cracks in offshore tubular structures, United Kingdom, 2002.

[73] D. Bowness, Weld toe magnification factors for semi-elliptical cracks in T-butt joints; comparison with existing solutions, Int. J. Fatigue. 22 (2000) 389–396. https://doi.org/10.1016/S0142-1123(00)00013-X.

[74] D. Bowness, M.M.K. Lee, Prediction of weld toe magnification factors for semi-elliptical cracks in T-butt joints, Int. J. Fatigue. 22 (2000) 369–387. https://doi.org/10.1016/S0142-1123(00)00012-8.

[75] P.M. Kyaw, N. Osawa, R. Gadallah, S. Tanaka, Accurate and efficient method for analyzing mixed-mode SIFs for inclined surface cracks in semi-infinite bodies by using numerical influence function method, Theor. Appl. Fract. Mech. 106 (2020) 1–13. https://doi.org/10.1016/j.tafmec.2019.102471.

[76] N. Osawa, J. Sawamura, S. Okada, K. Shigeta, T. Tsuji, Study on the accuracy of influence factor method when applied to surface cracks in a welded joint of a ship structure by, in: J. Japan Soc. Nav. Archit. Ocean Eng., 2010: pp. 201–208. https://doi.org/10.2534/jjasnaoe.12.201.

[77] B. Healy, A. Gullerud, K. Koppenhoefer, A. Roy, S. Roychowdhury, J. Petti, M. Walters, B. Bichon, K. Cochran, A. Carlyle, J. Sobotka, M. Messner, R. Dodds, WARP3D 3-D Dynamic nonlinear fracture analyses of solids using parallel computers, (2016). www.warp3d.net.

[78] F.H.K. Chen, R.T. Shield, Conservation laws in elasticity of the J-integral type, Zeitschrift Für Angew. Math. Und Phys. ZAMP. 28 (1977) 1–22. https://doi.org/10.1007/BF01590704.

[79] M.C. Walters, G.H. Paulino, R.H. Dodds, Interaction integral procedures for 3-D curved cracks including surface tractions, Eng. Fract. Mech. 72 (2005) 1635–1663. https://doi.org/10.1016/j.engfracmech.2005.01.002.

[80] H. Nishikawa, H. Serizawa, H. Murakawa, Development of farge-scaled FEM for analysis of mechanical problems in welding, J. Japan Soc. Nav. Archit. Ocean Eng. 2 (2005) 379–385. https://doi.org/10.2534/jjasnaoe.2.379.

[81] H. Murakawa, N. Ma, H. Huang, Iterative substructure method employing concept of inherent strain for large-scale welding problems, Weld. World. 59 (2015) 53–63. https://doi.org/10.1007/s40194-014-0178-z.

[82] H. Nishikawa, H. Serizawa, H. Murakawa, Actual application of FEM to analysis of large scale mechanical problems in welding, Sci. Technol. Weld. Join. 12 (2007) 147–152. https://doi.org/10.1179/174329307X164274.

[83] J. Wang, N. Ma, H. Murakawa, An efficient FE computation for predicting welding induced buckling in production of ship panel structure, Mar. Struct. 41 (2015) 20–52. https://doi.org/10.1016/j.marstruc.2014.12.007.

[84] N. Ma, H. Huang, H. Murakawa, Effect of jig constraint position and pitch on welding deformation, J. Mater. Process. Technol. 221 (2015) 154–162. https://doi.org/10.1016/j.jmatprotec.2015.02.022.

[85] D. Deng, H. Murakawa, Influence of transformation induced plasticity on simulated results of welding residual stress in low temperature transformation steel, Comput. Mater. Sci. 78 (2013) 55–62. https://doi.org/10.1016/j.commatsci.2013.05.023.

[86] J. Sun, X. Liu, Y. Tong, D. Deng, A comparative study on welding temperature fields, residual stress distributions and deformations induced by laser beam welding and CO2 gas arc welding, Mater. Des. 63 (2014) 519–530. https://doi.org/10.1016/j.matdes.2014.06.057.

[87] MSC. Dytran 2021 User's Guide, The MacNeal-Schwendler Corporation, 2021.

[88] R. Gadallah, N. Osawa, S. Tanaka, Calculation of SIFs along a 3-D crack front with the interaction integral method using a non-uniform residual stress field, Proc. Japan

Soc. Nav. Archit. Ocean Eng. JASNAOE. (2016) 447–452.

[89] MSC.MARC, Volume A: Theory and user information, The MacNeal-Schwendler Corporation, 2014. http://www.mscsoftware.com/.

[90] P.M. Kyaw, N. Osawa, R. Gadallah, S. Tanaka, Comparative study on stress intensity factors for surface cracks in welded joint and flat plate by using the influence function method, in: Vol. 2A Struct. Safety, Reliab., ASME, 2020. https://doi.org/10.1115/OMAE2020-19261.

[91] S. Kusuba, Study on fatigue life assessment by crack monitoring and simulation, Dissertation, Nagasaki University, Japan, 2007. http://naosite.lb.nagasaki-u.ac.jp/dspace/handle/10069/16925.

[92] M.C. Walters, G.H. Paulino, R.H. Dodds Jr, Computation of mixed-mode stress intensity factors for cracks in three-dimensional functionally graded solids, J. Eng. Mech. 132 (2006). https://doi.org/10.1061/ASCE0733-9399.

[93] G. Van Rossum, F.L. Drake, Python 3 Reference Manual, (2009).

[94] P.M. Kyaw, N. Osawa, S. Tanaka, R. Gadallah, Numerical study on the effect of residual stresses on stress intensity factor and fatigue life for a surface-cracked T-butt welded joint using numerical influence function method, Weld. World. 65 (2021) 2169–2184. https://doi.org/10.1007/s40194-021-01172-6.

[95] C. Acevedo, Influence of residual stresses on fatigue response of welded tubular K-joints, EPFL scientific publications, 2011. https://doi.org/10.5075/epfl-thesis-5056.

[96] D. Deng, Y. Zhou, T. Bi, X. Liu, Experimental and numerical investigations of welding distortion induced by CO2 gas arc welding in thin-plate bead-on joints, Mater. Des. 52 (2013) 720–729. https://doi.org/10.1016/j.matdes.2013.06.013.

Publications related to this Thesis

Publications with full or peer review

1. **P. M. Kyaw**, N. Osawa, S. Tanaka, and R. Gadallah, "Numerical weld magnification factor for a semi-circular surface crack in T-butt welded joints using influence function method," in: Vol. 2A Struct. Safety, Reliab., ASME, 2022.
2. **P.M. Kyaw,** N. Osawa, S. Tanaka, R. Gadallah, Numerical study on the effect of residual stresses on stress intensity factor and fatigue life for a surface-cracked T-butt welded joint using numerical influence function method, Weld. World. 65 (2021) 2169–2184. https://doi.org/10.1007/s40194-021-01172-6.
3. **P.M. Kyaw,** N. Osawa, R. Gadallah, S. Tanaka, Comparative study on stress intensity factors for surface cracks in welded joint and flat plate by using the influence function method, in: Vol. 2A Struct. Safety, Reliab., ASME, 2020. https://doi.org/10.1115/OMAE2020-19261.
4. **P.M. Kyaw**, N. Osawa, R. Gadallah, S. Tanaka, Accurate and efficient method for analyzing mixed-mode SIFs for inclined surface cracks in semi-infinite bodies by using numerical influence function method, Theor. Appl. Fract. Mech. 106 (2020) 1–13. https://doi.org/10.1016/j.tafmec.2019.102471.

Conference proceedings

1. **P. M. Kyaw**, N. Osawa, R. Gadallah, and S. Tanaka, "Comparative study on mixed-mode stress intensity factors of as-welded joint and HFMI-treated welded joint," 74th IIW Annual Assembly & International Conference, International Institute of Welding, 12-17 July, 2021, IIW-XIII-2901.
2. **P. M. Kyaw**, N. Osawa, R. Gadallah, and S. Tanaka, "Numerical study on mixed-mode stress intensity factors for a surface crack in HFMI-treated welded joint," in: J. Japan Soc. Nav. Archit. Ocean Eng., 32, 2021: pp. 403–409.
3. **P. M. Kyaw**, N. Osawa, R. Gadallah, and S. Tanaka, "Study on the effect of residual stresses on stress intensity factor and fatigue life of surface-cracked T-butt welded joints using numerical influence function method," 73rd IIW Annual Assembly & International Conference, International Institute of Welding, 19-24 July, 2020, IIW-XIII-2860.

4. **P. M. Kyaw**, N. Osawa, R. Gadallah, and S. Tanaka, "Effect of geometric configurations on stress intensity factors of flat plate and t-butt welded joints," in: J. Japan Soc. Nav. Archit. Ocean Eng., 31, 2020: pp. 239–243.

Publication under review

1. **P. M. Kyaw,** N. Osawa, S. Tanaka, and R. Gadallah, "Influence coefficient based fracture mechanics parameter modification factor for a surface crack in a welded joint", Submitted to Theoretical and Applied Fracture Mechanics.